

**Structure-diagnostic ion molecule reactions with
environmental pollutants studied by theory and
experiment**

by

© Roshanak Amiri

A thesis submitted to the
School of Graduate Studies
in partial fulfillment of the requirements for the degree of
Master of Science (M.Sc.)

Department of Chemistry
Memorial University of Newfoundland
St. John's, Newfoundland and Labrador, Canada

March 2023

St. John's

Newfoundland

Abstract

Atmospheric pressure chemical ionization (APCI) is widely used as a soft ionization technique for mass spectrometry. The APCI source acts not only as an ionization source, but also a reaction chamber for ion-molecule reactions. In this study, we investigated ion-molecule reactions between oxygen and two groups of environmental pollutants that are selective towards toxic isomers. The compounds of interest were tricresyl phosphates (TCPs) and tetrachlorodibenzo-p-dioxins (TCDDs). We propose the mechanisms of the ion molecule reactions of TCPs and TCDDs and provide support through computational and experimental analysis using density functional theory (DFT) and cyclic ion mobility-mass spectrometry (cIM-MS), respectively.

Ortho-substituted isomers of TCPs and their toxic metabolites (e.g., CBDP: cresyl saligenin phosphate) can cause neurotoxic effects in humans. When TCP is introduced to an atmospheric pressure chemical ionization (APCI) source using gas chromatography (GC), abundant radical cations M^{+} are formed by charge exchange. The mass spectrum of an ortho-substituted isomer displays two intense peaks that are absent in the spectra of non-ortho-substituted isomers, leading us to propose a structure-diagnostic ion-molecule reaction between ions M^{+} and ozone. The mechanism proposed in this thesis consists of a multi-step reaction starting with the rearrangement of the molecular ion to a distonic isomer followed by an oxidation step and then, decomposition into $[CBDP-H]^{+}$. This proposal is consistent with the results obtained from a series of isotopically-labelled analogues. Cyclic ion mobility experiments with a triorthocresyl phosphate standard, reveals the presence of at least two hydrogen shift isomers of the product ion $[CBDP-H]^{+}$ that are connected by a low-lying energy barrier. The selectivity of the ion-molecule reaction towards the ortho-substituted cresyl groups in TCP structures provides us with an identification tool that

differentiates potentially toxic and non-toxic tri-aryl phosphate esters present in complex mixtures of isomers that are produced in large volume by industry.

TCDDs are infamous for their toxicity and persistence in the environment after being generated from the combustion of polychlorinated compounds. The analysis of (mixed) halogenated dibenzo-p-dioxin isomers is challenging due to the limitations of traditional separation techniques and the paucity of authentic standards. Hard ionization techniques, including EI, are not informative due to a lack of isomer selective fragmentation. However, when APCI is used in negative mode, TCDD isomers undergo isomer selective bond cleavages. Previous experimental studies have reported on two selective ion-molecule reactions between TCDDs and O₂. First, the oxidation reaction resulting in [M-Cl+O]⁻ ions, and second, the ether cleavage reaction resulting in a radical anion and a neutral product. In this thesis, mechanisms are proposed for both oxidation and ether cleavage reactions using Density Functional Theory (DFT) calculations. We also calculated theoretical collision cross section (CCS) values for the ether cleavage products using MobCal-MPI to support further studies on separating their isomeric structures using cyclic-ion mobility. These mechanisms will guide the eventual development of experimental methods that can differentiate between (potentially) toxic and non-toxic mixed halogenated dibenzo-p-dioxins.

Acknowledgements

I would like to express my gratitude to Dr. Karl J. Jobst for giving me the opportunity of being a part of this research. You gifted me precious moments of being filled with the deepest joy of science: learning and discovery. I appreciate all your help, patience, guidance and support throughout my Master's. Doing my Master's under your supervision will always be one of the biggest honors of my life that makes me proud every time I think of it. Thank you for all the colors you added to the main scenes of my science journey.

To all members of the Jobst team, thank you. I received numerous helps and supports from my awesome colleagues including Tannia, Xiaolei, Meera, Mahin, Ethan, Amber, Bradley, Jake, Kevin, Olivia and Samiha. I was really lucky to be a part of an amazing team that taught me so many lessons through all the moments we shared and all the memories we made together. I would like to thank my committee members, Dr. Lindsay Cahill and Dr. Yuming Zhao, for their help and guidance for improving the quality of this thesis. I would also thank the Memorial University of Newfoundland with special thanks to SGS and TAUMUN for the fundings and financial supports.

Finally, I would like to thank my family. To my mother who always supported me for following my dreams in science, my father who inspired me for having enough courage to face the hardest challenges on my path, and my brother who believed in me when I needed it the most. I would also like to thank my partner, Umar, who gave light to my darkest disappointments and supported me in all the ways he could. Words may not be enough to thank all the faith you had in me and all the love you showed to me, but I will always be grateful for your endless help and support.

Table of Contents

Abstract	ii
Acknowledgements	iv
Table of Contents	v
List of Tables	vii
List of Schemes	viii
List of Figures	ix
List of Abbreviations and Symbols	xii
Chapter 1. Introduction	1
1.1. Structure-toxicity relationships for organic pollutants.....	1
1.1.1. Tri-cresyl phosphates	2
1.1.2. Tetrahalogenated dibenzo-p-dioxins.....	3
1.2. Instrumental analysis.....	5
1.2.1. Separation by gas chromatography	6
1.2.2. Ionization	7
1.2.3. Tandem mass spectrometry	8
1.2.4. Collision induced dissociation.....	10
1.2.5. Cyclic-ion mobility	11
1.3. Computational chemistry	22
1.3.1. Calculation of thermodynamic properties	27
1.3.2. Prediction of collision-cross section values	28
1.4. Objectives.....	31
References	32
Chapter 2. Differentiating toxic and non-toxic tricresyl phosphate isomers using ion-molecule reactions with oxygen	42
2.1. Introduction	43
2.2. Experimental Section	45
2.2.1. Chemicals and Sample preparation.....	45
2.2.2. Instrumental Analysis	45
2.2.3. Computational methods.....	46
2.3. Results and Discussion.....	47

2.3.1. Parallels between the metabolism of ToCP and its ion-molecule reactions with oxygen	47
2.3.2. Computational analysis of the mechanism.....	51
2.3.3. Complementary experiments with (isotopically labeled) isomers and homologues	56
2.3.4. Characterization of the [CBDP-H] ⁺ product ions using ion mobility.....	58
2.4. Conclusions	60
References	62
Supporting Information	69
Chapter 3. A Mechanistic Analysis of the Ion-Molecule Reaction between Oxygen and Tetrahalogenated Dibenzo-p-Dioxins	111
3.1. Introduction	112
3.2. Experimental Section	114
3.2.1. Computational methods.....	114
3.3. Results and Discussion.....	115
3.3.1. Computational analysis of the oxidation mechanism	115
3.3.2. Computational analysis of the ether cleavage reaction mechanism.....	116
3.3.3. Is the ether cleavage reaction regioselective for asymmetric TCDDs (e.g., 1,3,7,8 TCDD)?	118
3.3.4. The exothermicity of ether cleavage reactions on other TCDDs	119
3.3.5. Application of collision cross section in structural studies on ether cleavage products	120
3.4. Conclusions	124
References	125
Supporting Information	131
Chapter 4. Conclusions and future work.....	140

List of Tables

Table 3.1. The enthalpies of ether cleavage reactions of selected TCDD isomers 123

Table 3.2. Theoretical CCS values of ether cleavage products of the selected TCDD isomers and the required CCS resolutions obtained from MobCal-MPI calculations 123

List of Schemes

Scheme 2.1. The metabolism of ToCP (tri-ortho cresyl phosphate) into the toxic metabolite CBPD	48
Scheme 2.2. Rearrangement of TCP5a to TBC1 and TSBC, resulting in the formation of TCP6+ ·OH	54

List of Figures

Figure 1.1. The structures of **a)** organophosphate esters, **b)** triaryl phosphates and **c)** tricresyl phosphate 2

Figure 1.2. The structure of tricresyl phosphate and three types of ortho, meta, and para positions available for CH₃ groups. Only ortho-positioned methyl groups cause toxicity (shown in red) 3

Figure 1.3. The general structure of a polyhalogenated dibenzo-p-dioxin 4

Figure 1.4. The general structure of a polyhalogenated dibenzo-p-dioxin congener and two types of lateral and non-lateral positions available for halogen substitutes. Only lateral-positioned halogens cause toxicity (shown in red) 4

Figure 1.5. The schematic view of the GC-APCI-cIM-MS applied for the instrumental analysis 6

Figure 1.6. The close view of the cIM chamber performing slice selection experiments on mobility separated ions 14

Figure 1.7. The cIM device and the potential energy schematics of the cIM functions 17

Figure 1.8. The cIM instrument photographs 18

Figure 1.9. DT-RT and DT-m/z Contour plots 19

Figure 1.10. The DT-m/z and DT-RT plots before and after unwrapping the wrap arounds 22

Figure 2.1. (a) APCI⁺ mass spectrum of ToCP (ToCP^{•+} radical cation [m/z 368.1177] was not observed); CID mass spectra of (b) m/z 383 and (c) m/z 275 ions generated from ToCP. Note: The m/z 275 region of the mass spectrum in (a) is magnified by 10-fold 49

Figure 2.2. Selected ion chromatograms of (a) [M+H]⁺ (m/z 369); (b) M⁺ (m/z 368); and (c) [CBDP-H]⁺ m/z 275 ions generated by an equimolar mixture of ToCP, TmCP and TpCP 50

Figure 2.3. Energy diagram depicting the proposed mechanism for the ion-molecule reactions of ToCP^{•+} with O₂. The numbers in square brackets are relative energies (in kcal/mol) from **Table S2.1.** 53

Figure 2.4. Energy diagram depicting the proposed mechanism for the ion-molecule reactions of ToCP^{•+} with O₃. The numbers in square brackets are relative energies (in kcal/mol) from **Table S2.2.** 55

Figure 2.5. The APCI⁺ mass spectrum of D₉-labeled (methyl CD₃) triorthocresyl phosphate (tri-CD₃-o CP) 56

Figure 2.6. Selected ion contour plots of m/z 275 ions that have travelled (a) 1 pass; (b) 8 passes; and (c) 16 passes through the cIMS cell. The two peaks at ~23 ms and ~24.5 ms correspond to genuine m/z 275 isomers separated by ion mobility. The peak at ~29 ms is an artefact peak resulting from metastable decomposition of m/z 383 ions occurring downstream of the cIMS cell. The BGR color scale was used to display intensity 59

Figure 2.7. Selected ion contour plots of m/z 275 ions (a) generated in the source; and generated from mass selected m/z 383 ions that undergo CID in trap (b) and transfer (c) collision cells 60

Figure 3.1. The energy diagram of the oxidation reaction ($M^{\bullet-} + O_2 \rightarrow [M-Cl+O]^- + ClO^{\bullet}$) between 2,3,7,8 TCDD and O_2 obtained from B3LYP/6-311G (2d, d, p) energy calculations 116

Figure 3.2. The energy diagram of the ether cleavage reaction ($M^{\bullet-} + O_2 \rightarrow ECPI+ECPN$) between 2,3,7,8 TCDD and O_2 obtained from B3LYP/6-311G (2d, d, p) energy calculations 117

Figure 3.3. The energy diagrams of the ether cleavage reactions ($M^{\bullet-} \rightarrow ECPI+ECPN$) between 1,3,7,8 TCDD and O_2 for the formation of **a.** 1,3 ECPI and **b.** 2,3 ECPI obtained from B3LYP/6-311G (2d, d, p) energy calculations 119

Figure 3.4. The structures of six selected TCDD $^{\bullet-}$ structures and their ether cleavage products 122

Figure 3.5. The structures of ECPIs produced from of the six selected TCDD isomers and the corresponding theoretical CCS values obtained from MobCal-MPI calculations 123

List of Abbreviations and Symbols

Å: angstrom

APCI: atmospheric pressure chemical ionization

APCI (+): atmospheric pressure chemical ionization in positive mode

APCI (-): atmospheric pressure chemical ionization in negative mode

API: atmospheric pressure chemical ionization

°C: degree Celsius

°C/min: degree Celsius per minute

CBDP: cresyl saligenin phosphate (2-(ortho-cresyl)-4H-1,2,3- benzodioxaphosphorin-2- oxide)

CCS: collision cross section

CID: collision induced dissociation

cIM: cyclic ion mobility

DFT: density functional theory

DT: drift time

EC: ether cleavage

ECPI: ether cleavage product ion

ECPN: ether cleavage product neutral

et al.: and others

eV: electron volt

GC: gas chromatography

HF: Hartree Fock

IRC: intrinsic reaction coordinate

K: Kelvin

kcal/mol: kilocalorie per mole

kJ/mol: kilojoule per mol

M^{•+}: radical cation

M^{•-}: radical anion

MS: mass spectrometry
m/z: mass to charge ratio
OX: oxidation
PBDD: poly-brominated dibenzo-p-dioxin
PCB: printed circuit board
PCDD: poly-chlorinated dibenzo-p-dioxin
PXDD: mixed poly-halogenated dibenzo-p-dioxin
Quad: quadrupole
RT: retention time
TBDD: tetra-brominated dibenzo-p-dioxin
TCDD: tetra-chlorinated dibenzo-p-dioxin
TCP: tricresyl phosphate
THDD: tetra-halogenated dibenzo-p-dioxin
TM: trajectory method
TmCP: tri-meta-cresyl phosphate
ToCP: tri-ortho-cresyl phosphate
TOF: time-of-flight
TpCP: tri-para-cresyl phosphate
TS: transition state
TW: travelling wave
TXDD: mixed tetra-halogenated dibenzo-p-dioxin

Chapter 1. Introduction

1.1. Structure-toxicity relationships for organic pollutants

Organic pollutants often consist of many congeners and isomers. The toxicity of the isomers in each group of congeners is dependent on their unique structures. Mass spectrometry is an analytical technique widely used for structural characterization of environmental pollutants [1]. The ionization and activation techniques employed for each set of mass spectrometry experiments determines the structural information present in the resulting mass spectra [2]. *Hard* ionization techniques impart relatively high internal energies to the incipient ions, resulting in high energy fragmentation reactions that can provide valuable structural information [3]. *Soft* ionization techniques are ideal for the analysis of involatile or labile compounds, and provide structural information from low energy fragmentations and rearrangements [3,4] when coupled with tandem mass spectrometry. However, mass spectrometry is often perceived as a technique that does *not* provide sufficient structural information to differentiate between isomers.

“Real-world” samples contain complex mixtures of environmental pollutants that are mass-produced by industry [5]. A limited number of these pollutants are currently monitored using mass spectrometry, often coupled with gas or liquid chromatography. However, authentic standards are not available for a large number of (un)known pollutants present in the environment, and their structures and the corresponding toxic effects remain unknown [6].

Atmospheric pressure chemical ionization (APCI) is a soft ionization technique that can provide novel structural information on pollutants [7]. This information is derived from the products of ion-molecule reactions that occur during ionization [7,8]. Some ion-molecule reactions

have been shown to be selective toward toxic isomers of environmental pollutants [9], as witnessed by unique differences between the mass spectra of toxic and non-toxic isomers. Thus, they can potentially provide us with an identification tool that links the mass spectrum of a structure to its corresponding toxicity.

The scope of this thesis focuses on two groups of organic pollutants possessing structure-dependent toxicities: tricresyl phosphates and tetrahalogenated dibenzo-p-dioxins.

1.1.1. Tri-cresyl phosphates

Organophosphate esters are used in a wide variety of applications in industry, discussed in Chapter 2. Section 2.1. They consist of a phosphate ester that is connected to three R groups at the single-bonded oxygen atoms (Figure 1.1a). If all R groups are aryl substituents, the resulting structure will be a triaryl phosphate (Figure 1.1b), and if all aryl groups are methyl substituted, the resulting subclass of triaryl phosphates will be the tricresyl phosphate (TCP) [10,11], shown in Figure 1.1c.

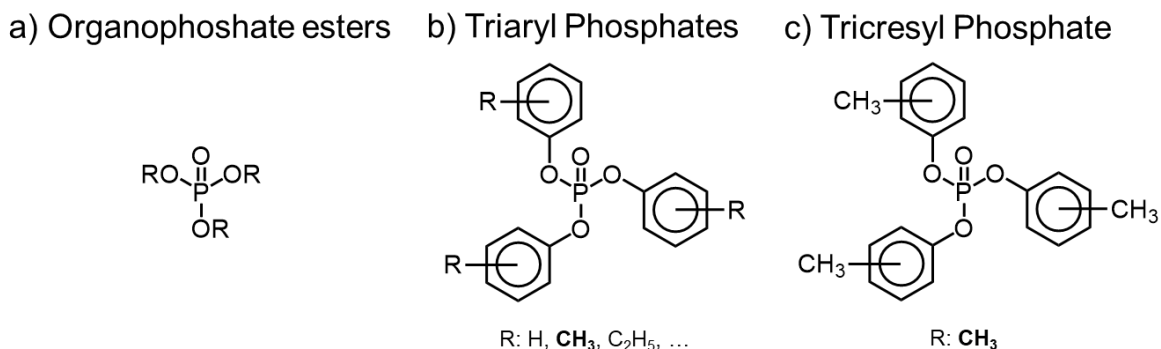


Figure 1.1. The structures of **a)** organophosphate esters, **b)** triaryl phosphates and **c)** tricresyl phosphate

The structure of TCP offers three positions (ortho, meta, and para) to methyl groups, and there are ten TCP isomers (Figure 1.2). The toxicity of a TCP isomer depends on the number of

ortho-substituted cresyl (*o*-cresyl) groups present. The six most toxic isomers contain at least one *o*-cresyl group [10,11], explored in Chapter 2. Section 2.1.

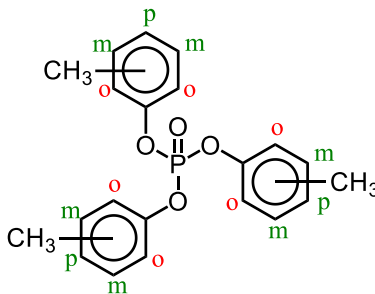


Figure 1.2. The structure of tricresyl phosphate and three types of ortho, meta, and para positions available for CH₃ groups. Only ortho-positioned methyl groups cause toxicity (shown in red).

The toxicity of the ortho-substituted TCPs may be expanded to a larger class of ortho-substituted triaryl phosphates. This proposal can be explained by the similar chemical behavior of congeners in a given group of organic compounds, including tri-aryl phosphates. For instance, longer (ethyl, propyl, etc.) alkyl chains may show the same chemical behavior as methyl groups in TCPs. Thus, an identification tool that differentiates between toxic and non-toxic congeners in complex samples can be useful for future environmental studies on triaryl phosphates. (Discussed in detail in Chapter 2)

1.1.2. Tetrahalogenated dibenzo-p-dioxins

Polyhalogenated dibenzo-p-dioxins consist of two (4-8) halogen (Cl/Br) substituted benzene rings connected by two oxygen bridges [12], depicted in Figure 1.3.

Polyhalogenated dibenzo-p-dioxins are not directly produced by industry but are released to the environment during the combustion processes [13,14], explored in Chapter 3. Section 3.1. The structure of polyhalogenated dibenzo-p-dioxins offers two types of lateral and non-lateral positions

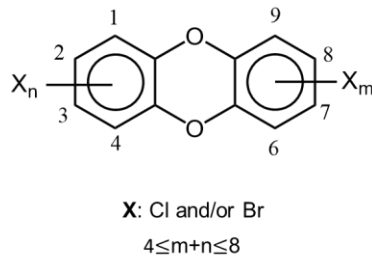


Figure 1.3. The general structure of a polyhalogenated dibenzo-p-dioxin. (1-4 and 6-9 numbers show the available positions for halogens on the dioxin structure).

to halogens (Figure 1.4) generating a large group of 1550 congeners [15]. The most toxic congeners in this class of compounds are those containing lateral-positioned halogens [16], shown in Figure 1.4.

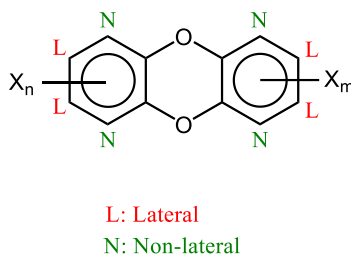


Figure 1.4. The general structure of a polyhalogenated dibenzo-p-dioxin congener and two types of lateral and non-lateral positions available for halogen substitutes. Only lateral-positioned halogens cause toxicity (shown in red).

Polychlorinated dibenzo-p-dioxins (PCDDs) consist of 75 congeners, among which only the 7 highly toxic congeners (2,3,7,8-substituted PCDDs) are identified and quantified in the environment [17]. The toxicity levels of the polyhalogenated dioxins are determined by their toxic equivalency factor (TEF) [18]. TEF assigns the relative toxicity of each dioxin by comparing its toxicity to 2,3,7,8-TCDD as the most toxic congener with the TEF of 1 ranging from 0.00001 (least toxic) to 1 (most toxic) [18–20].

Further studies on polyhalogenated dioxins were expanded to the identification and quantification of a limited number of mixed polyhalogenated dibenzo-p-dioxins (PXDDs) [21,22]. Nevertheless, the separation and identification of the majority of congeners present in complex samples are limited by the large number of PXDDs (1400 congeners) and the lack of authentic standards [13]. The focus of this study is on tetrahalogenated dibenzo-p-dioxins, yet it may lead to the discovery of a diagnostic tool that identifies and separates all the toxic congeners in complex mixtures of polyhalogenated dibenzo-p-dioxins.

1.2. Instrumental analysis

Mass spectrometry (MS) is the most powerful detector hyphenated with gas chromatography [23,24]. In GC-MS, the separation of compounds by gas chromatography is accompanied by rich mass spectrometric information on the structure and identities of analyte molecules [23,24]. The experiments described in this thesis were performed with a gas chromatographic (GC) cyclic ion mobility-mass spectrometer (cIM-MS) equipped with an atmospheric pressure chemical ionization (APCI) source (GC-APCI-cIM-MS). The schematic of the instrument is shown in Figure 1.5 and the sections below describe each stage of chromatographic separation, ion mobility and mass analysis.

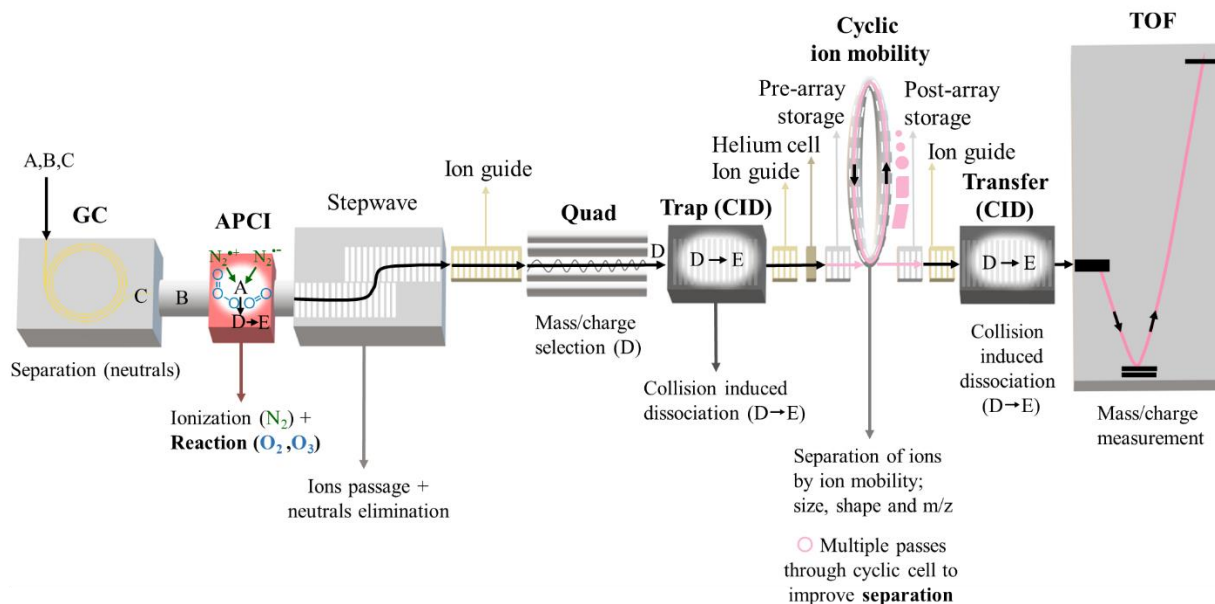


Figure 1.5. The schematic view of the GC-APCI-cIM-MS employed for the instrumental analysis.

1.2.1. Separation by gas chromatography

Gas chromatography (GC) is among the most widely used techniques to separate closely related compounds present in (complex) mixtures [25,26]. The basis of separation in chromatography methods can be explained by their mobile phase (MP), stationary phase (SP), and the equilibrium during the transfer of analytes between the two phases. For instance, the stronger analyte-SP interactions (and weaker analyte-MP interactions) result in a later elution from the chromatography column and larger retention time (RT). GC is the chromatography technique used for the separation of volatile and semi-volatile analytes. In the work presented in this thesis, GC was employed as an inlet. In GC, the analyte molecules are partitioned between a gaseous mobile phase and a liquid stationary phase that is coated on the interior walls of an open tubular column [27]. When a mixture of analytes (e.g. compounds A, B, and C in Figure 1.5) is injected to the

instrument, GC separates the analytes and the analyte molecules are subsequently swept through a heat transfer line and into the ionization source.

1.2.2. Ionization

The entrance to every mass spectrometer is its ionization source. Ionization sources may be categorized into two general categories: *hard* ionization and *soft* ionization sources. For example, electron ionization (EI) is a *hard* ionization technique. In EI, gaseous analytes molecules are bombarded by a beam of energetic electrons (~ 70 eV). The low mass and high kinetic energy of these electrons cause a negligible elevation in the translational energy of the analytes. Instead, the vibrational and rotational energy levels of the analyte molecules increase which results in the formation of molecular ions (M^+) and extensive fragmentation. The fragment ions observed in an EI spectrum play the main role in the structural identification of analytes [27], but isomeric compounds often yield virtually identical EI mass spectra.

Atmospheric pressure chemical ionization (APCI) is the soft ionization technique used in this thesis (see Fig. 1.5) and it offers several advantages over conventional EI. First, this set of techniques do *not* require vacuum systems in the ionization source and the resulting collisional cooling at atmospheric pressure increases the yield of the molecular ions. Consequently, the elemental compositions can be determined and the detection limits may be enhanced. Second, a wide variety of sophisticated mass spectrometry systems can be modified to perform GC-APCI. Most importantly, API source conditions may promote structure diagnostic ion-molecule reactions that do *not* occur using classic ionization techniques [28]. Other types of API techniques that have been hyphenated with GC-MS include atmospheric pressure photoionization (APPI) [29], and atmospheric pressure laser ionization (APLI) [30].

In APCI, a high flow of make-up gas sweeps the eluted sample molecules from the GC transfer line towards the corona discharge. Corona discharge results in the ionization of make-up gas and generates a plasma of primary ions (e.g., N_2^{*+} and N_4^{*+} in case of using N_2 as the make-up gas) and electrons. Similar to conventional chemical ionization (CI) technique, ionization of the analytes occurs via the collisions between primary ions and neutral analyte molecules. The occurrence of charge transfer during the collisions depends on the recombination energy of the primary ions, which must exceed the ionization energy (IE) of the analyte. The make-up gas is usually an inert gas (to promote non-reactive collisions) with a higher IE than the analytes. [28,31]. Further collisions between the ionized analytes and neutral molecules present in the source, including oxygen species, can result in ion-molecule reactions.

In the GC-APCI-cIM-MS instrument used for these studies, the precursor and product ions of the ion molecule reactions (D and E in Figure 1.5) generated in APCI source are guided to the mass analyzer (quadrupole) through the "Stepwave" and the first ion guide. The main function of the Stepwave is guiding the ions while eliminating the neutral species from the ions' pathway.

1.2.3. Tandem mass spectrometry

Tandem mass spectrometry (MS/MS) is a technique that combines two or more mass analyzers. This enables the selection of precursor ions (or neutrals), such as molecular ions and their fragmented and/or rearranged product ions, and probing their structures using collision experiments with a target gas such as He, N_2 or Ar. The cyclic ion mobility-mass spectrometer used in the studies of this thesis is a unique tandem mass spectrometer consisting of quadrupole and time-of-flight mass analyzers, hyphenated with a cyclic ion mobility cell [27,32].

The quadrupole mass analyzer (Q; Quad) consists of four parallel cylindrically shaped rod electrodes and operates according to the following principles. One pair of opposite rods is connected to the positive side of a variable DC (direct current) source, and the other pair is connected to the negative side. Furthermore, variable radio-frequency AC (alternating current) voltages are applied to each pair of rods. Ions entering the quadrupole mass analyzer are attracted to oppositely charged rods, and as they pass through the Quad, they undergo stable oscillating motion resulting from the combination of attractive and repulsive forces [33]. The combination of DC and AC voltages enables the user to select a range of mass to charge ratios of ions that can pass through the quadrupole. The ions with m/z values outside the selected range are deflected and eliminated through neutralization by collisions with the rods. This allows for selecting ions of interest based on their m/z values for further collision induced dissociation (CID) and cyclic ion mobility (CIM) experiments [27,32–34]. The Quad in the instrument employed for this thesis can be operated to allow for the passage of all ions generated in the source or to eliminate the passage of ions outside a selected narrow range of mass to charge (m/z) ratios (D in Figure 1.5) for CID experiments.

The time-of flight (TOF) mass analyzer involves measuring the time required for an ion to travel from the TOF entry to the detector, which is directly related to its mass to charge ratio. Ions have approximately equal kinetic energy when they enter the TOF mass analyzer, and are then accelerated towards the detector. Ions with equal kinetic energies, but different mass to charge ratios, will have different velocities. Thus, ions of lower mass to charge ratios will reach the detector sooner than the heavier ions and their m/z values are obtained from Equation 1.1, which shows the theoretical relationship between the velocity (v) of an ion with its mass m_i and its charge of ze (the number (z) of elementary (e) charges) accelerated through a voltage of U . [27,35].

$$v = \sqrt{\frac{2zeU}{m_i}} \quad (\text{Eq 1.1.})$$

As shown in Equation 1.1, the velocity of each ion is inversely proportional to the square root of its mass [33].

The TOF mass analyzer in the instrument employed for this thesis studies offers two advantages over the previous generation of TOF analyzers by having an increased length (40 cm higher than SYNAPT G2-Si [32,36]) and enabling users to perform the experiments in two modes (V and W). Increasing the length of TOF and consequently, the distance that ions travel, improves the separation of the ions by widening the distribution of their velocities and flight durations. Operating TOF in W mode (triple deflection; longer ion path) yields higher resolutions while in V mode (double deflection; shorter ion path) the sensitivity is increased by limiting the loss of ions [32]. (Note that Figure 1.5 shows the instrument when TOF is operated in V mode)

1.2.4. Collision induced dissociation

Tandem mass spectrometers are equipped with one or more collision cells that enable collision-induced dissociation (CID) experiments. The mass analysis and collision events may occur sequentially over time, as is the case with ion trap and Fourier transform mass spectrometers. In tandem quadrupole and quadrupole time-of-flight (QTOF) mass spectrometers, the precursor ions are mass selected by a quadrupole mass analyzer before being accelerated through a collision cell located in adjacent region of the instrument. This collision gas is usually an inert gas (e.g., He, N₂ or Ar) whose collisions with the precursor ions do not result in a chemical reaction. The energy that is transferred to the precursor ions through the collisions highly depends on the applied collision energy.

In the GC-APCI-cIM-MS instrument employed in these studies, two collision cells are located between Quad and TOF mass analyzers. The first collision cell is located before the cyclic cell (trap) and the location of the second collision cell is after the cyclic cell (transfer). When CID takes place ($D \rightarrow E$; Figure 1.5) in the trap, the mobilities of the product ions can be measured. In contrast, when CID is performed in the transfer cell, both the precursor ion and its dissociation products will be observed with the same mobility [27]. This can aid in spectral deconvolution.

1.2.5. Cyclic-ion mobility

Ion mobility (IM) instruments provide additional information on the structure of ions by mobility-based separation of ions. This separation can be achieved in several ways, but using the traditional approach, an electric field accelerates ions through a buffer gas that is chemically inert through a drift tube of fixed length (DT-IMS). Non-reactive collisions with the buffer gas impede the ions and increases the drift time required for the ion to travel through the ion mobility cell. The drift time of each ion is dependent on the number of its collisions with buffer gas, the temperature, and the surface area of the ion. This surface area is reported in \AA^2 as collision cross section (CCS) which depends on the size and shape of the ion [37].

The new generation of high-resolution ion mobility techniques provide higher resolutions with improved sensitivity compared to DT-IMS. Travelling wave ion mobility (TW-IM) is technique used in this thesis [37].

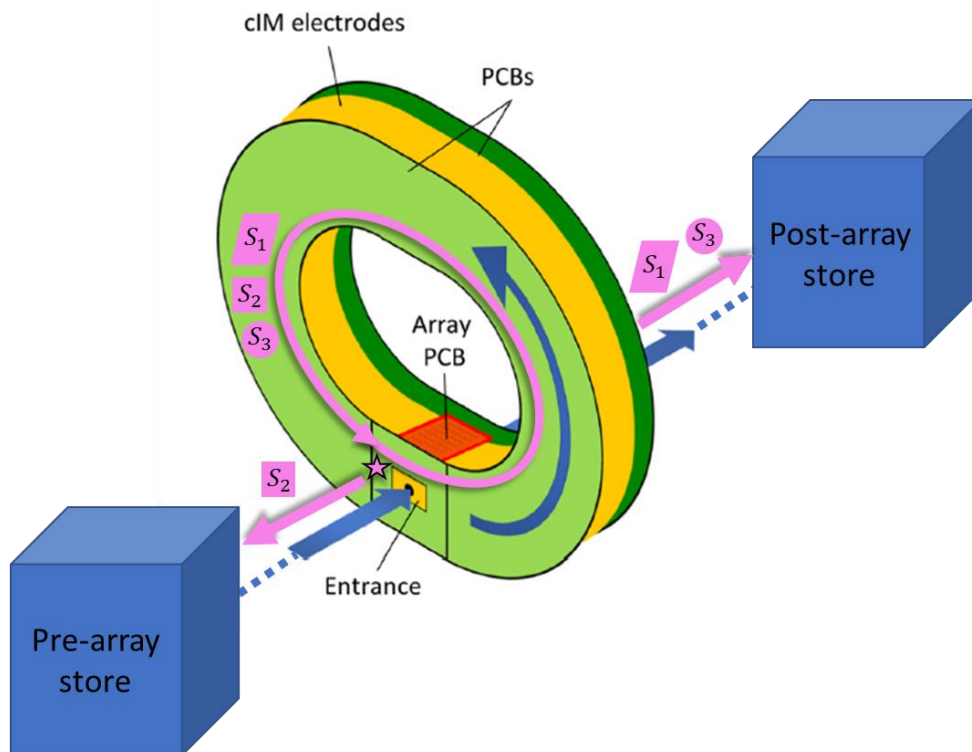
The ion mobility section of the instrument contains a series of electrodes positioned orthogonal to the ion transmission axis. A radio frequency (RF) voltage is applied in opposite phases to adjacent electrodes providing a radially confining potential barrier [38]. The presence of the buffer gas molecules inside the ion mobility device decelerates or stops the ion axial motion

[36]. To propel the ions through the buffer gas, a direct current (DC) voltage is superimposed on the RF of a pair of adjacent electrodes in a repeating sequence along the ion mobility device [36,39]. The generated series of potential hills are subsequently applied to the next pair of electrodes at regular time intervals forming a continuous sequence of “travelling waves” [36]. Then, the ions “surf” on the wavefronts of the travelling waves until the waves overtake them. The frequency with which the waves overtake the ions is correlated to the mobility of the ions (reverse relationship). Thus, ions of lower mobility get overtaken more frequently than the ones with higher mobility and take longer to transit the device, which explains the basis of mobility separation [32,39,40].

The schematic of the cyclic ion mobility (cIM), shown in Figure 1.5, indicates that the cyclic cell is positioned orthogonal to the main ion path. Ions exiting the Quad enter the trap cell that accumulates them and releases them in multiple packages of ions. When the first package of ions is released to the cIM for mobility separations, the next package is accumulated in the trap until the separation completes. Then, the mobility separated ions exit the cIM and the trap releases the next package of ions to the cIM. The released package of ions passes through a helium cell that reduces the ion scattering and activation prior to their entrance into the high-pressure cIM chamber, to which N_2 is supplied as the buffer gas [32,40]. The cIM chamber consists of a pre-array and a post-array store in addition to the cyclic cell. These two storage units have two main functions: transportation of ions to and from the cyclic cell and storing mobility selected “slices” of ions.

Cyclic ion mobility instrument allows for selecting “slices” of ions that are of our interest for further ion mobility studies. To perform these experiments, the cIM should be operated with “ejection to pre-array store” function (Figure 1.7g; described in detail later). Figure 1.6 shows a close view of the cIM chamber that performs the mobility separation on a mixture of S_1 , S_2 and S_3

slices of ions. When the mobility separation is completed, the selected slice of ions (S_2 in Figure 1.6) is ejected to the pre-array store while the remaining slices of ions (S_1 and S_3) are ejected to the post-array store and continue their path to the TOF. Pre-array store accumulates the selected slices of ions (S_2 in Figure 1.6) until they are reinjected into the main array (cyclic cell). Reinjection of the selected slices of ions into the array can be performed under collision induced dissociation conditions, as required, prior to further mobility separations. Then, the product ions can either be ejected to post-array store guided to the TOF analyzer or undergo further slicing experiments. The reinjection of ions from the pre-array store into the array is similar to injection function (Figure 1.7b; described in detail later), nevertheless, it is *not* correlated to the release of packages of ions from the trap.



★ Selection of mobility separated slices of ions

Figure 1.6. The close view of the cIM chamber performing slice selection experiments on mobility separated ions. Adapted from Giles et al. [32]. © Copyright 2019, American Chemical Society; ACS AuthorChoice.

The cIM instrument can be operated in five main modes: injection, separation, ejection to TOF, ejection to pre-array store, and bypass.

Injection: When each package of ions is released from the trap, ions are guided to the pre-array store and finally reach the array (Figure 1.7a). The array holds the ions and prepares them for mobility separations. The DC potential of the array is adjusted to a level that is below that of the (i) pre-array store to let all ions of each package flow into the array, (ii) main cIM electrodes to prevent ions from entering the cIM separation region prematurely and (iii) array exit aperture to

avoid the direct passage of the ions to the post array store, see Figure 1.7b. Then, a low-height travelling wave (TW) is applied in the array to distribute the ions throughout the array region (Figure 1.7e). The injection mode is held till all ions have entered the array region.

Separation: The injection of each package of ions is followed by the separation of the ions based on their mobilities. To let the ions travel through the cyclic cell, the DC potential of the array is increased to a level equal to that of the cIM electrodes, see Figure 1.7d. To avoid the exit of the ions from the cyclic cell, the DC potentials of the cIM entrance and exit apertures are ramped up to a level higher than the array. To make the ions travel around the cIM separator, the direction and amplitude of the TWs in the array are adjusted to match those of the cIM electrodes (Figure 1.7c-d). The ions travelling the same cyclic path arrive at the cyclic cell exit spot at different times depending on their mobilities. The arrival time of the ions is recorded as their “drift time” which is a traditional term for reporting ion mobility results coming from the drift tube ion mobility instruments. The length of time period given for mobility separation mode is determined by the user based on the type of analytes and desired experiments.

Ejection: The mobility separated ions undergo an ejection process after spending their whole separation time inside the cyclic cell. The ejection processes can be performed in two different modes depending on the experiment: (i) Ejection to TOF and (ii) Ejection to pre-array store.

When ions are subjected to ejection to TOF, the DC potential of the array is lowered to a level below that of the cIM electrodes and the cIM entrance aperture, but still higher than the post-array store. Then, the DC potential of the cIM exit aperture is decreased to a level lower than that of the array to let the mobility separated ions flow from the array into the post-array store. Furthermore, the direction of the TWs in the array is altered toward the exit to push the separated ions toward the exit aperture (Figure 1.7e-f). Meanwhile, the operation of the TWs in the cIM

electrodes continues to deliver all mobility separated ions of the same package. Ions exiting the cIM are guided toward the TOF through the post-array store, ion guide (IG) and the transfer cell.

Ejection to Pre-array store: One of the unique features of the cyclic ion mobility instrument is that the mobility separation can be followed by additional experiments (including slicing experiments) prior to ejection to the TOF. These experiments require a different ejection mode called “ejection to pre-array store”. Similar to ejection to TOF, this mode involves decreasing the DC potential of the array to a level below that of the cIM electrodes, see Figure 1.7g. However, unlike the ejection to TOF, the DC potential of the array is kept higher than the pre-array store and the entrance aperture to let the ions flow into the pre-array store. In the meantime, the DC potential of the exit aperture is adjusted to a level higher than the array to prevent the flow of ions into the post-array store towards the TOF. Moreover, the direction of the TW in the array is altered toward the entrance aperture to push the ions enter the pre-array store. Then, the pre-array store receives all or selected slices of the mobility separated ions from the cIM.

Bypass: The GC-cIM-MS instrument enables the users to perform mass spectrometry experiments with the standard Q-TOF geometry and exclude the ion mobility separations from the instrumental analysis. These experiments require operating the cIM in bypass mode via which the ions are transported directly from the pre-array to the post array store through the array bypassing the cIM separation region. To implement the continuous transmission of the ions, the DC potentials of the apertures inside the cIM chamber are adjusted to decrease gradually from the pre-array store to the entrance aperture, array, exit aperture, and post-array store, see Figure 1.7h. To avoid the entry of the ions into the cIM separation region, the DC potential of the array is kept below that of the cIM electrodes. To ensure that all ions pass through the array toward the post-array store, the direction of the TWs in the array is adjusted toward the exit aperture [32].

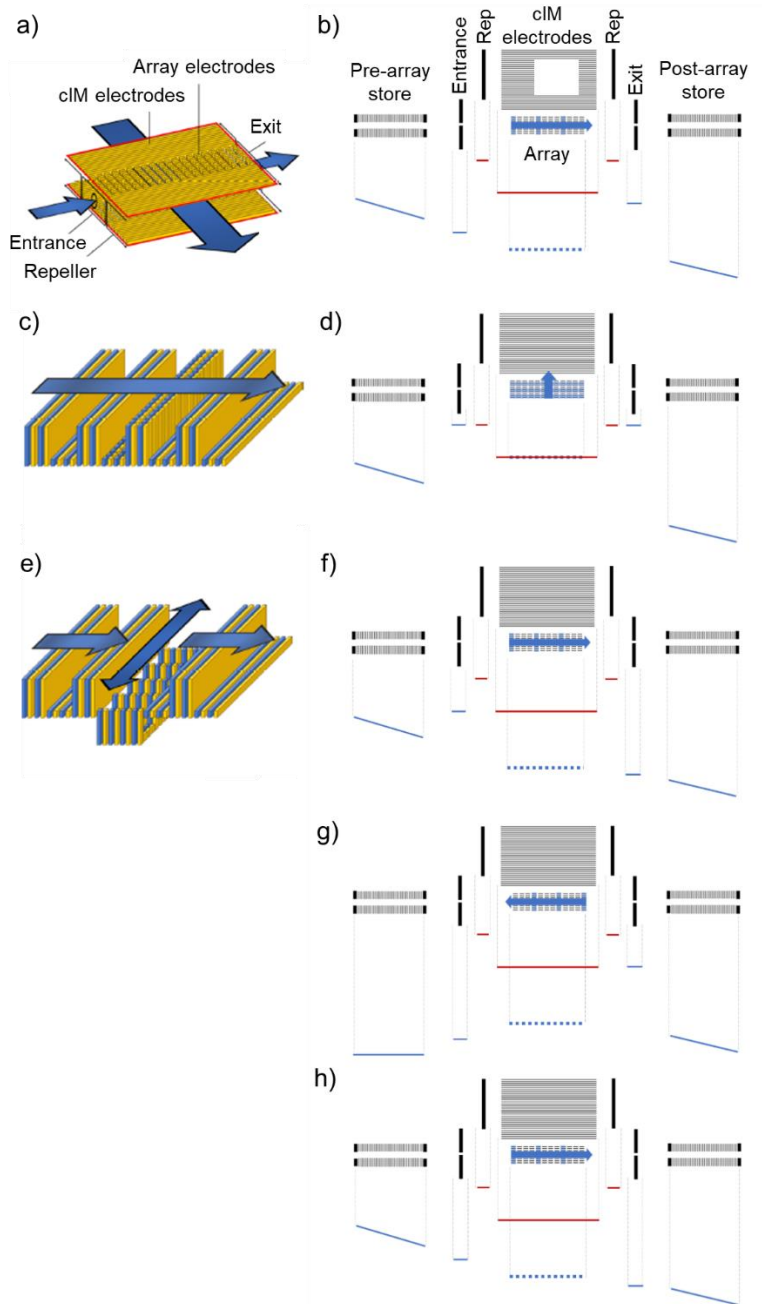


Figure 1.7. The cIM device, a) ion entry/exit region, consisting of array electrodes; c) ion injection/ejection mode; e) separation mode, and the potential energy schematics of the cIM functions, b) injection; d) separation; f) ejection to TOF; g) ejection to pre-array store; h) bypass. Settings changeable on a per function basis: blue lines. Settings changeable on a per sequence basis: red lines. Blue arrows indicate the direction of the array TW direction. Reproduced from Giles et al. [32]. © Copyright 2019, American Chemical Society; *ACS AuthorChoice*.

The photographs of the cIM device are provided in Figure 1.8 showing how it is designed to perform injection/ejections and mobility separations perpendicularly. The array of electrodes (also called array) in cIM device allows for the operation of TWs in two orthogonal directions with one direction for injection/ejections and the other for mobility separations (Figure 1.7c-e). To enable this function, the printed circuit boards (PCBs) supporting the electrodes of the ion entry/exit region (red rectangle in Figure 1.8) are assembled orthogonal to those of the main cIM (mobility separation region). This arrangement results in the racetrack shape of the cIM device rather than a uniform circle [32].

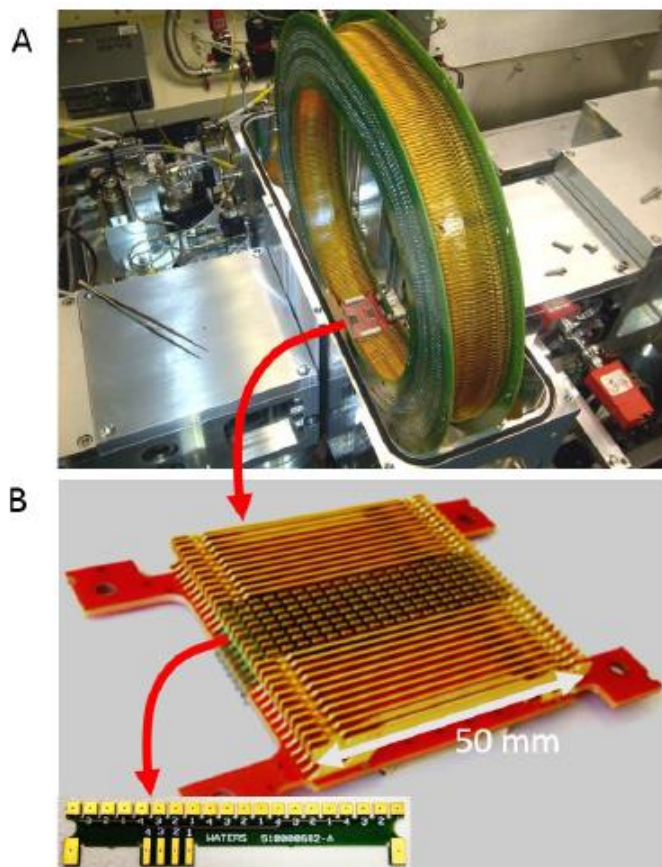


Figure 1.8. The cIM instrument photographs. (A) the cIM device. (B) The multi-function array. The segmented array electrodes are made from PCBs (inset) soldered to the PCB substrate (red). Reprinted from Giles et al. [32]. © Copyright 2019, American Chemical Society; *ACS AuthorChoice*.

The cyclic structure of the mobility cell allows for multi-pass experiments that can improve the separation by lengthening the path that ions travel [32]. However, increasing the number of passes through the cyclic cell can complicate the separation by a phenomenon called “wrap around”. Wrap around is defined as the complexity of the ion mobility data when ions with higher mobility and resulting higher speed travel additional passes through the cyclic cell and reach the detector later than the slower (less mobile) ions. As a result, the ions of higher mobilities will appear at the same or higher drift times than the ions of lower mobilities [32,41]. Breen et al. [41] developed a method for unwrapping the “wrap arounds” to take advantage from the improved separation of multi-pass experiments in cyclic ion mobility as a comprehensive technique. For this purpose, they performed ion mobility studies on a mixture of nine siloxane homologues (1-9) using GC-cIM-MS. The result of this study is provided in Figure 1.9 containing the drift time-retention time (DT-RT; Figure 1.9a-c) and drift time-mass to charge (DT-m/z; Figure 1.9d-f) contour plots in three different mobility separation times (2, 6 and 14 milliseconds) [41].

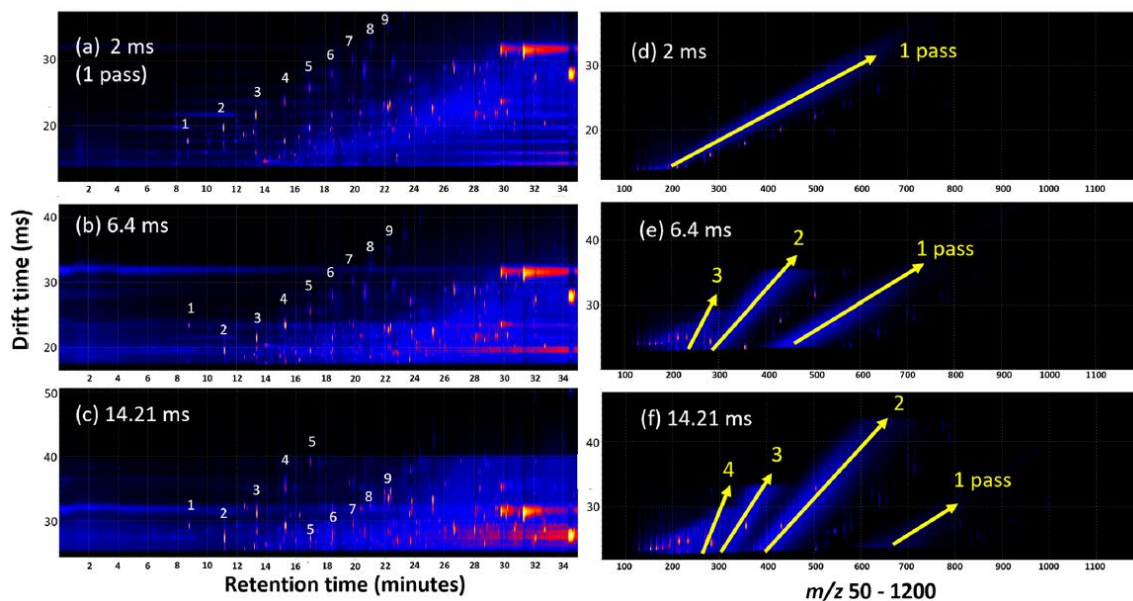


Figure 1.9. Contour plots displaying gas chromatographic retention time (minutes) vs ion mobility drift time when separation times of (a) 2, (b) 7, and (c) 14 ms are used; Panels (d)–(f) display m/z vs ion mobility

drift time for the same experiments. Reprinted from Breen et al. [41] © Copyright 2022, American Chemical Society.

Figure 1.9a displays the DT-RT contour plot of the (1-9) siloxane mixture with a total mobility separation time of 2 milliseconds which allows for a single pass of all homologues through the cyclic cell. The cIM signals corresponding to these structures fall upon a diagonal line which can be explained by the effect of lengthening the siloxane chain (from homologue 1 to 9) on the retention time and mobility. The longer chains possess higher retention times and lower mobilities (higher drift times). When the mobility separation time is increased to 6 milliseconds (Figure 1.9b), “wrap around” takes place by the drift shift of the siloxane ions 1 as they appear at a longer drift time than the siloxane ions 2. Increasing the mobility separation time to even a higher value (14 milliseconds; Figure 1.9c) lets the ions 1 travel three passes and wrap around twice and ions 2-4 travel two passes and wrap around once while ions 6-9 travel only one pass. The population of ions 5 splits into two groups with one group travelling two passes and the other travelling one pass [41].

The drift time of the ions is also correlated to their mass to charge ratios and Figure 1.9d displays this linear relationship for the 1-9 siloxane mixture in 2 milliseconds separation time. When all ions travel a single pass through the cyclic cell, all peaks form one linear region in the DT- m/z contour plot showing that ions of greater masses can be characterized by longer drift times. However, when the separation increases to 6 and 14 milliseconds (Figure 1.9e-f), two and three linear regions appear in contour plots, respectively. The wrap around reveals itself by forming multiple bands (linear regions) of peaks. The slope of each linear band of peaks is directly correlated to the number of passes ions travel through the cIM. Thus, the greater number of passes through the cIM results in higher slopes of the linear bands, shown in Figure 1.9e-f [41].

The drift times measured by the cIM instrument cannot show the distance each group of ions travel through a single experiment performed at one separation time point. However, multiple experiments at different separation times (Figure 1.9) can reveal the number of passes each group of ions travel through the cIM. Based on the data shown in Figure 1, Breen et al. [41] suggested a simplified solution to unwrap the wrap arounds that requires the determination of the periodic drift time (t_{1p}) and “zero-pass” time of the ions (t_{0p}). Periodic drift time (t_{1p}) is the time each ion requires to travel a single pass through the cyclic cell which has a linear relationship with the arrival time (t_a) that is shown as the drift time measured by the cIM. The “zero-pass” time (t_{0p}) is the time each ion requires to travel the distance between the trap and TOF through which it “bypasses” the cIM and the mobility separation does *not* occur. Then, to find the number of passes (n) each ion travels during a mobility separation, the following equation can be used [41]:

$$t_a = t_{0p} + nt_{1p} \quad (\text{Eq 1.2})$$

Breen et al. [41] also applied this process to complex mixtures of chemicals using an R-based script to align the ion mobility data according to m/z and retention time. Figure 1.10a-d shows how this unwrapping solution helped to simplify the wrapped data. Hence, it provides users with a comprehensive application of multi-pass experiments with cyclic ion mobility to take advantage of improved separations [41].

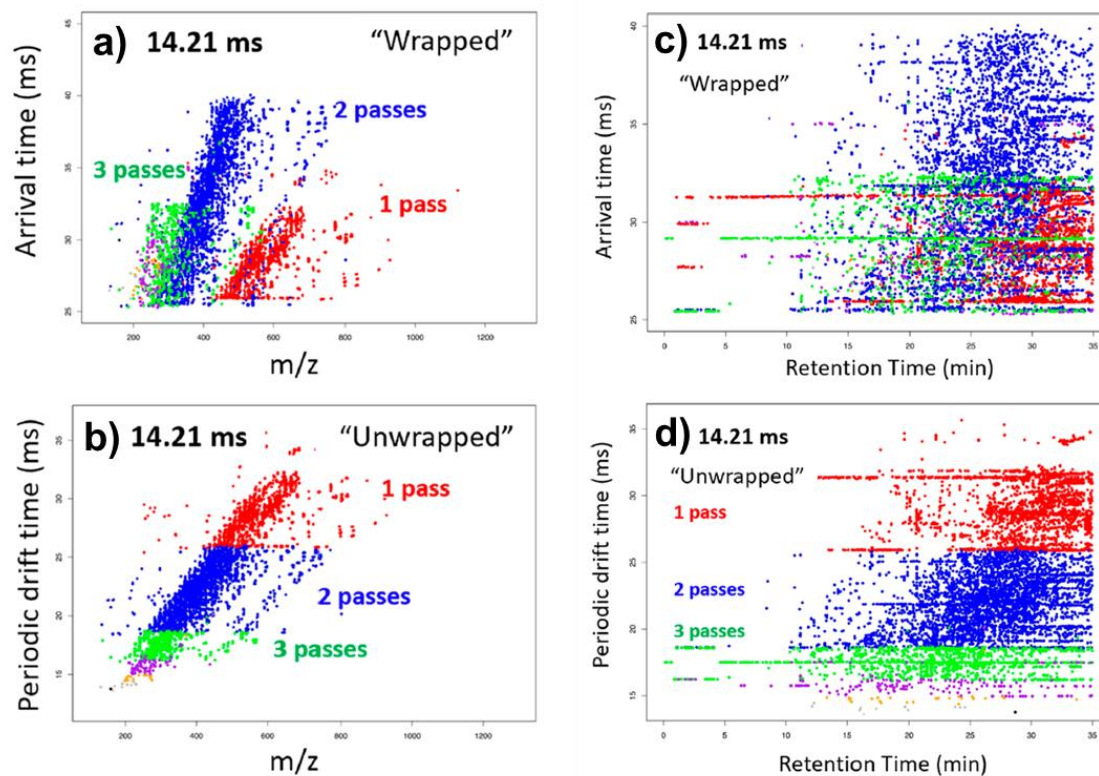


Figure 1.10. The drift time versus mass to charge plot (a) where the wrap-around effect is unwrapped in (b) by extrapolating the number of passes experienced by each ion and the drift time versus retention time plot (c) obtained from GC-cIM, and unwrapped results are shown in plot (d). Reproduced from Breen et al. [41] © Copyright 2022, American Chemical Society.

1.3. Computational chemistry

Computational chemistry provides an elegant and accurate set of techniques to investigate chemical problems using computing resources. Computational chemistry can predict molecular geometries, total energies and thermodynamic properties (including reactants, products, intermediates and transition states), chemical reactivity indicators (e.g. charge distribution), as well as properties measured by a variety of analytical and spectroscopic techniques [42]. The main tools used to investigate these properties are classified into two broad categories: *ab initio* methods and

density functional theory (DFT). The fundamental basis of both methods is solving the Schrödinger equation to find the energy and wavefunction of a structure (shown in Eq. 1.3; where \hat{H} stands for the Hamiltonian operator, Ψ for the wavefunction and E for the energy). However, the Schrödinger equation cannot be solved exactly for structures containing more than one electron due to the “electron correlations”. Electron correlations are defined as the instantaneous electron-electron repulsions that explain how the motion of each electron is correlated to the instantaneous positions of its neighboring electrons. Thus, both *ab initio* and DFT calculations involve applying approximations on the Schrödinger equation [43–45].

$$\hat{H} \Psi = E \Psi \quad \text{eq. 1.3}$$

Ab initio methods use quantum mechanics to make approximations on the Schrödinger equation. Prior to *ab initio* approximations, Hartree-Fock (HF) method offered an approximate solution to the Schrödinger equation by ignoring the electron correlations. In HF calculations, the instantaneous electron-electron repulsions are replaced by the repulsions each electron experience from the average position of the other electrons [43,44]. Therefore, the correlated motions of electrons that avoid each other more than what HF theory suggests result in a lower energy than the value calculated by the HF method. The energy difference between the HF energy and the exact energy is called the “correlation energy” [43–45]. The *ab initio* approximation techniques were then developed to account for both HF energy and the approximate correlation energy while calculating the energy of a multi-electronic structure. The most common *ab initio* techniques used to serve this purpose are configuration interaction (CI), Møller–Plesset perturbation theory (MP) and coupled cluster theory (CC) [44]. The main limitation of ab initio methods is their high computational cost that significantly increases the calculation time for large molecules [42,46].

Density functional theory (DFT) uses the relationship between the density of electrons and the total energy of an electronic structure to perform energy calculations. While the HF methods are based on calculating the wavefunction, DFT calculates the total electronic energy in addition to the electronic density distribution [45]. In 1964, Hohenberg and Kohn [47] showed that ground state energy of an electronic system is determined by the electron density. The main advantage of DFT method over the conventional wavefunction approaches (*ab initio* methods) can be explained by the lesser number of required variables. The wavefunction of an electron system containing N number of electrons is dependent on 4N variables with three spatial (x,y,z) and one spin coordinate for each electron. The total electron density is the square of the wavefunction integrated over three spatial coordinates (x,y,z), independent of the number of electrons. Therefore, despite the complexity of the wavefunctions caused by increasing the number of electrons (and the corresponding 4N variables), the electron density remains independent of the system size having the same number of (three) variables. Then, the only challenge for DFT calculations was designing the functionals connecting the electron density with the energy [44]. It should be noted that a “function” (shown with $f(x)$) relates a set of variables (coordinates) to a scalar quantity and a “functional” (shown with $F[f(x)]$) relates a function to a scalar quantity [43,44]. Thus, the wavefunction ($\Psi(r)$) and electron density ($\rho(r)$) are “functions” and accordingly, the energy depending on a wavefunction ($E[\Psi(r)]$) /electron density ($E[\rho(r)]$) is a “functional” [44]. In the simplest case of a DFT calculation, energy would only depend on the electron density. However, energy is also dependent on the derivatives of the electron density in a more general form. Hence, using the DFT methods, energy functional is defined as the sum of two terms:

$$E[\rho(r)] = \int V_{\text{ext}}(r) \rho(r) dr + F[\rho(r)] \quad \text{eq. 1.4}$$

In Eq. 1.4, V_{ext} stands for the external potential that electrons experience due to their Coulomb interaction with the nuclei ($\int V_{\text{ext}}(\mathbf{r}) \rho(\mathbf{r}) d\mathbf{r}$ is also shown as $V_{\text{ne}}[\rho(\mathbf{r})]$ or nuclear-electron functional) and $F[\rho(\mathbf{r})]$ stands for the combination of the kinetic energy of the electrons and interelectronic interactions. Nevertheless, the exact equation for $F[\rho(\mathbf{r})]$ remained unknown until Kohn and Sham [48] proposed the $F[\rho(\mathbf{r})]$ as an approximate sum of three terms indicated in Eq. 1.5 [45].

$$F[\rho(\mathbf{r})] = E_{\text{KE}}[\rho(\mathbf{r})] + E_{\text{H}}[\rho(\mathbf{r})] + E_{\text{XC}}[\rho(\mathbf{r})] \quad \text{eq. 1.5}$$

In Eq. 1.5, $E_{\text{KE}}[\rho(\mathbf{r})]$ (also shown as T_e) is the kinetic energy, $E_{\text{H}}[\rho(\mathbf{r})]$ is the electron-electron Coulombic energy and $E_{\text{XC}}[\rho(\mathbf{r})]$ is the “exchange-correlation” energy [45]. Kohn and Sham [48] pointed that the $E_{\text{KE}}[\rho(\mathbf{r})]$ is the kinetic energy of a system of *non-interacting* electrons which has the same density as a real electron system (that contains *interacting* electrons) [45,48]. $E_{\text{H}}[\rho(\mathbf{r})]$ is also called the Hartree electrostatic energy since it is equal to the whole pairwise electron-electron interactions while ignoring the electrons motions as proposed by Hartree. Before proceeding to explain the “exchange-correlation” energy, we should describe the exchange energy briefly. One of the main challenges with the initial Hartree method was that Hartree assigned each specific electron to a specific orbital while based on the antisymmetry principle, electrons should be indistinguishable. Hartree’s assumption complicated the calculations when exchanging two electrons was giving a completely different wavefunction [45]. To simplify these calculations, Slater [49] represented the wavefunction in a determinant form that satisfies the antisymmetry principle in a way that exchanging any two electrons (any two rows of the determinant) changes the sign of the determinant. The calculated energy of an electron system that satisfy the antisymmetry principle for exchanging the electrons (such as the ones resulting from Slater determinants) is called “exchange energy” [44,45].

The exchange-correlation energy is the combination of an exchange and a correlation component. The simplest way to calculate the exchange component is called the local density approximation (LDA) that is based on the “uniform electron gas” model, in which the electron density is assumed to be constant throughout the space. This method can be extended to local spin density approximation (LSDA) that also accounts for the electron systems containing unequal density of opposite spins (α and β). These methods required improvements by considering a non-uniform gas density, for which the exchange-correlation energy is not only dependent on the density but also the derivatives of the density. Gradient corrections with the well-known generalized gradient approximation (GGA) method offered this set of improvements by including the first derivative of the density [43–45]. Becke [50] proposed a (GGA) gradient correction for the LSDA exchange functionals that is shown as B or B88, see Eq. 1.6. Then, the general form of energy can be defined as a combination of LSDA, “exact” exchange and a gradient correction term. The exact exchange energy is defined as the energy obtained from the Slater determinant of the Kohn-Sham orbitals which is an almost equal value to the HF calculated energy. For this reason, when the “exact” exchange energy is involved in DFT calculations, the applied method is called a *hybrid* method (or *hybrid* Hartree-Fock/density functional method) [44].

The applied DFT (hybrid) functional in this thesis is called a B3LYP functional that uses Eq. 1.6. to calculate the exchange-correlation energy.

$$E_{XC}^{B3LYP} = (1 - a)E_X^{LSDA} + aE_X^{HF} + b\Delta E_X^{B88} + (1 - c)E_C^{LSDA} + cE_C^{LYP} \quad \text{eq. 1.6}$$

In Eq. 1.6, the three variables (a, b and c) are empirical coefficients that are the origin of “3” in the acronym. Becke’s gradient correction (B88) [51] is used for the exchange energy (the combination of the Hartree-Fock (HF) and LSDA exchange (X) energy). Then, the correlation

(C) energy is provided from the LSDA and the gradient correction by the LYP (Lee, Yang, and Parr [52]) functional that is determined by the $\nabla^2\rho$ [43–45].

1.3.1. Calculation of thermodynamic properties

Thermodynamic studies of ion-molecule reactions can be studied by energy calculations in addition to the instrumental analysis. The exothermicity and endothermicity of each reaction (determined by the energy levels of the reactants, products and intermediate minima) determines whether it can occur. Computational methods were applied in this study to simulate the proposed mechanisms of the ion molecule reactions prior to experiment.

The DFT calculations start with optimizing the geometry of an ion or molecule. The geometry optimization procedure consists of iterative processes during which the positions of atoms in a molecule/ion are altered repeatedly to obtain the minimum energy structure on the potential energy surface (PES). Then, the stability of the resulting geometry is verified by performing frequency calculations. The vibrational frequencies generated by this set of calculations are used to determine the identity of minima (real frequencies) and transition states (one imaginary frequency). Intrinsic reaction coordinates (IRC) calculations can be performed to confirm the identity of the transition structures. IRC calculations examine the reaction path by following the imaginary frequency that connects the transition structure to the minima on the PES.

The accuracy and cost of the energy calculations depend on two factors: the approximation made on the electron correlation energy (DFT in this study) and the choice of basis set. As the first factor was discussed previously, the basis sets will be explained briefly.

Each basis set consists of the mathematical functions that describe the orbitals of a molecule. The ideal number of functions is “infinite” which requires costly computational

resources. To solve this, the minimum basis sets (single-zeta basis sets) are defined as the ones containing one basis function for each formally or partially occupied orbital in a given molecule. However, the minimum basis set is inadequate due to the calculations' failure of the closest nucleus-core electrons distances and in the delocalization of valence electrons. The solution for this limitation is doubling or tripling the size of the basis set to create a double-zeta (DZ) or triple-zeta (TZ) basis set. For instance, the applied method for energy calculations in this study was a B3LYP in combination with CBSB7 functional that has the form of a 6-311G (2d,d,p) basis set. This basis set consists of a single "s" basis function for the core electron region (6: six s orbitals), a TZ basis function generated from splitting the valence space into three basis functionals (311: three, one, and one sets of $sp_xp_y p_z$ orbitals, respectively), and four sets of polarization functions (2d,d,p). The polarization functions are necessary due to the inadequate flexibility of multi-zeta basis sets to describe the electron distribution [43].

1.3.2. Prediction of collision-cross section values

Collision cross section (CCS) was previously discussed as the average surface area (\AA^2) available for colliding with buffer gas molecules that determines the drift time in ion mobility spectrometry. The direct semi-linear relationship between CCS and drift time can provide the experimental CCS values obtained from the ion-mobility instrument when the calibration curve (CCS/DT) is plotted [53]. These CCS values can be theoretically calculated prior to ion mobility experiments by using CCS prediction tools. Currently available CCS prediction methods can be classified into two groups of machine learning-based models and molecular dynamics methods.

To find the relationship between the inputs and the CCS values (output), machine learning-based models can be used. Trained models are obtained from datasets. Then, a testing dataset is

used to evaluate the efficiency of the trained model (Plante et al. [59]). The main limitation of the existing models is that the accuracy of predicted CCS values highly depends on the training dataset. Thus, the accuracy of the CCS prediction of a very different structure from the ones applied for training datasets falls outside a reliable range. For instance, MetCCS (metabolites) [54], LipidCCS (Lipids) [55], LiPydomics (Lipids) [56], AllCCS (mostly biological and small molecules) [57], ANN (pesticides) [58], and DNN (biological molecules) [59] that are the currently available models for CCS prediction are remarkably limited to the structures that were/are of biological interest which furtherly limits their applications in environmental studies.

Molecular dynamics (MD) applies the laws of motion on a simulated complex system of N particles [42,60]. These simulations start with the initial positions and velocities while the initial velocities of all particles are assumed to be equal. The calculations aim for the changes in velocities and directions affected by intermolecular interactions. Thus, they are used for studying the motions of the components in a dynamic system, including a complex mixture of molecules and different sides of a single large molecule [60,61]. Moreover, quantum molecular dynamics can simulate the actual chemical reactions [42]. For CCS predictions, MD is used to simulate the changes in position and velocity of ions during their non-reactive collisions with the buffer gas molecules. These methods are not limited by training datasets, but are highly demanding for costly computational resources for complex and large molecules.

The first application of molecular dynamics for calculating the theoretical CCS values was in 1996 when Mesleh et al. [62] built MOBCAL based on the kinetic theory of gases to compute the rotationally averaged cross sections. MOBCAL can use either of the three fundamental algorithms; projected area approximation (PA), exact/elastic hard sphere scattering (EHSS), and trajectory method (TM) [62]. MOBCAL provided the main fundamentals for further molecular

dynamics-based CCS prediction tools. For instance, IMoS (2014) was built based on the same theory as MOBCAL to calculate the CCS values but with a higher speed by applying more efficient and parallelized algorithms [63]. Collidoscope (2017) applies TM based algorithms in combination with an explicit modeling of scattering to reach a high accuracy and computational efficiency [64]. HPCCS (2018) performs efficient and parallel computations using TM algorithm to calculate the theoretical CCS values of significantly large molecules with a high accuracy [65]. ISiCLE (in silico chemical library engine, 2019) uses chemical identifiers as input and applies simulations based on molecular dynamics, quantum chemistry and ion mobility calculations to predict the CCS values and generate libraries. ISiCLE applies a TM algorithm to calculate the CCS values of the optimized geometries (by DFT) from the generated 3D structures with a high efficiency. This results in differentiations between conformational isomers of small molecules. This method is highly efficient but limited to small-sized molecules [66]. Finally, MobCal-MPI (2019) have been developed based on TM algorithms in parallel computing architectures to predict CCS values using atom specific parameters. MobCal-MPI requires DFT calculations using B3LYP on a 6-31++G(d,p) basis set, in which (++) show the diffusion functions. The DFT calculation results provide information on the distribution of partial charges that are required for TM simulations and CCS predictions by MobCal-MPI. MobCal-MPI is a fast, efficient and accurate method for a wide variety of organic compounds containing C, H, O, P, Cl, F, Br, I, and N atoms [67]. Hence, it was selected for predicting the CCS values of environmental pollutants in this study.

Although computational chemistry allows for the simulation of chemical structures and reactions, it cannot replace all experimental studies. Computational chemistry can minimize the required time, cost and resources for experiments while the experiments provide complementary supports for the computational results [42].

1.4. Objectives

In this study, the mechanisms of the ion-molecule reactions between organic pollutants and oxygen species in an APCI source have been studied using a combination of computational techniques and instrumental analysis. Density functional calculations were performed to provide theoretical supports for proposed mechanisms and GC-APCI-cIM-MS was applied for further structural studies. The combination of theoretical and experimental studies on these mechanisms provides a useful tool to discover whether the ion-molecule reactions are selective towards toxic structures. The resulting diagnostic tool can have potentially expanded applications for two classes of chemicals (triaryl phosphates and polyhalogenated dibenzo-p-dioxins). The importance of this tool is in its capability of differentiating between toxic and non-toxic isomers of unknown structures which belong to either of these two classes of compounds. Furthermore, when enough toxicological information is available for ranking different isomers based on their levels of toxicity, the ion mobility results can link the structures of the product ions to the corresponding level of toxicity.

References

- [1] F.W. Karasek, O. Hutzinger, S. Safe, *Mass Spectrometry in Environmental Sciences*, Plenum press, New York, 1985.
- [2] T. Portolés, E. Pitarch, F.J. López, F. Hernández, W.M.A. Niessen, Use of soft and hard ionization techniques for elucidation of unknown compounds by gas chromatography/time-of-flight mass spectrometry, *Rapid Commun. Mass Spectrom.* 25 (2011) 1589–1599. <https://doi.org/10.1002/rcm.5028>.
- [3] A.H. Grange, F.A. Genicola, G.W. Sovocool, Utility of three types of mass spectrometers for determining elemental compositions of ions formed from chromatographically separated compounds, *Rapid Commun. Mass Spectrom.* 16 (2002) 2356–2369. <https://doi.org/10.1002/rcm.842>.
- [4] A. Carrasco-Pancorbo, E. Nevedomskaya, T. Arthen-Engeland, T. Zey, G. Zurek, C. Baessmann, A.M. Deelder, O.A. Mayboroda, Gas chromatography/atmospheric pressure chemical ionization-time of flight mass spectrometry: Analytical validation and applicability to metabolic profiling, *Anal. Chem.* 81 (2009) 10071–10079. <https://doi.org/10.1021/ac9006073>.
- [5] D.M. Whitacre, *Reviews of Environmental Contamination and Toxicology*, Springer US, 2011. <https://www.ptonline.com/articles/how-to-get-better-mfi-results>.
- [6] A.R. Fernandes, W. Vetter, C. Dirks, L. van Mourik, R. Cariou, J. Sprengel, N. Heeb, A. Lentjes, K. Krätschmer, Determination of chlorinated paraffins (CPs): Analytical conundrums and the pressing need for reliable and relevant standards, *Chemosphere.* 286 (2022). <https://doi.org/10.1016/j.chemosphere.2021.131878>.

- [7] E.C. Meurer, A.A. Sabino, M.N. Eberlin, Ionic transacetalization with acylium ions: A class-selective and structurally diagnostic reaction for cyclic acetals performed under unique electrospray and atmospheric pressure chemical ionization in-source ion-molecule reaction conditions, *Anal. Chem.* 75 (2003) 4701–4709.
<https://doi.org/10.1021/ac0344384>.
- [8] M. Marinas, E. Sa, M.M. Rojas, M. Moalem, F.J. Urbano, C. Guillou, L. Rallo, A nuclear magnetic resonance (^1H and ^{13}C) and isotope ratio mass spectrometry ($\delta^{13}\text{C}$, $\delta^2\text{H}$ and $\delta^{18}\text{O}$) study of Andalusian olive oils, *Rapid Commun. Mass Spectrom.* 24 (2010) 1457–1466. <https://doi.org/10.1002/rcm>.
- [9] S. Fernando, M.K. Green, K. Organtini, F. Dorman, R. Jones, E.J. Reiner, K.J. Jobst, Differentiation of (Mixed) Halogenated Dibenzo-p-Dioxins by Negative Ion Atmospheric Pressure Chemical Ionization, *Anal. Chem.* 88 (2016) 5205–5211.
<https://doi.org/10.1021/acs.analchem.6b00255>.
- [10] I. van der Veen, J. de Boer, Phosphorus flame retardants: Properties, production, environmental occurrence, toxicity and analysis, *Chemosphere.* 88 (2012) 1119–1153.
<https://doi.org/10.1016/j.chemosphere.2012.03.067>.
- [11] H. de Ree, M. van den Berg, T. Brand, G.J. Mulder, R. Simons, B. Veldhuijzen van Zanten, R.H.S. Westerink, Health risk assessment of exposure to TriCresyl Phosphates (TCPs) in aircraft: A commentary, *Neurotoxicology.* 45 (2014) 209–215.
<https://doi.org/10.1016/j.neuro.2014.08.011>.
- [12] B. Patrizi, M.S. de Cumis, TCDD toxicity mediated by epigenetic mechanisms, *Int. J. Mol. Sci.* 19 (2018) 1–15. <https://doi.org/10.3390/ijms19124101>.

- [13] J.A. van Zorge, J.H. van Wijnen, R.M.C. Theelen, K. Olie, M. van den Berg, Assessment of the toxicity of mixtures of halogenated dibenzo-p-dioxins and dibenzofurans by use of toxicity equivalency factors (TEF), *Chemosphere*. 19 (1989) 1881–1890.
<https://www.unhcr.org/publications/manuals/4d9352319/unhcr-protection-training-manual-european-border-entry-officials-2-legal.html?query=excom> 1989.
- [14] R. Ishaq, C. Näf, Y. Zebühr, D. Broman, U. Järnberg, PCBs, PCNs, PCDD/Fs, PAHs and Cl-PAHs in air and water particulate samples - Patterns and variations, *Chemosphere*. 50 (2003) 1131–1150. [https://doi.org/10.1016/S0045-6535\(02\)00701-4](https://doi.org/10.1016/S0045-6535(02)00701-4).
- [15] A.R. Fernandes, M. Rose, D. Mortimer, M. Carr, S. Panton, F. Smith, Mixed brominated/chlorinated dibenzo-p-dioxins, dibenzofurans and biphenyls: Simultaneous congener-selective determination in food, *J. Chromatogr. A*. 1218 (2011) 9279–9287.
<https://doi.org/10.1016/j.chroma.2011.10.058>.
- [16] H.-R. Buser, Brominated and Brominated/Chlorinated Dibenzodioxins and Dibenzofurans: Potential Environmental Contaminants, *Chemosphere*. 1 (1987) 70–71.
- [17] K. Srogi, Levels and congener distributions of PCDDs, PCDFs and dioxin-like PCBs in environmental and human samples: A review, *Environ. Chem. Lett.* 6 (2008) 1–28.
<https://doi.org/10.1007/s10311-007-0105-2>.
- [18] M. Van Den Berg, L. Birnbaum, A.T.C. Bosveld, B. Brunström, P. Cook, M. Feeley, J.P. Giesy, A. Hanberg, R. Hasegawa, S.W. Kennedy, T. Kubiak, J.C. Larsen, F.X.R. Van Leeuwen, A.K.D. Liem, C. Nolt, R.E. Peterson, L. Poellinger, S. Safe, D. Schrenk, D. Tillitt, M. Tysklind, M. Younes, F. Wærn, T. Zacharewski, Toxic equivalency factors (TEFs) for PCBs, PCDDs, PCDFs for humans and wildlife, *Environ. Health Perspect.* 106

- (1998) 775–792. <https://doi.org/10.1289/ehp.98106775>.
- [19] S.P. Bhavsar, E.J. Reiner, A. Hayton, R. Fletcher, K. MacPherson, Converting Toxic Equivalents (TEQ) of dioxins and dioxin-like compounds in fish from one Toxic Equivalency Factor (TEF) scheme to another, *Environ. Int.* 34 (2008) 915–921. <https://doi.org/10.1016/j.envint.2008.02.001>.
- [20] M. Van den Berg, L.S. Birnbaum, M. Denison, M. De Vito, W. Farland, M. Feeley, H. Fiedler, H. Hakansson, A. Hanberg, L. Haws, M. Rose, S. Safe, D. Schrenk, C. Tohyama, A. Tritscher, J. Tuomisto, M. Tysklind, N. Walker, R.E. Peterson, The 2005 World Health Organization reevaluation of human and mammalian toxic equivalency factors for dioxins and dioxin-like compounds, *Toxicol. Sci.* 93 (2006) 223–241. <https://doi.org/10.1093/toxsci/kfl055>.
- [21] K.L. Organtini, A.L. Myers, K.J. Jobst, E.J. Reiner, B. Ross, A. Ladak, L. Mullin, D. Stevens, F.L. Dorman, Quantitative Analysis of Mixed Halogen Dioxins and Furans in Fire Debris Utilizing Atmospheric Pressure Ionization Gas Chromatography-Triple Quadrupole Mass Spectrometry, *Anal. Chem.* 87 (2015) 10368–10377. <https://doi.org/10.1021/acs.analchem.5b02463>.
- [22] A.L. Myers, S.A. Mabury, E.J. Reiner, Analysis of mixed halogenated dibenzo-p-dioxins and dibenzofurans (PXDD/PXDFs) in soil by gas chromatography tandem mass spectrometry (GC-MS/MS), *Chemosphere.* 87 (2012) 1063–1069. <https://doi.org/10.1016/j.chemosphere.2012.02.013>.
- [23] O.D. Sparkman, Z.E. Penton, F.G. Kitson, *Gas Chromatography and Mass Spectrometry*, 2011.

- [24] J. Abian, The coupling of gas and liquid chromatography with mass spectrometry, *J. Mass Spectrom.* 34 (1999) 157–168. [https://doi.org/10.1002/\(SICI\)1096-9888\(199903\)34:3<157::AID-JMS804>3.0.CO;2-4](https://doi.org/10.1002/(SICI)1096-9888(199903)34:3<157::AID-JMS804>3.0.CO;2-4).
- [25] J.M. Miller, *Chromatography: Concepts and Contrasts*, Wiley, 2005. <https://books.google.ca/books?hl=en&lr=&id=22CUljAmScC&oi=fnd&pg=PR5&dq=J.+M.+Miller,+Chromatography:+Concepts+and+Contrasts,+2nd+ed.,+New+York:+Wiley,+2009&ots=X2DQYBcsVv&sig=KY4FdcPkDQoHLMTwASMJb ppl5Vc#v=onepage&q&f=false>.
- [26] E. Heftmann, *Chromatography: Fundamentals and Applications of Chromatography and Related Differential Migration Methods*, Elsevier B.V, 2004.
- [27] D.A. Skoog, F.J. Holler, S.R. Crouch, *Principles of Instrumental Analysis*, Cengage Learning, 2007.
- [28] X. Li, F.L. Dorman, P.A. Helm, S. Kleywegt, A. Simpson, M.J. Simpson, K.J. Jobst, Nontargeted screening using gas chromatography– atmospheric pressure ionization mass spectrometry: Recent trends and emerging potential, *Molecules*. 26 (2021). <https://doi.org/10.3390/molecules26226911>.
- [29] D.B. Robb, T.R. Covey, A.P. Bruins, Atmospheric pressure photoionization: An ionization method for liquid chromatography-mass spectrometry, *Anal. Chem.* 72 (2000) 3653–3659. <https://doi.org/10.1021/ac0001636>.
- [30] N. Brenner, M. Haapala, K. Vuorensola, R. Kostianen, Simple coupling of gas chromatography to electrospray ionization mass spectrometry, *Anal. Chem.* 80 (2008) 8334–8339. <https://doi.org/10.1021/ac801406t>.

- [31] S.A. Schreckenbach, D. Simmons, A. Ladak, L. Mullin, D.C.G. Muir, M.J. Simpson, K.J. Jobst, Data-independent identification of suspected organic pollutants using gas chromatography-atmospheric pressure chemical ionization-mass spectrometry, *Anal. Chem.* 93 (2021) 1498–1506. <https://doi.org/10.1021/acs.analchem.0c03733>.
- [32] K. Giles, J. Ujma, J. Wildgoose, S. Pringle, K. Richardson, D. Langridge, M. Green, A Cyclic Ion Mobility-Mass Spectrometry System, *Anal. Chem.* 91 (2019) 8564–8573. <https://doi.org/10.1021/acs.analchem.9b01838>.
- [33] J.H. Gross, *Mass Spectrometry*, third, Springer US, 2004.
- [34] P.E. Miller, M.B. Denton, The quadrupole mass filter: Basic operating concepts, *J. Chem. Educ.* 63 (1986) 617–622. <https://doi.org/10.1021/ed063p617>.
- [35] A.W.N. Delgass, R.G. Cooks, Focal Points in Mass Spectrometry, *Am. Assoc. Adv. Sci.* 235 (1987) 545–553. <https://www.jstor.org/stable/1698677>.
- [36] S.D. Pringle, K. Giles, J.L. Wildgoose, J.P. Williams, S.E. Slade, K. Thalassinou, R.H. Bateman, M.T. Bowers, J.H. Scrivens, An investigation of the mobility separation of some peptide and protein ions using a new hybrid quadrupole/travelling wave IMS/oa-ToF instrument, *Int. J. Mass Spectrom.* 261 (2007) 1–12. <https://doi.org/10.1016/j.ijms.2006.07.021>.
- [37] A.T. Kirk, A. Bohnhorst, C.-R. Raddatz, M. Allers, S. Zimmermann, Ultra-high-resolution ion mobility spectrometry — current instrumentation , limitations , and future developments, *Anal. Bioanal. Chem.* (2019) 6229–6246.
- [38] B.J. Whitaker, State-selected and state-to-state ion-molecule reaction dynamics. Part1.

- Experiment: Advances chemical physics volume 82., John Wiley and Sons, Inc., New York, 1992.
- [39] K. Giles, S.D. Pringle, K.R. Worthington, D. Little, J.L. Wildgoose, R.H. Bateman, Applications of a travelling wave-based radio-frequency-only stacked ring ion guide, *Rapid Commun. Mass Spectrom.* 18 (2004) 2401–2414. <https://doi.org/10.1002/rcm.1641>.
- [40] K. Giles, J.P. Williams, I. Campuzano, Enhancements in travelling wave ion mobility resolution, *Rapid Commun. Mass Spectrom.* 25 (2011) 1559–1566. <https://doi.org/10.1002/rcm.5013>.
- [41] J. Breen, M. Hashemihedeshi, R. Amiri, F.L. Dorman, K.J. Jobst, Unwrapping Wrap-around in Gas (or Liquid) Chromatographic Cyclic Ion Mobility-Mass Spectrometry, *Anal. Chem.* 94 (2022) 11113–11117. <https://doi.org/10.1021/acs.analchem.2c02351>.
- [42] E.G. Lewars, *Computational Chemistry: Introduction to the Theory and Applications of Molecular and Quantum Mechanics*, Springer US, 2011. <https://doi.org/10.1002/jcc.540030214>.
- [43] S.M. Bachrach, *Computational Organic Chemistry*, Wiley, 2007.
- [44] F. Jensen, *Introduction to computational chemistry*, 2nd ed., Wiley, 2007.
- [45] A.R. Leach, *Molecular modelling principles and applications*, 2nd ed., Pearson, 2001.
- [46] H.F. Schaefer, Computers and molecular quantum mechanics: 1965-2001, A personal perspective, *J. Mol. Struct. THEOCHEM.* 573 (2001) 129–137. [https://doi.org/10.1016/S0166-1280\(01\)00539-5](https://doi.org/10.1016/S0166-1280(01)00539-5).
- [47] P. Hohenberg, W. Kohn, Inhomogeneous electron gas, *Phys. Rev.* (1964).

- <https://doi.org/10.1103/PhysRev.136.B864>.
- [48] W. Kohn, L.J. Sham, Self-consistent equations including exchange and correlation effects, *Phys. Rev.* (1965). <https://doi.org/10.1103/PhysRev.140.A1133>.
- [49] J.C. Slater, A simplification of the Hartree-Fock method, *Phys. Rev.* 81 (1951) 385–390. <https://doi.org/10.1103/PhysRev.81.385>.
- [50] A.D. Becke, Density-functional exchange-energy approximation with correct asymptotic behavior, *Phys. Rev.* (1988). <https://doi.org/10.1103/PhysRevA.38.3098>.
- [51] A.D. Becke, Density-functional thermochemistry. III. The role of exact exchange, *J. Chem. Phys.* 98 (1993) 5648–5652. <https://doi.org/10.1063/1.464913>.
- [52] C. Lee, W. Yang, R.G. Parr, Development of the Colle-Salvetti correlation-energy formula into a functional of the electron density, *Phys. Rev.* (1988). <https://doi.org/10.1103/PhysRevB.37.785>.
- [53] J.G. Forsythe, A.S. Petrov, C.A. Walker, S.J. Allen, J.S. Pellissier, M.F. Bush, N. V. Hud, F.M. Fernández, Collision cross section calibrants for negative ion mode traveling wave ion mobility-mass spectrometry, *Analyst.* 140 (2015) 6853–6861. <https://doi.org/10.1039/c5an00946d>.
- [54] Z. Zhou, X. Shen, J. Tu, Z.J. Zhu, Large-scale prediction of collision cross-section values for metabolites in ion mobility-mass spectrometry, *Anal. Chem.* 88 (2016) 11084–11091. <https://doi.org/10.1021/acs.analchem.6b03091>.
- [55] Z. Zhou, J. Tu, X. Xiong, X. Shen, Z.J. Zhu, LipidCCS: Prediction of Collision Cross-Section Values for Lipids with High Precision to Support Ion Mobility-Mass

- Spectrometry-Based Lipidomics, *Anal. Chem.* 89 (2017) 9559–9566.
<https://doi.org/10.1021/acs.analchem.7b02625>.
- [56] D.H. Ross, J.H. Cho, R. Zhang, K.M. Hines, L. Xu, LiPydomics: A Python Package for Comprehensive Prediction of Lipid Collision Cross Sections and Retention Times and Analysis of Ion Mobility-Mass Spectrometry-Based Lipidomics Data, *Anal. Chem.* 92 (2020) 14967–14975. <https://doi.org/10.1021/acs.analchem.0c02560>.
- [57] Z. Zhou, M. Luo, X. Chen, Y. Yin, X. Xiong, R. Wang, Z.J. Zhu, Ion mobility collision cross-section atlas for known and unknown metabolite annotation in untargeted metabolomics, *Nat. Commun.* 11 (2020) 1–13. <https://doi.org/10.1038/s41467-020-18171-8>.
- [58] L. Bijlsma, R. Bade, A. Celma, L. Mullin, G. Cleland, S. Stead, F. Hernandez, J. V. Sancho, Prediction of Collision Cross-Section Values for Small Molecules: Application to Pesticide Residue Analysis, *Anal. Chem.* 89 (2017) 6583–6589.
<https://doi.org/10.1021/acs.analchem.7b00741>.
- [59] P.L. Plante, É. Francovic-Fontaine, J.C. May, J.A. McLean, E.S. Baker, F. Laviolette, M. Marchand, J. Corbeil, Predicting Ion Mobility Collision Cross-Sections Using a Deep Neural Network: DeepCCS, *Anal. Chem.* 91 (2019) 5191–5199.
<https://doi.org/10.1021/acs.analchem.8b05821>.
- [60] K. Vollmayr-Lee, Introduction to molecular dynamics simulations, *Am. J. Phys.* 88 (2020) 401–422. <https://doi.org/10.1119/10.0000654>.
- [61] E. Saiz, M.P. Tarazona, Molecular dynamics and the water molecule: An introduction to molecular dynamics for physical chemistry students, *J. Chem. Educ.* 74 (1997) 1350–

1354. <https://doi.org/10.1021/ed074p1350>.
- [62] M.F. Mesleh, J.M. Hunter, A.A. Shvartsburg, G.C. Schatz, M.F. Jarrold, Structural information from ion mobility measurements: Effects of the long-range potential, *J. Phys. Chem.* 100 (1996) 16082–16086. <https://doi.org/10.1021/jp961623v>.
- [63] C. Larriba-Andaluz, C.J. Hogan, Collision cross section calculations for polyatomic ions considering rotating diatomic/linear gas molecules, *J. Chem. Phys.* 141 (2014). <https://doi.org/10.1063/1.4901890>.
- [64] S.A. Ewing, M.T. Donor, J.W. Wilson, J.S. Prell, Collidoscope: An Improved Tool for Computing Collisional Cross-Sections with the Trajectory Method, *J. Am. Soc. Mass Spectrom.* 28 (2017) 587–596. <https://doi.org/10.1007/s13361-017-1594-2>.
- [65] L. Zanutto, G. Heerdt, P.C.T. Souza, G. Araujo, M.S. Skaf, High performance collision cross section calculation-HPCCS, *J. Comput. Chem.* (2018) 1–7. <https://doi.org/10.1002/jcc.25199>.
- [66] S.M. Colby, D.G. Thomas, J.R. Nunez, D.J. Baxter, K.R. Glaesemann, J.M. Brown, M.A. Pirrung, N. Govind, J.G. Teegarden, T.O. Metz, R.S. Renslow, ISiCLE: A Quantum Chemistry Pipeline for Establishing in Silico Collision Cross Section Libraries, *Anal. Chem.* 91 (2019) 4346–4356. <https://doi.org/10.1021/acs.analchem.8b04567>.
- [67] C. Ieritano, J. Crouse, J.L. Campbell, W.S. Hopkins, A parallelized molecular collision cross section package with optimized accuracy and efficiency, *Analyst.* 144 (2019) 1660–1670. <https://doi.org/10.1039/c8an02150c>.

Chapter 2. Differentiating toxic and non-toxic tricresyl phosphate isomers using ion-molecule reactions with oxygen

Published in Journal of the American Society for Mass Spectrometry (JSMS)

Authors: Roshanak Amiri, Meera J. Bissram, Mahin Hashemihedeshi, Frank L. Dorman, David Megson, Karl J. Jobst*

* Corresponding Author

Abstract: Ortho-substituted isomers of tricresyl phosphates (TCPs) and their toxic metabolites (e.g., CBDP: cresyl saligenin phosphate) can cause neurotoxic effects in humans. When TCP is introduced to an atmospheric pressure chemical ionization (APCI) source using gas chromatography (GC), radical cations $M^{+\bullet}$ are formed by charge exchange. The mass spectrum of an ortho-substituted isomer displays two intense peaks that are absent in the spectra of non-ortho-substituted isomers, leading us to propose structure-diagnostic ion-molecule reactions between ions $M^{+\bullet}$ and oxygen species present in the source. However, the mechanism of these reactions has not yet been established. In this study, we propose a mechanism and provide support through computational and experimental analysis using density functional theory (DFT) and cyclic ion mobility-mass spectrometry (cIM-MS). The mechanism consists of a multi-step reaction starting with the rearrangement of the molecular ion into a distonic isomer followed by an oxidation step and then, decomposition into $[CBDP-H]^+$. This proposal is consistent with the results obtained from a series of isotopically-labelled analogues. Cyclic ion mobility experiments with a triorthocresyl phosphate standard, reveals the presence of at least two hydrogen shift isomers of the product ion $[CBDP-H]^+$ that are connected by a low-lying barrier. The selectivity of the ion-

molecule reactions towards ortho-substituted cresyl TCP isomers provides us with an identification tool that can select potentially neurotoxic tri-aryl phosphate esters present in complex mixtures that are produced in large volume by industry.

2.1. Introduction

Organophosphate esters (OPEs) have been used extensively as plasticizers, lubricant additives, anti-foaming agents and substitutes for banned halogenated flame retardants. [1–3] They have been identified in air and (indoor) dust particulate, water, soil, sediment, and biota. [2–6] Among aryl OPEs, triorthocresyl phosphate (ToCP) is infamous for its neurotoxicity. [7–9] The first observations of the neurotoxic effects of ToCP in humans involved contamination of foodstuffs, beverages, and drugs, resulting in pain, paresthesia, muscle weakness and paralysis. [10] More recent studies on human exposure to ToCP have focused on aircraft crews reporting headaches, loss of balance, numbness, and neurobehavioral abnormalities as the symptoms of so-called “aerotoxic syndrome”. [11,12] It has been suggested that aerotoxic syndrome is associated with the presence of ToCP in the lubricants used in jet engines. [13]

Tricresyl phosphates (TCP) with ortho-cresyl substituents exhibit greater neurotoxicity than their non-ortho counterparts. [14,15] This is because ortho-TCPs are biotransformed into toxic metabolites that cannot be generated from non-ortho substituted TCPs. For example, ToCP is metabolized to CBDP (cresyl saligenin phosphate (2-(ortho-cresyl)-4H-1,2,3-benzodioxaphosphorin-2-oxide)) by liver microsomal cytochrome P450 and serum albumin, see Scheme 2.1. CBDP is responsible for the neurotoxic effects of ToCP as it can irreversibly bind to human butyrylcholinesterase (hBuChE) and human acetylcholinesterase (hAChE). [16–18] Ortho substituted TCPs are also more reactive under ambient conditions, possibly because they undergo

atmospheric oxidation. [5,13] Consequently, the lifetime and probability of exposure of a TCP isomer depends on the number of ortho substituents. This may explain why longer lived mono-*o*-cresyl isomers and di-*o*-cresyl isomers respectively appear to be ten- and five-fold more toxic than ToCP. [5,19]

Differentiating between TCP isomers requires efficient separation. Commonly employed methods for identifying TCP in environmental samples involve gas or liquid chromatography-mass spectrometry (LC-MS or GC-MS). [20–24] Commercially produced OPEs are mixtures that likely contain hundreds of compounds, [25] few of which are available as authentic standards.

In a previous study by Megson et al., [26] the occurrence of TCPs and their alkylated homologues in fresh and used jet oil was investigated by comprehensive two-dimensional gas chromatography (GCxGC) coupled with atmospheric pressure chemical ionization (APCI) mass spectrometry (GCxGC-APCI). They observed that the APCI mass spectrum of ToCP displayed two additional peaks compared to those of trimeta- and triparacresyl phosphate. [26] Although a mechanism was not proposed, the authors suggest that ion-molecule reactions with oxygen may be selective towards ortho-substituted isomers. [27–30] Ion molecule reactions involving oxygen have been shown to differentiate isomeric ions in both positive [29] and negative ion modes. [27,28,30] In the present study, we employ density functional theory to elucidate the mechanism of these ion-molecule reactions in combination with complementary experiments on D-labeled ortho-substituted TCP isomers. This study aims to establish the mechanism of the ion-molecule reactions with oxygen (in both O₂ and O₃ forms) that is selective towards the ortho-substituted TCP isomers, leading to an approach to identify toxic, ortho-substituted isomers and congeners of TCP present in environmental samples.

2.2. Experimental Section

2.2.1. Chemicals and Sample preparation

Triortho, trimeta and triparasubstituted-cresyl phosphates (ToCP, TmCP, and TpCP) were obtained from TCI America. Tris 2-ethyl phenyl phosphate and D-labeled TCP isomers (Tri-CD₃-ortho-cresyl phosphate, mono-D₇-meta-diortho-cresyl phosphate, mono-D₇-ortho-dimetacresyl phosphate, mono-D₇-para-diortho-cresyl phosphate, mono-D₇-ortho-diparacresyl phosphate, di-D₇-meta-monoortho-cresyl phosphate, di-D₇-ortho-monometacresyl phosphate, di-D₇-para-monoortho-cresyl phosphate, and di-D₇-ortho-monoparacresyl phosphate; Table S2.3) were synthesized from phosphorous (V) oxychloride (Fisher Scientific) and the corresponding alcohols (*o*-, *m*- and *p*-cresols, TCI America; D₈-labelled *o*-, *m*- and *p*-cresol, CDN Isotopes; CD₃-labelled *o*-cresol, Toronto Research Chemicals; 2-ethylphenol, TCI America) using a method adapted from Huang *et al.*, 2017 [31]. Following Huang *et al.*'s procedure, the seven syntheses performed herein produced yields ranging from 50 to 75%.

2.2.2. Instrumental Analysis

The experiments were performed using a Waters Select Series Cyclic IMS ion mobility mass spectrometer (Wilmslow, UK) coupled to an Agilent 8890 Gas chromatograph using atmospheric pressure chemical ionization (APCI). Analyte separation was performed using either a Rtx-5HT column (15m×250µm×0.25µm) or a DB-XLB column was applied (15m×250µm×0.1µm). Most experiments were performed using an initial oven temperature set to 90 °C for 1 minute; then ramped to 115 °C at 95 °C/min, to 150 °C at 65 °C/min, to 210 °C at 45 °C/min, and to 330 °C at 35 °C/min, and finally held for 3.5 minutes with a total run time of 10 minutes. [32] For selected

GC experiments, the oven temperature was ramped to 325 °C at 27 °C/min and held for 6.3 minutes with a total run time of 16 minutes. Standard solutions (1 µL) were injected in the splitless mode. The inlet temperature was set to 280 °C and the helium carrier gas flow was set to 3 mL/min. GC eluent exiting the column was swept through the ion volume using a make-up flow of nitrogen (~99.99% purity) of 350 mL/min. Atmospheric pressure chemical ionization was performed under solvent free conditions by corona discharge (2 µA) in the positive mode. Analyte molecules were ionized by charge exchange with N₂⁺. The purity of the in-house nitrogen (99.99%) was too high to observe ion molecule reactions observed by Megson *et al.* [26] who employed a nitrogen generator yielding <99.5% purity. In the present study, we used dried compressed air as the auxiliary and cone gas to promote reactions with dioxygen. The source conditions were as follows: source temperature, 150 °C; sampling cone, 40 V; cone gas, 175 L/hour; auxiliary gas, 100 L/hour. Column bleed (C₉H₂₇O₅Si₅⁺ - m/z 355.0699) was used to internally correct the measured m/z. Mass spectra were collected for m/z 50 – 1200. The cyclic ion mobility cell was operated in the single pass mode, with a separation time set to 10.64 ms and a traveling wave height of 15 V. Calibration of the instrument to measure CCS was performed according to standard procedure using a mixture of 22 compounds (aka, “major mix”) supplied by Waters Corp. Multi-pass experiments were performed by increasing the separation time to 98.04 ms (8 passes) and 207.06 ms (16 passes). Collision-induced dissociation (CID) experiments were performed with nitrogen (collision energy (trap), 6 V; (transfer), 4 V) in the trap and transfer regions of the cIMS, which are located before and after the cyclic ion mobility cell, respectively.

2.2.3. Computational methods

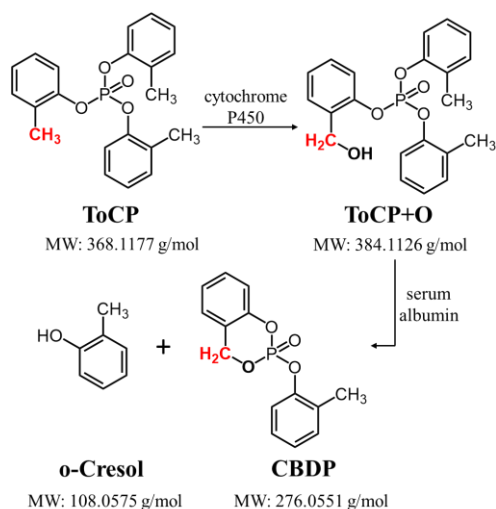
All computations were performed with the Gaussian g16 suite of programs on the Atlantic Computational Excellence network (ACEnet) cluster. The total energies of all ions and neutrals

were calculated using the B3LYP level of theory in combination with the 6-311G (2d,d,p) basis set. [33] The identity of local minima and connecting transition states (TS) was determined by frequency analysis and confirmed by intrinsic reaction coordinate (IRC) calculations. The total energies (in Hartree) and relative energies (in kcal/mol) for the molecular ions, product ions and neutrals are reported in Table S2.1, S2.2. The predicted collision cross section (CCS) values of all structures were calculated using the MobCal-MPI v1.2, on the SHARCNET platform. Geometry optimization prior to MobCal analysis was performed by DFT at the B3LYP/6-31++G(d,p) level of theory. Using the python module provided by Hopkins *et al.*, [34] in combination with Open Babel 2.4.1 [35] and sdf2xyz2sdf [36] packages, the output files from the geometry optimization were converted to input files for MobCal-MPI. The trajectory method (TM) was employed to simulate CCS measurements using N₂ as the buffer gas. [34]

2.3. Results and Discussion

2.3.1. Parallels between the metabolism of ToCP and its ion-molecule reactions with oxygen

Scheme 2.1 displays the two-step metabolism of ToCP. First, the cresyl methyl group is oxidized into an alcohol by the microsomal enzyme cytochrome P450. The next step involves ring-closure between the newly-formed hydroxyl group and the phosphate moiety. This process is catalyzed by serum albumin, and results in the formation of CBDP, a neurotoxic metabolite. Meta- and para-substituted isomers cannot undergo the same reaction, and consequently they are less toxic. Megson *et al.* [26] observed that the APCI mass spectrum of ToCP is characterized by two additional peaks absent in those of trimeta and triparacresyl phosphate. [26]



Scheme 2.1. The metabolism of ToCP (tri-ortho cresyl phosphate) into the toxic metabolite CBPD. [37]

Figure 2.1a displays the APCI (+) mass spectrum of ToCP. Compared to the mass spectra of TmCP and TpCP (Figs. S2.16 and S17), the spectrum of ToCP displays two additional mass peaks (m/z 383 and m/z 275) in Figure 2.1a, are only one mass unit less than those expected for the metabolites shown in Scheme 2.1. The additional peaks (m/z 383 and m/z 275) in Figure 2.1a, are only one mass unit less than those expected for the metabolites shown in Scheme 2.1. These peaks are observed when oxygen is present in the ion source, [30] (Figs. 2.1, and S2.6-2.17) and disappear when pure (>99.99%) nitrogen (Figure S2.18-2.30) is used as the cone and auxiliary gas. The selected ion chromatograms of isomers ToCP, TmCP and TpCP in Figure 2.2 indicate that only ToCP can produce m/z 275 product ions. The comparison between figure 2.2a and 2.2b shows that the ion molecule reaction involves the depletion of the molecular ion to produce the m/z 275 ions from ToCP. However, the abundance of the protonated ions remains the same during the reaction, which suggests that $[\text{ToCP}+\text{H}]^+$ does not participate in the ion-molecule reactions. The exact mass measured for m/z 275 deviates 1.1 ppm from the theoretical mass of $\text{C}_{14}\text{H}_{12}\text{PO}_4$, which contains one less hydrogen atom than the elemental composition of CBPD. The mass spectrum of ToCP (Figure 2.1a) also displays a negligible yield of molecular ions M^{*+} compared to those of

TmCP and TpCP (Figs. S2.7/S2.8), which suggests that almost all molecular radical cations ($M^{\bullet+}$) of ToCP have reacted with oxygen species present in the source. This is also reflected in the selected ion chromatograms of ions $M^{\bullet+}$ (m/z 368) and $[M+H]^+$ (m/z 369) shown in Figures 2.2a/b: the abundances of the $[M+H]^+$ ions of all three isomers are approximately equal, whereas the $M^{\bullet+}$ ions resulting from ToCP are depleted. These results suggest that oxygen reacts with the $M^{\bullet+}$ ions, whereas the $[M+H]^+$ quasimolecular ions probably do not play a significant role in the reaction.

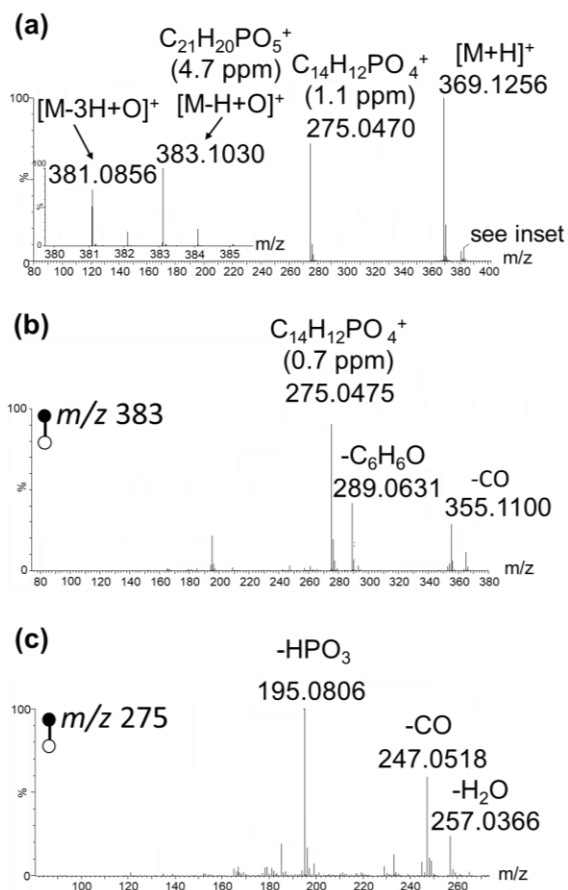


Figure 2.1. (a) APCI⁺ mass spectrum of ToCP (ToCP^{•+} radical cation [m/z 368.1177] was not observed); CID mass spectra of (b) m/z 383 and (c) m/z 275 ions generated from ToCP. Note: The m/z 275 region of the mass spectrum in (a) is magnified by 10-fold.

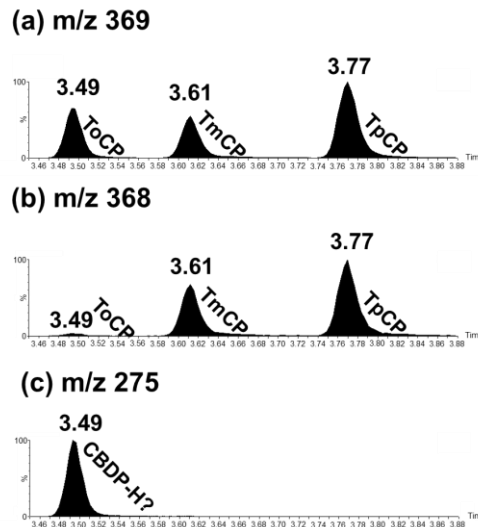


Figure 2.2. Selected ion chromatograms of (a) $[M+H]^+$ (m/z 369); (b) M^{*+} (m/z 368); and (c) $[C\text{BDP-H}]^+$ m/z 275 ions generated by an equimolar mixture of ToCP, TmCP and TpCP.

The m/z 383 product shown in Figure 2.1a (inset) deviates by 4.7 ppm from the theoretical mass of $C_{21}H_{20}PO_5$, which contains one less hydrogen atom than the metabolite generated in the first step of the metabolic process in Scheme 2.1. If the m/z 383 ions are intermediates in the ion-molecule reactions, then one would expect that the CID mass spectrum of m/z 383 would display an intense peak corresponding to ions with m/z 275. The observation from CID experiments (Figure 2.1b) is consistent with the proposal that ToCP radical cations react with oxygen to form m/z 383 ions $[M-H+O]^+$, which subsequently dissociate into $[C\text{BDP-H}]^+$ as the final product of the ion-molecule reactions. Unfortunately, the mass spectrum of the m/z 275 ion (see Figure 2.1c) is dominated by reactions (losses of H_2O , CO and HPO_3) that are not helpful in elucidating its structure.

At first glance, the ion-molecule reactions observed in Figure 2.1a parallel the metabolic process shown in Scheme 2.1. [38] In both, activation of a C-H bond at the ortho-methyl moiety is a key step. However, human metabolism of ToCP achieves C-H bond activation through enzyme catalysis, whereas the ion-molecule reactions appear to be uncatalyzed. Ayrton *et al.* [38] have

observed that uncatalyzed oxidation of saturated hydrocarbons can occur in an ambient corona discharge, under similar conditions to those used in our experiments, and leading to $[M-H+O]^+$ ions among other oxidation products. They argue that ozone is likely responsible for these oxidation processes, and this proposal is based on the observation that saturated hydrocarbons typically form abundant $[M-H]^+$ ions, which can readily react with ozone. We suspect that the mechanism of the ion-molecule reactions involving ToCP are different for three reasons. First, $[M-H]^+$ ions were not observed in the mass spectra of ToCP or its isomers, and it isn't immediately obvious why ozonation of the ortho-methyl group would be favoured over the meta- or para-isomers. Secondly, we observed depletion of the molecular ions M^+ of ToCP, which strongly suggests that the radical cation is the likely reactant. Third, organophosphate ester ions are likely to form long-lived, stable distonic ions [39] that may be reactive towards both molecular oxygen [29] and ozone.

2.3.2. Computational analysis of the mechanism

Figure 2.3 displays the energy diagram of the proposed mechanism for the ion-molecule reactions involving O_2 . The first step involves rearrangement of ion **TCP1** into its distonic isomer **TCP2** via a 1,6-H shift. The molecular ion must have at least 18 kcal/mol of internal energy to overcome the initial energy barrier. Upon charge exchange with N_2^{*+} (~15 eV), incipient TCP^{*+} ions will have 7 eV (~161 kcal/mol) of internal energy. However, most of the initial internal energy will be removed by collisional cooling. Stephens et al. [40] used a set of thermometer ions with well-defined dissociation energies to study the distribution of internal energies resulting from APCI. Their results suggest that the average internal energy of TCP^{*+} ions is approximately 30-40 kcal/mol, [40] which exceeds the 18 kcal/mol barrier required for transformation of **TCP1** into

TCP2. The radical site of the distonic isomer (**TCP2**) offers an attractive site for triplet O₂ to form a covalent bond. [29] This results in the generation of the remarkably stable ion **TCP3a**. The newly formed C-O bond is stabilized by at least 19 kcal/mol. Consequently, ion **TCP3a** can rearrange by low lying hydrogen shifts into **TCP4a** and **TCP5a**.

The next stage of the reaction involves the loss of [•]OH from **TCP5a** via a direct bond cleavage, which would explain the formation of [M-H+O]⁺ ions, as witnessed by the m/z 383 peak in Figure 2.1a. This reaction is predicted to be exothermic: the dissociation threshold (**TCP6** + [•]OH) lies 41 kcal/mol below the combined enthalpies of the reactants **TCP1** and O₂. However, our calculations also suggest that the loss of [•]OH is associated with a substantial kinetic barrier. To probe the transition state structure, we performed a relaxed scan of the potential energy surface along the peroxy bond. At each step of the calculation, the O-O bond was increased stepwise, while the remaining parts of the ion were allowed to optimize. Instead of a smooth direct bond cleavage reaction into **TCP6** + [•]OH, we found that this led to rearrangement of **TCP5a** into a terbody complex, **TBC1**, shown in Scheme 2.2.

The terbody complex **TBC1** consists of three discrete species, bound together non-covalently: a dicresyl phosphite radical cation complexed with a cresyl radical and a hydroxyl radical. Dissociation of ions **TBC1** by loss of a cresyl radical requires only 9 kcal/mol and the loss of a cresol molecule requires only 3 kcal/mol. It is important to note that cresyl radical loss, resulting in m/z 293 ions, is not observed experimentally. Therefore, we suggest that further rearrangement of ions **TBC1** must occur via pathways that do not exceed the energy requirements for loss of a cresyl radical. The calculations indicate that the least energy demanding route to loss of [•]OH from ions **TBC1**, see Scheme 2.2, involves migration of the cresyl radical in **TBC1** towards the dicresyl phosphite moiety, resulting in the formation of a phosphorous-oxygen bond.

Unfortunately, the barrier for this reaction exceeds the energy requirements for cresyl radical loss, a reaction that is not observed.

From the computed mechanism shown in Fig. 2.3, we conclude that the reaction between **TCP1** and O_2 can produce the observed m/z 383 ions, either from **TCP5a** via a direct bond cleavage, or via a rearrangement into the ter-body complex **TBC1**. However, the presence of a kinetic barrier seems to impede the formation of m/z 383 ions by this route, and the absence of m/z 293 in the mass spectrum (Fig. 2.1a) also casts doubt on this mechanism. One possible explanation is that the reaction does not involve dioxygen, but rather other oxygen species present in the source, such as ozone.

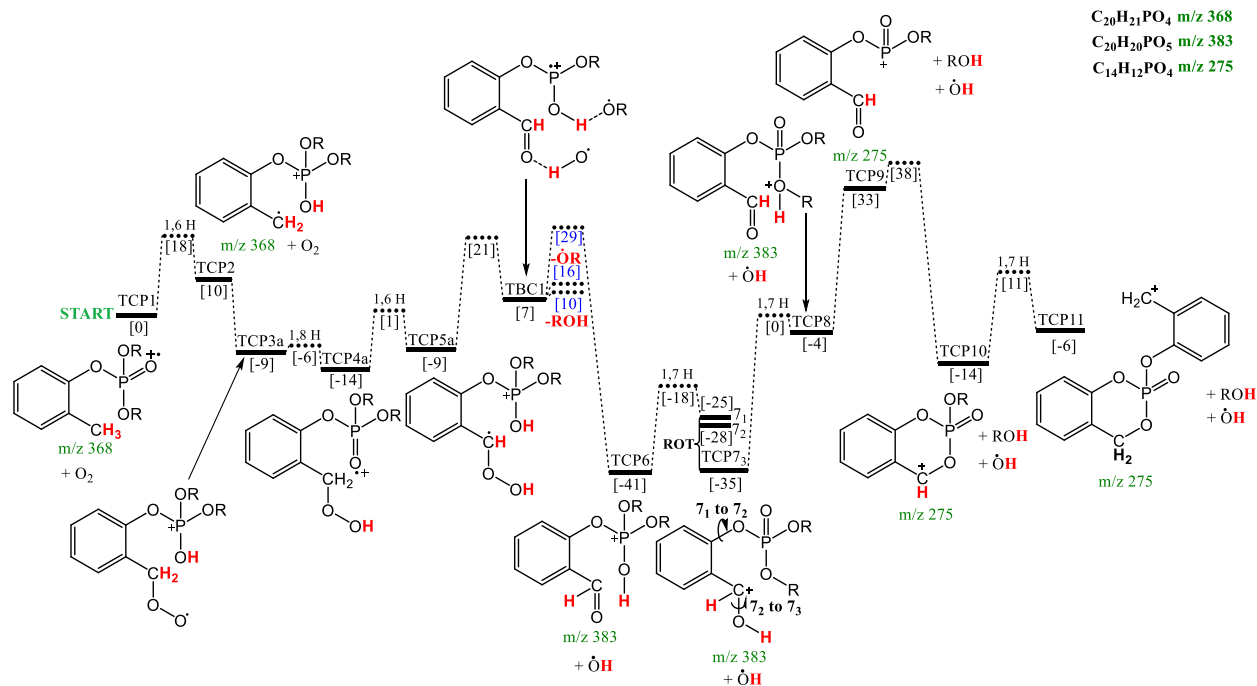
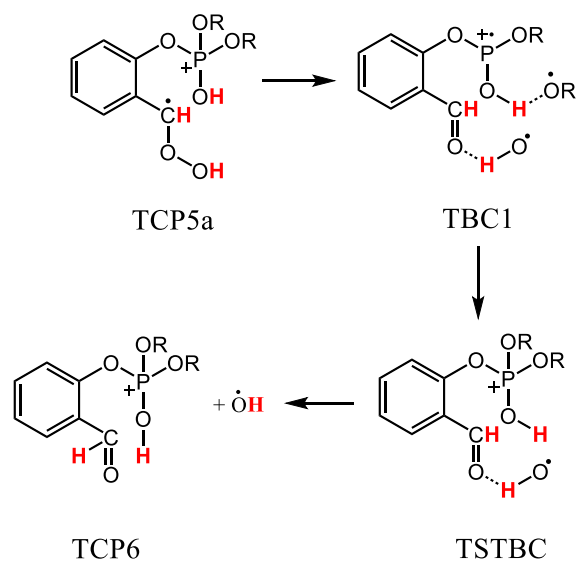


Figure 2.3. Energy diagram depicting the proposed mechanism for the ion-molecule reactions of $ToCP^+$ with O_2 . The numbers in square brackets are relative energies (in kcal/mol) from **Table S2.1**. Note: R represents the *o*-cresyl group.



Scheme 2.2. Rearrangement of TCP5a to TBC1 and TSTBC, resulting in the formation of TCP6+ ·OH.

Figure 2.4 displays the proposed ion-molecule reactions mechanism involving ozone. Most steps of this mechanism parallel those proposed in the reaction with O₂. The first step involves rearrangement of the molecular ion **TCP1** into its distonic isomer **TCP2**. Then, O₃ reacts with **TCP2**, by forming a strong C-O bond in ion **TCP3b** that is stabilized by 80 kcal/mol. Ion **TCP3b** can follow two possible paths to produce **TCP6** by loss of a peroxy radical (·OOH), resulting in the observed m/z 383 ions.

TCP3b could rearrange into **TCP6** via a circuitous route involving consecutive 1,9 H- and 1,6-H shifts (not shown), but the least energy demanding pathway involves a straightforward 1,4-H shift. Ion **TCP6** can then rearrange into **TCP8** via a 1,7 H-shifts and then decompose by loss of a cresol molecule to form m/z 275 ions **TCP9**. We note that **TCP9** can also ring-close into a more stable isomer, **TCP10**, which is closely similar in structure to CBDP. Overall, the formation of m/z 383 and m/z 275 from **TCP1** and ozone is highly exothermic: The CBDP analogue **TCP10** is generated with upwards of 88 kcal/mol of internal energy! Thus, **TCP10** can easily isomerize into **TCP11** via a low-lying 1,7-H shift, and we would therefore expect that the m/z 275 ions consist

of a mixture of at least two or more H-shift isomers. This hypothesis will be tested by ion mobility experiments described in **Section 2.3.4**. In the proposed mechanism, the hydrogens on the ortho methyl groups (shown in red in Figure 2.3) play a crucial role. **Section 2.3.3** explores the use of isotopically labeled analogues to support the proposed mechanism.

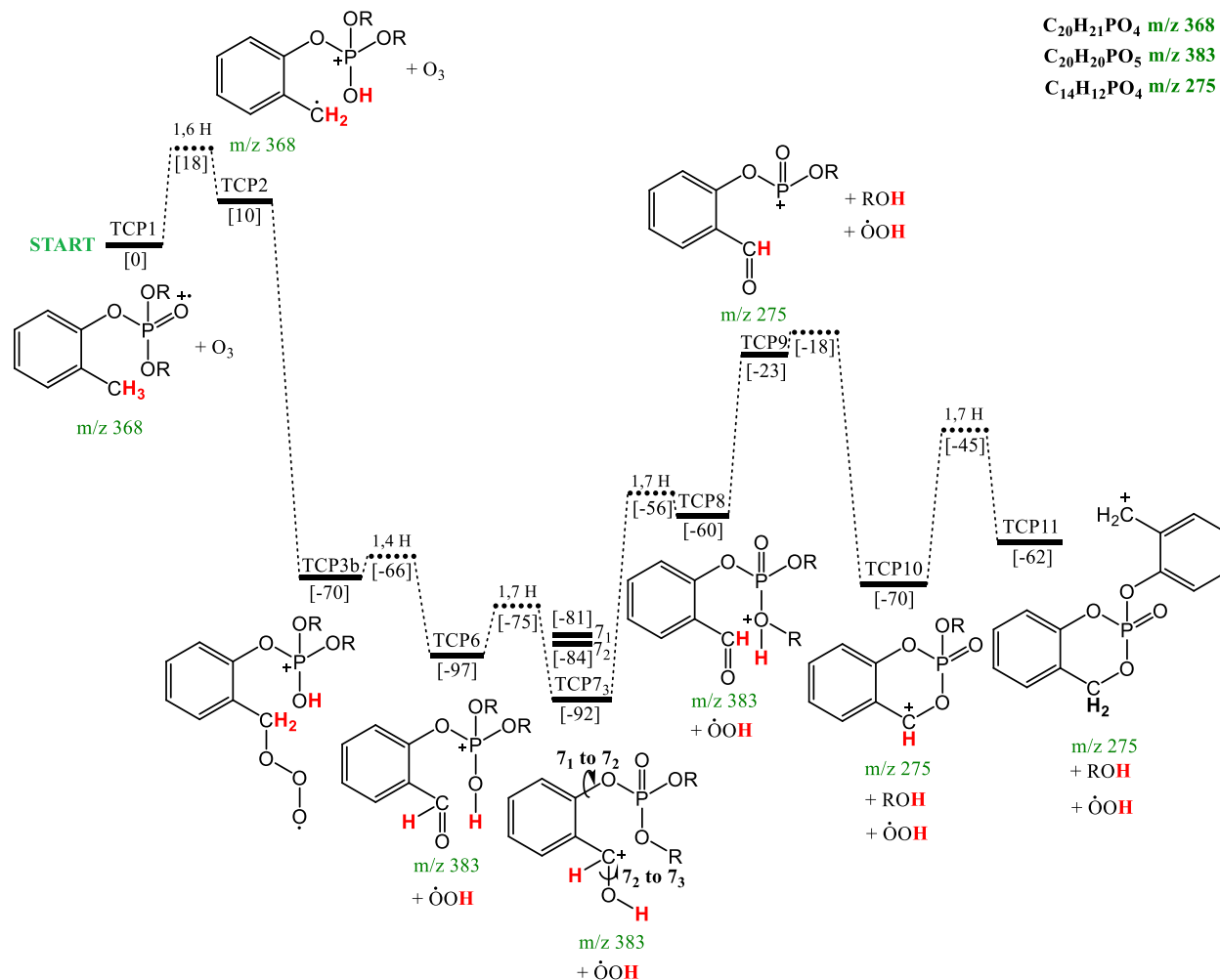


Figure 2.4. Energy diagram depicting the proposed mechanism for the ion-molecule reactions of ToCP⁺ with O₃. The numbers in square brackets are relative energies (in kcal/mol) from **Table S2.2**. Note: Each R represents the o-cresyl group.

2.3.3. Complementary experiments with (isotopically labeled) isomers and homologues

Isotopic labeling in mass spectrometry is a time-honored approach to study the mechanisms of ion-molecule reactions and dissociations.[41] This section describes experiments with the D-labeled ToCP analogues and isomers listed in Table S2.3 and S2.4. The identity of each synthetic product was confirmed initially by comparing the chromatographic behaviour with that of their unlabeled analogue. The deviations between theoretical and experimental m/z were within 5 ppm for all compounds. The proposed mechanism (Figure 2.4) suggests that the ortho-methyl hydrogen atoms play a crucial role in the reaction. Therefore, one would expect that experiments with CD_3 -labeled ToCP would result in mass shifted products compared to the reaction with unlabeled ToCP. Indeed, the APCI mass spectrum of CD_3 -labeled ToCP (Figure 2.5), displays peaks at m/z 390, corresponding to the loss of $^{\bullet}OD$ from the incipient ion molecule complex **TCP3b**, and m/z 279 which corresponds with the $[C_{BDP-D}]^+$ ions. These observations are consistent with the mechanistic proposal shown in Figure 2.4.

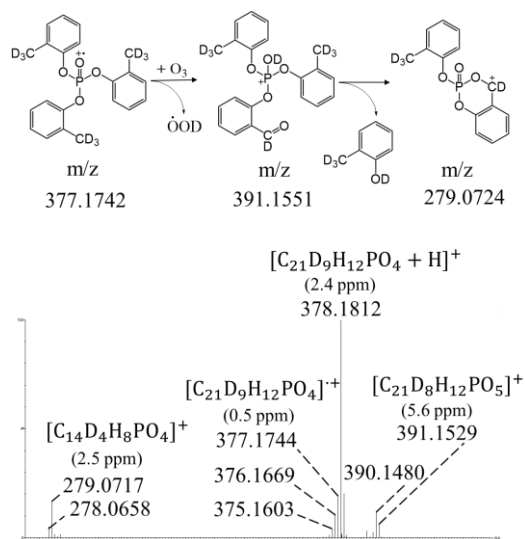


Figure 2.5. The APCI⁺ mass spectrum of D₉-labeled (methyl CD₃) triorthocresyl phosphate (tri-CD₃-o CP).

Compared to its unlabeled analogue, the mass spectrum of CD₃-labelled ToCP also displays two additional peaks that appear at one and two mass units less than the molecular ion mass (m/z 377 and m/z 376) as well as the [M-D+O]⁺ and [CBDP-D]⁺ product ions masses (m/z 390 and m/z 278) (Figure 2.5). Accurate mass measurements suggest that the additional peaks could result from hydrogen-deuterium exchange between the ion structures and water molecules present in the ion source. The mechanism for this exchange has not been investigated, but we note that the distonic ion **TCP2** contains a phosphoryl hydrogen (or deuterium in the case of the CD₃-labelled analogue) that could potentially be exchanged. The mass spectra of the synthesized D₇- and D₁₄-labelled TCPs provide support for this proposal by revealing that only TCPs that are labelled on the ortho-substituted cresyl group(s) form H-D exchange products, see Figures S2.9, S2.11, S2.13 and S2.15. When oxygen is excluded from the source, the putative exchange reactions mostly disappear, which suggests that the exchange may involve intermediates generated during the ion-molecule reactions.

Among the remaining eight synthesized D-labelled ortho-substituted tricresyl phosphates, three of them (mono-D₇-ortho-dimeta CP, mono-D₇-para-diortho CP, and di-D₇-ortho-monometa CP) formed all expected [M-H/D+O]⁺ and [CBDP-H/D]⁺ product ions (Table S2.4). For example, di-D₇-ortho-monometa CP is expected to react with ozone to produce [CBDP-D]⁺ ions while losing either a mass-labelled ortho cresol molecule or an unlabeled meta cresol molecule. In this case, both reactions are observed (Fig. S2.14). The mass spectra of four other labelled compounds (mono-D₇-meta-diortho CP, di-D₇-ortho-monopara CP, di-D₇-meta-monoortho CP, and di-D₇-para-monoortho CP) display mass peaks corresponding to [M-H/D+O]⁺ product ions, but only one or none of the expected [CBDP-H/D]⁺ product ions. In all these cases, the cresol expected to be

lost was D₇-labelled, which suggests a kinetic isotope effect impedes the formation of [CBDP-H/D]⁺ ions. Finally, the last synthesized isotopologue, mono-D₇-ortho-dipara CP, did *not* lose *p*-cresol-OD, which is only labelled with one deuterium. We note that *p*-cresol is the least stable cresol isomer by ~2 kcal/mol[42], thus increasing the dissociation threshold. The loss of cresol-OD also requires a deuterium shift that may be impeded by a kinetic isotope effect. The ethyl-substituted ToCP homologue, tri-*o*-ethyl phenylphosphate (ToEP) was studied to test the hypothesis that the reaction involving ToCP will also occur in its homologues that contain at least one ortho-methylene. In the mass spectrum obtained in the presence of oxygen, peaks corresponding to both [M-H+O]⁺ and [M-H+O-ROH]⁺ ions (*m/z* 425 and *m/z* 303) were observed.

2.3.4. Characterization of the [CBDP-H]⁺ product ions using ion mobility

The mechanism proposed in Figure 2.4 indicates that the *m/z* 275 product ions are generated as a mixture of hydrogen atom shift (H-shift) isomers, viz. **TCP9**, **TCP10** and **TCP11**. Theory predicts that the least stable isomer, **TCP9**, swiftly rearranges via a low barrier into ions **TCP10** and **TCP11**. Therefore, it is expected that the population of *m/z* 275 ions primarily consists of two isomers, **TCP10** and **TCP11**, which may be separable by ion mobility. This hypothesis was tested by the ion mobility experiments shown in Figure 2.6, which display retention time vs. drift time contour plots of the *m/z* 275 ions generated by ToCP. When the *m/z* 275 ions generated in the ion source are subjected to one pass through the cyclic ion mobility cell, three mobility separated peaks are resolved (Fig. 2.6a), of which two will be shown to be genuine *m/z* 275 isomers, while one is an artefact.

Three peaks are observed in the contour plot of Figure 2.6a with drift times of ~23, 24.5 and 29 ms. We propose that the peak observed at a drift time of 29 ms is the result of metastable

dissociation of m/z 383 ions into m/z 275 ions after exiting the cIMS cell. Indeed, when the collision energy is increased in the transfer region located downstream of the cIMS cell, the abundance of the m/z 275 peak observed with a drift time of 29 ms dramatically increases (Fig. 2.7c) whereas the abundances of the two peaks at 23 and 24.5 ms increase when collision-induced dissociation occurs prior to the cIMS cell (Fig. 2.7b). The collision cross section of the ions observed with a drift time of 23 ms was measured to be 149.6 \AA^2 , which deviates by -4.1% from the value computed for **TCP10** using MobCal-MPI. Theory also predicts that the separation of **TCP10** and **TCP11** requires a resolving power of 45 (defined as $R=CCS/\Delta CCS$), which is line with the expected performance of the instrument when ions are subjected to a single pass through the cIMS cell.

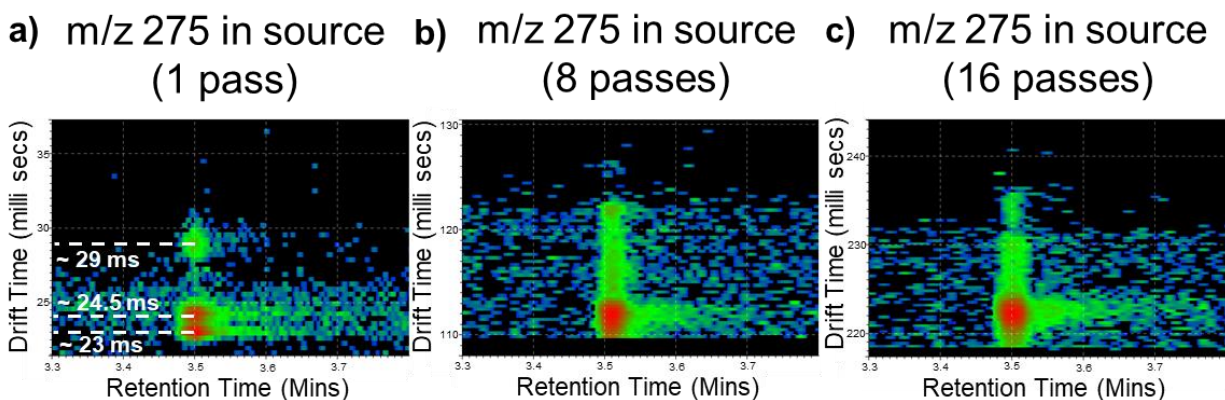


Figure 2.6. Selected ion contour plots of m/z 275 ions that have travelled (a) 1 pass; (b) 8 passes; and (c) 16 passes through the cIMS cell. The two peaks at ~ 23 ms and ~ 24.5 ms correspond to genuine m/z 275 isomers separated by ion mobility. The peak at ~ 29 ms is an artefact peak resulting from metastable decomposition of m/z 383 ions occurring downstream of the cIMS cell. The BGR color scale was used to display intensity.

In principle, the separation of ions **TCP10** and **TCP11** could be improved by allowing the ions to travel successive passes through the cIMS cell. However, when the number of passes is increased to eight (Fig. 2.6b) and sixteen (Fig. 2.6c), the separation does not improve, and the two

peaks instead coalesce. This experimental observation is in agreement with theory, which predicts that ions **TCP10** and **TCP11** are connected by a low-lying transition state (45 kcal/mol below the initial energy of the molecular ion, see Fig. 2.4). When multi-pass experiments are performed, each additional pass provides ions **TCP10** and **TCP11** with more time to interconvert during their transit through the cIMS cell. We also considered the possibility that ions **TCP10** and **TCP11** rearrange by ring-expansion into ions **TCP12** and **TCP13**, whose structures are shown in Figure S2.31. Ions **TCP12** and **TCP13** are the products of benzylium-tropylium rearrangement. However, the energy barriers of these rearrangements are estimated to be as high as 50 kcal/mol based on the previous study by Zins *et al.* [43].

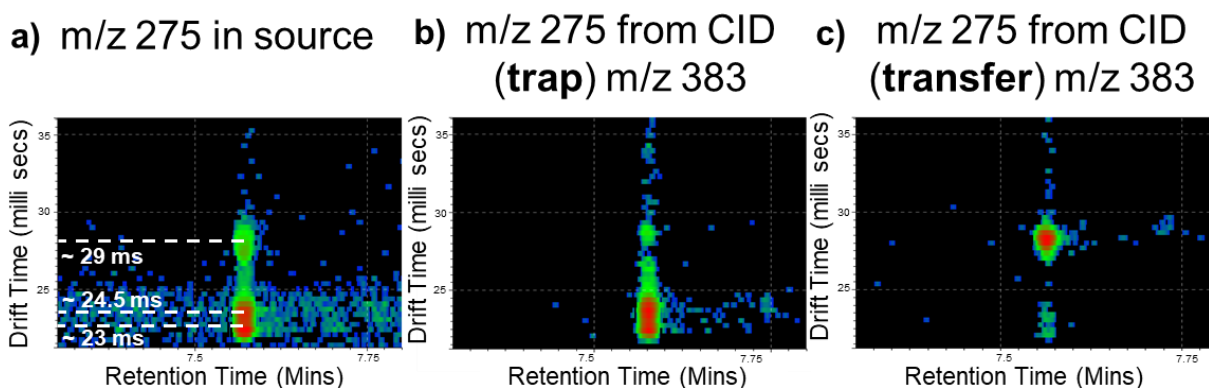


Figure 2.7. Selected ion contour plots of m/z 275 ions (a) generated in the source; and generated from mass selected m/z 383 ions that undergo CID in trap (b) and transfer (c) collision cells.

2.4. Conclusions

The neurotoxic congeners of TCP undergo a two-step metabolism, involving oxidation into M+O followed by decomposition into the metabolite CDBP. This biochemical process parallels the proposed mechanism for the ion-molecule reactions between ionized ToCP with oxygen species present in the APCI source. Computational analysis of the ion-molecule reactions indicates that the reaction between ionized ToCP and O_3 is less energy demanding than the reaction involving

O₂. Experimental support for the selectivity of the reaction toward the ortho-cresyl group(s) was provided by performing mass spectrometry analysis on deuterium labelled ortho-substituted TCP isomers. The results also suggest that a distonic ion plays a crucial role in the reaction. Experiments with the ethyl-substituted ToCP homologue indicated that the ion-molecule reactions occur on ortho-substituted ethyl group(s) as well as methyl group(s). Ion-mobility separation of the products of the ion-molecule reactions revealed the formation of at least two m/z 275 isomers of [CBDP-H]⁺. The present study provides new insight into a structure-diagnostic ion-molecule reactions that may eventually be used to identify potentially toxic congeners of homologous tri-aryl phosphates present in complex mixtures produced in large volume by industry.

References

- [1] D.J. Duarte, J.M.M. Rutten, M. van den Berg, R.H.S. Westerink, In vitro neurotoxic hazard characterization of different tricresyl phosphate (TCP) isomers and mixtures, *Neurotoxicology*. 59 (2017) 222–230. <https://doi.org/10.1016/j.neuro.2016.02.001>.
- [2] G.L. Wei, D.Q. Li, M.N. Zhuo, Y.S. Liao, Z.Y. Xie, T.L. Guo, J.J. Li, S.Y. Zhang, Z.Q. Liang, Organophosphorus flame retardants and plasticizers: Sources, occurrence, toxicity and human exposure, *Environ. Pollut.* 196 (2015) 29–46. <https://doi.org/10.1016/j.envpol.2014.09.012>.
- [3] Y. Yang, Y. Xiao, Y. Chang, Y. Cui, G. Klobučar, M. Li, Intestinal damage, neurotoxicity and biochemical responses caused by tris (2-chloroethyl) phosphate and tricresyl phosphate on earthworm, *Ecotoxicol. Environ. Saf.* 158 (2018) 78–86. <https://doi.org/10.1016/j.ecoenv.2018.04.012>.
- [4] U.E. Bollmann, A. Möller, Z. Xie, R. Ebinghaus, J.W. Einax, Occurrence and fate of organophosphorus flame retardants and plasticizers in coastal and marine surface waters, *Water Res.* 46 (2012) 531–538. <https://doi.org/10.1016/j.watres.2011.11.028>.
- [5] I. van der Veen, J. de Boer, Phosphorus flame retardants: Properties, production, environmental occurrence, toxicity and analysis, *Chemosphere*. 88 (2012) 1119–1153. <https://doi.org/10.1016/j.chemosphere.2012.03.067>.
- [6] C.T. He, J. Zheng, L. Qiao, S.J. Chen, J.Z. Yang, J.G. Yuan, Z.Y. Yang, B.X. Mai, Occurrence of organophosphorus flame retardants in indoor dust in multiple microenvironments of southern China and implications for human exposure, *Chemosphere*. 133 (2015) 47–52. <https://doi.org/10.1016/j.chemosphere.2015.03.043>.

- [7] P.H. Craig, M.L. Barth, Evaluation of the hazards of industrial exposure to tricresyl phosphate: a review and interpretation of the literature, *J. Toxicol. Environ. Heal. - Part B Crit. Rev.* 2 (1999) 281–300. <https://doi.org/10.1080/109374099281142>.
- [8] D.X. Long, Y.J. Wu, Growth inhibition and induction of G1 phase cell cycle arrest in neuroblastoma SH-SY5Y cell by tri-ortho-cresyl phosphate, *Toxicol. Lett.* 181 (2008) 47–52. <https://doi.org/10.1016/j.toxlet.2008.06.871>.
- [9] Y. Li, F. Piao, X. Liu, Protective effect of taurine on triorthocresyl phosphate (TOCP)-induced cytotoxicity in C6 glioma cells. In *Taurine 8*, Springer US, 2013.
- [10] N. INOUE, K. FUJISHIRO, K. MORI, M. MATSUOKA, Triorthocresyl Phosphate Poisoning, *J. UOEH.* 10 (1988) 433–442. <https://doi.org/10.7888/juoeh.10.433>.
- [11] L.M. Schopfer, P. Masson, P. Lamourette, S. Simon, O. Lockridge, Detection of cresyl phosphate-modified butyrylcholinesterase in human plasma for chemical exposure associated with aerotoxic syndrome, *Anal. Biochem.* 461 (2014) 17–26. <https://doi.org/10.1016/j.ab.2014.05.021>.
- [12] M. Liyasova, B. Li, L.M. Schopfer, F. Nachon, P. Masson, C.E. Furlong, O. Lockridge, Exposure to tri-o-cresyl phosphate detected in jet airplane passengers, *Toxicol. Appl. Pharmacol.* 256 (2011) 337–347. <https://doi.org/10.1016/j.taap.2011.06.016>.
- [13] H. de Ree, M. van den Berg, T. Brand, G.J. Mulder, R. Simons, B. Veldhuijzen van Zanten, R.H.S. Westerink, Health risk assessment of exposure to TriCresyl Phosphates (TCPs) in aircraft: A commentary, *Neurotoxicology.* 45 (2014) 209–215. <https://doi.org/10.1016/j.neuro.2014.08.011>.

[14] J.J. Ramsden, On the proportion of ortho isomers in the tricresyl phosphates contained in jet oil, *J. Biol. Phys. Chem.* 13 (2013) 69–72. <https://doi.org/10.4024/03ra13l.jbpc.13.02>.

[15] J.E. Casida, M. Eto, R.L. Baron, Biological Activity of a Tri-o-Cresyl Phosphate Metabolite, *Nature*. 191 (1961).

[16] J. Reinen, L. Nematollahi, A. Fidder, N.P.E. Vermeulen, D. Noort, J.N.M. Commandeur, Characterization of human cytochrome P450s involved in the bioactivation of tri-Ortho-Cresyl phosphate (ToCP), *Chem. Res. Toxicol.* 28 (2015) 711–721. <https://doi.org/10.1021/tx500490v>.

[17] E. Carletti, J.P. Colletier, L.M. Schopfer, G. Santoni, P. Masson, O. Lockridge, F. Nachon, M. Weik, Inhibition pathways of the potent organophosphate CBDP with cholinesterases revealed by X-ray crystallographic snapshots and mass spectrometry, *Chem. Res. Toxicol.* 26 (2013) 280–289. <https://doi.org/10.1021/tx3004505>.

[18] P. Masson, Evolution of and perspectives on therapeutic approaches to nerve agent poisoning, *Toxicol. Lett.* 206 (2011) 5–13. <https://doi.org/10.1016/j.toxlet.2011.04.006>.

[19] Dietrich Henschler, Die Trikresylphosphatvergiftung - Experimentelle Klärung von Problemen der Ätiologie und Pathogenese, *Klin. Wochenschr.* 36 (1958) 663–674.

[20] F. Yang, J. Ding, W. Huang, W. Xie, W. Liu, Particle size-specific distributions and preliminary exposure assessments of organophosphate flame retardants in office air particulate matter, *Environ. Sci. Technol.* 48 (2014) 63–70. <https://doi.org/10.1021/es403186z>.

[21] B. Lazarov, R. Swinnen, M. Spruyt, F. Maes, K. Van Campenhout, E. Goelen, A.

Covaci, M. Stranger, Air sampling of flame retardants based on the use of mixed-bed sorption tubes—a validation study, *Environ. Sci. Pollut. Res.* 22 (2015) 18221–18229. <https://doi.org/10.1007/s11356-015-5028-z>.

[22] T. Suparanon, W. Phetwarotai, Fire-extinguishing characteristics and flame retardant mechanism of polylactide foams: Influence of tricresyl phosphate combined with natural flame retardant, *Int. J. Biol. Macromol.* 158 (2020) 1090–1101. <https://doi.org/10.1016/j.ijbiomac.2020.04.131>.

[23] M.S.E. Makinen, M.R.A. Makinen, J.T.B. Koistinen, A.L. Pasanen, P.O. Pasanen, P.J. Kalliokoski, A.M. Korpi, Respiratory and dermal exposure to organophosphorus flame retardants and tetrabromobisphenol A at five work environments, *Environ. Sci. Technol.* 43 (2009) 941–947. <https://doi.org/10.1021/es802593t>.

[24] G. De Nola, J. Kibby, W. Mazurek, Determination of ortho-cresyl phosphate isomers of tricresyl phosphate used in aircraft turbine engine oils by gas chromatography and mass spectrometry, *J. Chromatogr. A.* 1200 (2008) 211–216. <https://doi.org/10.1016/j.chroma.2008.05.035>.

[25] M. Vykoukalová, M. Venier, Š. Vojta, L. Melymuk, J. Bečanová, K. Romanak, R. Prokeš, J.O. Okeme, A. Saini, M.L. Diamond, J. Klánová, Organophosphate esters flame retardants in the indoor environment, *Environ. Int.* 106 (2017) 97–104. <https://doi.org/10.1016/j.envint.2017.05.020>.

[26] D. Megson, X. Ortiz, K.J. Jobst, E.J. Reiner, M.F.A. Mulder, J. Balouet, Chemosphere A comparison of fresh and used aircraft oil for the identification of toxic substances linked to aerotoxic syndrome, *Chemosphere.* 158 (2016) 116–123.

<https://doi.org/10.1016/j.chemosphere.2016.05.062>.

[27] F. Lépine, D. Boismenu, S. Milot, O.A. Mamer, Collision of molecular anions of benzenedicarboxylic esters with oxygen in a triple quadrupole mass spectrometer, *J. Am. Soc. Mass Spectrom.* 10 (1999) 1248–1252. [https://doi.org/10.1016/S1044-0305\(99\)00105-1](https://doi.org/10.1016/S1044-0305(99)00105-1).

[28] O.A. Mamer, L. Choiniere, D. Boismenu, F. Lepine, Artefactual pyruvate and 2-oxobutyrate produced by trimethylsilylation of methylmalonic and ethylmalonic acids in the presence of oxygen, *J. Inherit. Metab. Dis.* 22 (1999) 821–826. <https://doi.org/10.1023/A:1005510224963>.

[29] K.J. Jobst, J. De Winter, R. Flammang, J.K. Terlouw, P. Gerbaux, Differentiation of the pyridine radical cation from its distonic isomers by ion-molecule reactions with dioxygen, *Int. J. Mass Spectrom.* 286 (2009) 83–88. <https://doi.org/10.1016/j.ijms.2009.06.012>.

[30] S. Fernando, M.K. Green, K. Organtini, F. Dorman, R. Jones, E.J. Reiner, K.J. Jobst, Differentiation of (Mixed) Halogenated Dibenzo-p-Dioxins by Negative Ion Atmospheric Pressure Chemical Ionization, *Anal. Chem.* 88 (2016) 5205–5211. <https://doi.org/10.1021/acs.analchem.6b00255>.

[31] X. Huang, X. Zhao, M. Zhang, Y. Xu, H. Zhi, J. Yang, Green Synthesis of Triaryl Phosphates with POCl₃ in Water, *ChemistrySelect.* 2 (2017) 11007–11011. <https://doi.org/10.1002/slct.201702215>.

[32] R.A. Di Lorenzo, V. V. Lobodin, J. Cochran, T. Kolic, S. Besevic, J.G. Sled, E.J. Reiner, K.J. Jobst, Fast gas chromatography-atmospheric pressure (photo)ionization mass spectrometry of polybrominated diphenylether flame retardants, *Anal. Chim. Acta.* 1056 (2019) 70–78. <https://doi.org/10.1016/j.aca.2019.01.007>.

[33] W.C. Gaussian 16, Revision C.01, Frisch, M. J.; Trucks, G. W.; Schlegel, H. B.; Scuseria, G. E.; Robb, M. A.; Cheeseman, J. R.; Scalmani, G.; Barone, V.; Petersson, G. A.; Nakatsuji, H.; Li, X.; Caricato, M.; Marenich, A. V.; Bloino, J.; Janesko, B. G.; Gompers, Gaussian 16, Revision C.01, (2016). <https://gaussian.com/citation/>.

[34] C. Ieritano, J. Crouse, J.L. Campbell, W.S. Hopkins, A parallelized molecular collision cross section package with optimized accuracy and efficiency, *Analyst*. 144 (2019) 1660–1670. <https://doi.org/10.1039/c8an02150c>.

[35] N.M. O’Boyle, M. Banck, C.A. James, C. Morley, T. Vandermeersch, G.R. Hutchison, *Open Babel*, *J. Cheminform.* 3 (2011) 1–14. <https://jcheminf.biomedcentral.com/track/pdf/10.1186/1758-2946-3-33>.

[36] P. Tosco, T. Balle, F. Shiri, SDF2XYZ2SDF: How to exploit TINKER power in cheminformatics projects, *J. Mol. Model.* 17 (2011) 3021–3023. <https://doi.org/10.1007/s00894-011-1111-7>.

[37] M. Eto, J.E. Casida, T. Eto, Hydroxylation and cyclization reactions involved in the metabolism of tri-O-cresyl phosphate, *Biochem. Pharmacol.* 11 (1962) 337–352. [https://doi.org/10.1016/0006-2952\(62\)90056-4](https://doi.org/10.1016/0006-2952(62)90056-4).

[38] S.T. Ayrton, R. Jones, D.S. Douce, M.R. Morris, R.G. Cooks, Uncatalyzed, Regioselective Oxidation of Saturated Hydrocarbons in an Ambient Corona Discharge, *Angew. Chemie - Int. Ed.* 57 (2018) 769–773. <https://doi.org/10.1002/anie.201711190>.

[39] L. Zeller, J. Farrell, P. Vainiotalo, H.I. Kenttämää, Long-Lived Radical Cations of Simple Organophosphates Isomerize Spontaneously to Distonic Structures in the Gas Phase, *J. Am. Chem. Soc.* 114 (1992) 1205–1214. <https://doi.org/10.1021/ja00030a013>.

[40] E.R. Stephens, M. Dumlao, D. Xiao, D. Zhang, W.A. Donald, Benzylammonium Thermometer Ions: Internal Energies of Ions Formed by Low Temperature Plasma and Atmospheric Pressure Chemical Ionization, *J. Am. Soc. Mass Spectrom.* 26 (2015) 2081–2084. <https://doi.org/10.1007/s13361-015-1272-1>.

[41] J.L. Holmes, K.J. Jobst, J.K. Terlouw, Isotopic labelling in mass spectrometry as a tool for studying reaction mechanisms of ion dissociations, *J. Label. Compd. Radiopharm.* 50 (2007) 1115–1123. <https://doi.org/10.1002/jlcr.1386>.

[42] J.D. Cox, The heats of combustion of phenol and the three cresols, *Pure Appl. Chem.* 2 (1961) 125–128. <https://doi.org/10.1351/pac196102010125>.

[43] E.L. Zins, C. Pepe, D. Rondeau, S. Rochut, N. Galland, J.C. Tabet, Theoretical and experimental study of tropylium formation from substituted benzylpyridinium species, *J. Mass Spectrom.* 44 (2009) 12–17. <https://doi.org/10.1002/jms.1461>.

Supporting Information

Contents

Table S2.1. Energies of the TCP isomers and the products of their reaction with O ₂ were obtained using the B3LYP/6-311G (2d, d, p) level of theory. E _{total} is the total calculated energy in Hartree at 298 K and Rel. E is the calculated relative energy in kcal/mol at 298 K	73
Table S2.2. Energies of the TCP isomers and the products of their reaction with O ₃ were obtained using the B3LYP/6-311G (2d, d, p) level of theory. E _{total} is the total calculated energy in Hartree at 298 K and Rel. E is the calculated relative energy in kcal/mol at 298 K	74
Figure S2.1. The optimized geometries of TCP1-TS5a and their transition structures (in reaction with O ₂) obtained from Gaussian g16 calculations (B3LYP/CBSB7)	75
Figure S2.2. The optimized geometries of TS5a-TCP7 ₂ and their transition structures (in reaction with O ₂) obtained from Gaussian g16 calculations (B3LYP/CBSB7)	76
Figure S2.3. The optimized geometries of TS8-TCP11, and their transition structures (in reaction with O ₂) obtained from Gaussian g16 calculations (B3LYP/CBSB7)	77
Figure S2.4. The optimized geometries of TCP3b-TCP5b, (1,4 H) and (1,9 H), (in reaction with O ₃) obtained from Gaussian g16 calculations (B3LYP/CBSB7)	78
Figure S2.5. The geometries of TCP and [CBDP-H] ⁺ isomers for CCS calculations	79
Table S2.3. List of the synthesized D-labeled TCP isomers and congeners structures	80-83

Table S2.4. Labeled and unlabeled tricresyl phosphate isomers and congeners used in the present study. The elemental compositions of their (quasi)molecular ions and the observed product ions are summarized	84
Figure S2.6. The mass spectrum of ToCP using APGC-MS (+) with air	85
Figure S2.7. The mass spectrum of TmCP using APGC-MS (+) with air	86
Figure S2.8. The mass spectrum of TpCP using APGC-MS (+) with air	87
Figure S2.9. The mass spectrum of mono-D ₇ -meta-diortho CP using APGC-MS (+) with air ...	88
Figure S2.10. The mass spectrum of mono-D ₇ -ortho-dimeta CP using APGC-MS (+) with air	89
Figure S2.11. The mass spectrum of mono-D ₇ -para-diortho CP using APGC-MS (+) with air	90
Figure S2.12. The mass spectrum of mono-D ₇ -ortho-dipara CP using APGC-MS (+) with air	91
Figure S2.13. The mass spectrum of di-D ₇ -meta-monoortho CP using APGC-MS (+) with air	92
Figure S2.14. The mass spectrum of di-D ₇ -ortho-monometata CP using APGC-MS (+) with air	93
Figure S2.15. The mass spectrum of di-D ₇ -para-monoortho CP using APGC-MS (+) with air	94

Figure S2.16. The mass spectrum of di-D ₇ -ortho-monopara CP using APGC-MS (+) with air	95
Figure S2.17. The mass spectrum of ToEP using APGC-MS (+) with air	96
Figure S2.18. The mass spectrum of ToCP using APGC-MS (+) with N ₂	97
Figure S2.19. The mass spectrum of TmCP using APGC-MS (+) with N ₂	98
Figure S2.20. The mass spectrum of TpCP using APGC-MS (+) with N ₂	99
Figure S2.21. The mass spectrum of tri-CD ₃ -o CP using APGC-MS (+) with N ₂	100
Figure S2.22. The mass spectrum of mono-D ₇ -meta-diortho CP using APGC-MS (+) with N ₂	101
Figure S2.23. The mass spectrum of mono-D ₇ -ortho-dimeta CP using APGC-MS (+) with N ₂	102
Figure S2.24. The mass spectrum of mono-D ₇ -para-diortho CP using APGC-MS (+) with N ₂	103
Figure S2.25. The mass spectrum of mono-D ₇ -ortho-dipara CP using APGC-MS (+) with N ₂	104
Figure S2.26. The mass spectrum of di-D ₇ -meta-monoortho CP using APGC-MS (+) with N ₂	105
Figure S2.27. The mass spectrum of di-D ₇ -ortho-monometata CP using APGC-MS (+) with N ₂	106

Figure S2.28. The mass spectrum of di-D ₇ -para-monoortho CP using APGC-MS (+) with N ₂	107
Figure S2.29. The mass spectrum of di-D ₇ -ortho-monopara CP using APGC-MS (+) with N ₂	108
Figure S2.30. The mass spectrum of ToEP using APGC-MS (+) with N ₂	109
Figure S2.31. The structures of TCP 12 and TCP 13; the benzyllium-tropylium ion rearrangement products of TCP 10 and TCP 11	110
Table S2.5 The list of all TCP ⁺⁺ and [CBDP-H] ⁺ isomers predicted MobCal_MPI CCS values	110

Table S2.1. Energies of the TCP isomers and the products of their reaction with O₂ were obtained using the B3LYP/6-311G (2d, d, p) level of theory. E_{total} is the total calculated energy in Hartree at 298 K and Rel. E is the calculated relative energy in kcal/mol at 298 K.

Structure	E _{total} [298 K]	Rel. E [298 K]	Transition State	E _{total} [298 K]	Rel. E [298 K]
TpCP	-1455.2684078	-	-	-	-
TpCP + O₂	-1605.5710116	-2	-	-	-
TmCP	-1455.2649829	-	-	-	-
TmCP + O₂	-1605.5675867	0	-	-	-
TCP 1 (ToCP)	-1455.2644453	-	TS1 (TCP1→TCP2)	-1455.2352011	-
O ₂	-150.3647876	-	-	-	-
TCP 1 + O₂	-1605.6292329	0	TS1 (TCP1→TCP2) + O₂	-1605.5999887	18
TCP 2	-1455.2482693	-	-	-	-
TCP 2 + O₂	-1605.6130569	10	-	-	-
TCP 3a	-1605.6428051	-9	TS3a (TCP3a→TCP4a)	-1605.6394173	-6
TCP 4a	-1605.6385111	-14	TS4a (TCP4a→TCP5a)	-1605.6281296	1
TCP 5a	-1605.6432083	-9	TS5a (TCP5a→TBC1)	-1605.5954846	21
TBC1	-1605.6187789	7	TSTBC (TBC1→TCP6 + OH[•])	-1605.5834203	29
TCP 6	-1529.9399433	-	TS6 (TCP6→TCP7 ₁)	-1529.9038719	-
OH [•]	-75.7545265	-	-	-	-
TCP 6 + OH[•]	-1605.6944698	-41	TS6 (TCP6→TCP7₁) + OH[•]	-1605.6583984	-18
TCP 7 ₁	-1529.9145731	-	TS7 (TCP7 ₁ →TCP7 ₂)	-1529.9048957	-
TCP 7₁ + OH[•]	-1605.6690996	-25	TS7 (TCP7₁→TCP7₂) + OH[•]	-1605.6594222	-19
TCP 7 ₂	-1529.9186763	-	TS8 (TCP7 ₂ →TCP7 ₃)	-1529.9048957	-
TCP 7₂ + OH[•]	-1605.6732028	-28	TS8 (TCP7₂→TCP7₃) + OH[•]	-1605.6525146	-15
TCP 7 ₃	-1529.9309521	-	TS9 (TCP7 ₃ →TCP8)	-1529.874462	-
TCP 7₃ + OH[•]	-1605.6854786	-35	TS9 (TCP7₃→TCP8) + OH[•]	-1605.6289881	0
TCP 8	-1529.880533	-	-	-	-
TCP 8 + OH[•]	-1605.6350592	-4	-	-	-
TCP 9	-1182.9421816	-	TS10 (TCP9→TCP10)	-1182.9345215	-
ROH	-346.8794521	-	-	-	-
TCP 9 + ROH	-1529.8216337	-	TS10 (TCP9→TCP10) + ROH	-1529.8139736	-
TCP 9 + OH[•] + ROH	-1605.5761602	33	TS10 (TCP9→TCP10) + OH[•] + ROH	-1605.5685001	38
TCP 10	-1183.0172029	-	TS11 (TCP9→TCP10)	-1182.9775067	-
TCP 10 + OH[•] + ROH	-1605.6511815	-14	TS11 (TCP9→TCP10) + OH[•] + ROH	-1605.6114853	11
TCP 11	-1183.0047928	-	-	-	-
TCP 11 + OH[•] + ROH	-1605.6387714	-6	-	-	-
TCP 11	-1183.0175746	-	-	-	-
TCP 12 + OH[•] + ROH	-1605.6515532	-14	-	-	-
TCP 12	-1183.0175694	-	-	-	-
TCP 13 + OH[•] + ROH	-1605.651548	-14	-	-	-

Table S2.2. Energies of the TCP isomers and the products of their reaction with O₃ were obtained using the B3LYP/6-311G (2d, d, p) level of theory. E_{total} is the total calculated energy in Hartree at 298 K and Rel. E is the calculated relative energy in kcal/mol at 298 K.

Structure	E _{total} [298 K]	Rel. E [298 K]	Transition State	E _{total} [298 K]	Rel. E [298 K]
TpCP	-1455.2684078	–	–	–	–
TpCP + O₃	-1680.7391964	-2	–	–	–
TmCP	-1455.2649829	–	–	–	–
TmCP + O₃	-1680.7357715	0	–	–	–
TCP 1 (ToCP)	-1455.2644453	–	TS1 (TCP1→TCP2)	-1455.2352011	–
O ₃	-225.4707886	–	–	–	–
TCP 1 + O₃	-1680.7352339	0	TS1 (TCP1→TCP2) + O₃	-1680.7059897	18
TCP 2	-1455.2482693	–	–	–	–
TCP 2 + O₃	-1680.7190579	10	–	–	–
TCP 3b	-1680.8472056	-70	TS3b (TCP3b →TCP6+ OOH) [1,4 H]	-1680.8401593	-66
			TS3b (TCP3b →TCP4b) [1,9 H]*	-1680.8061502	-44
TCP 4b	-1680.8027707	-42	TS4b (TCP4b→TCP5b)*	-1680.7790300	-27
TCP 5b	-1680.9019150	-105	TSSb (TCP5b→TCP6 + OOH)*	-1680.9029928	-105
TCP 6	-1529.9399433	–	TS6 (TCP6→TCP7 ₁)	-1529.9038719	–
OOH	-150.9504083	–	–	–	–
TCP 6 + OOH	-1680.8903516	-97	TS6 (TCP6→TCP7₁) + OOH	-1680.8542802	-75
TCP 7 ₁	-1529.9145731	–	TS7 (TCP7 ₁ →TCP7 ₂)	-1529.9048957	–
TCP 7₁ + OOH	-1680.8649814	-81	TS7 (TCP7₁→TCP7₂) + OOH	-1680.8553040	-75
TCP 7 ₂	-1529.9186763	–	TS8 (TCP7 ₂ →TCP7 ₃)	-1529.9048957	–
TCP 7₂ + OOH	-1680.8690846	-84	TS8 (TCP7₂→TCP7₃) + OOH	-1680.8483964	-71
TCP 7 ₃	-1529.9309521	–	TS9 (TCP7 ₃ →TCP8)	-1529.874462	–
TCP 7₃ + OOH	-1680.8813604	-92	TS9 (TCP7₃→TCP8) + OOH	-1680.8248699	-56
TCP 8	-1529.880533	–	–	–	–
TCP 8 + OOH	-1680.830941	-60	–	–	–
TCP 9	-1182.9421816	–	TS10 (TCP9→TCP10)	-1182.9345215	–
ROH	-346.8794521	–	–	–	–
TCP 9 + ROH	-1529.8216337	–	TS10 (TCP9→TCP10) + ROH	-1529.8139736	–
TCP 9 + OOH + ROH	-1680.7720420	-23	TS10 (TCP9→TCP10) + OOH + ROH	-1680.7643819	-18
TCP 10	-1183.0172029	–	TS11 (TCP9→TCP10)	-1182.9775067	–
TCP 10 + OOH + ROH	-1680.8470633	-70	TS11 (TCP9→TCP10) + OOH + ROH	-1680.8073671	-45
TCP 11	-1183.0047928	–	–	–	–
TCP 11 + OOH + ROH	-1680.8346532	-62	–	–	–
TCP 11	-1183.0175746	–	–	–	–
TCP 12 + OOH + ROH	-1605.6515532	-70	–	–	–
TCP 12	-1183.0175694	–	–	–	–
TCP 13 + OOH + ROH	-1605.651548	-70	–	–	–

* The transition structures and intermediates of the 1,9 H-shift path are not shown in the energy diagram shown in Figure 4.

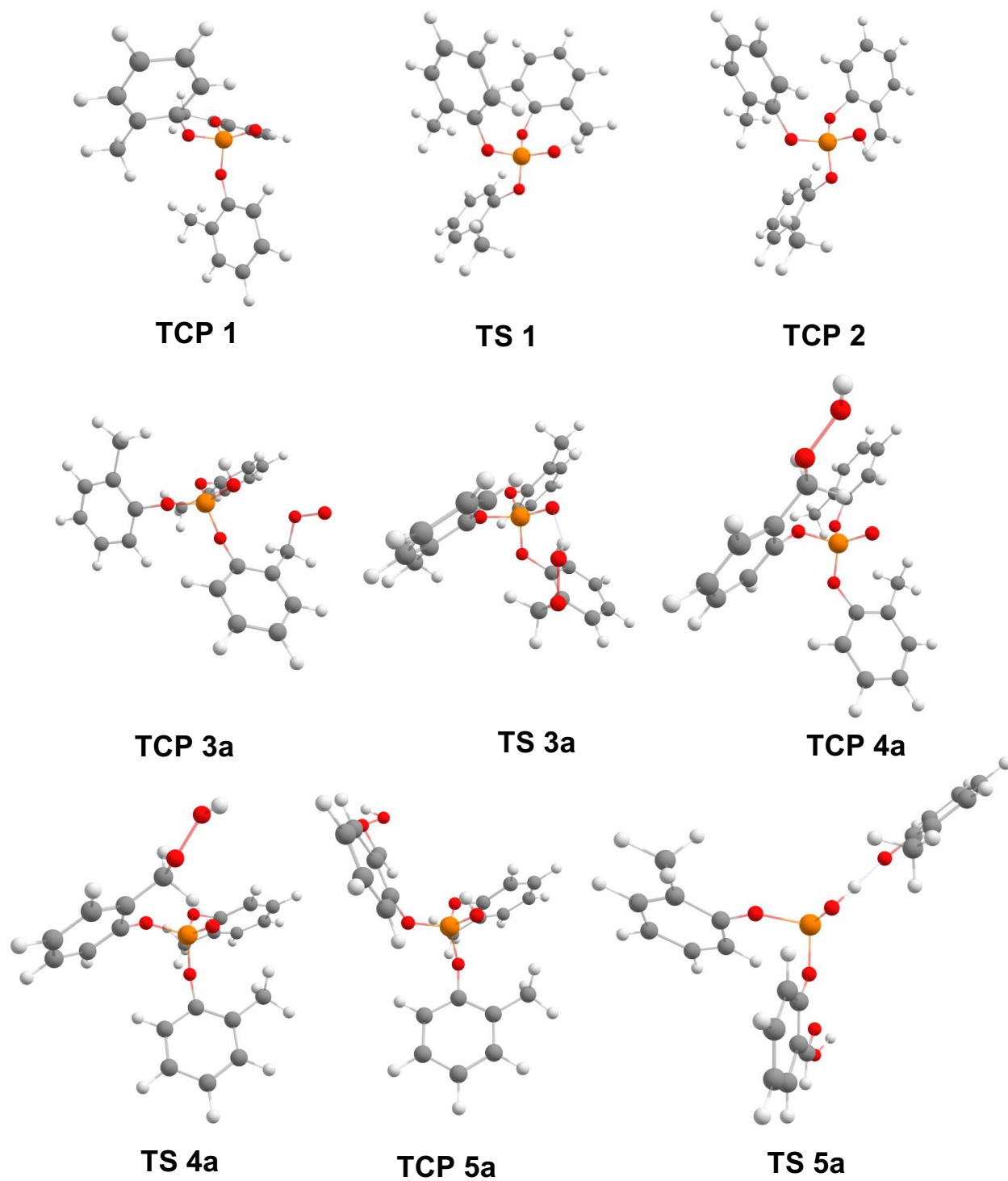


Figure S2.1. The optimized geometries of TCP1-TS5a and their transition structures (in reaction with O₂) obtained from Gaussian g16 calculations (B3LYP/CBSB7)

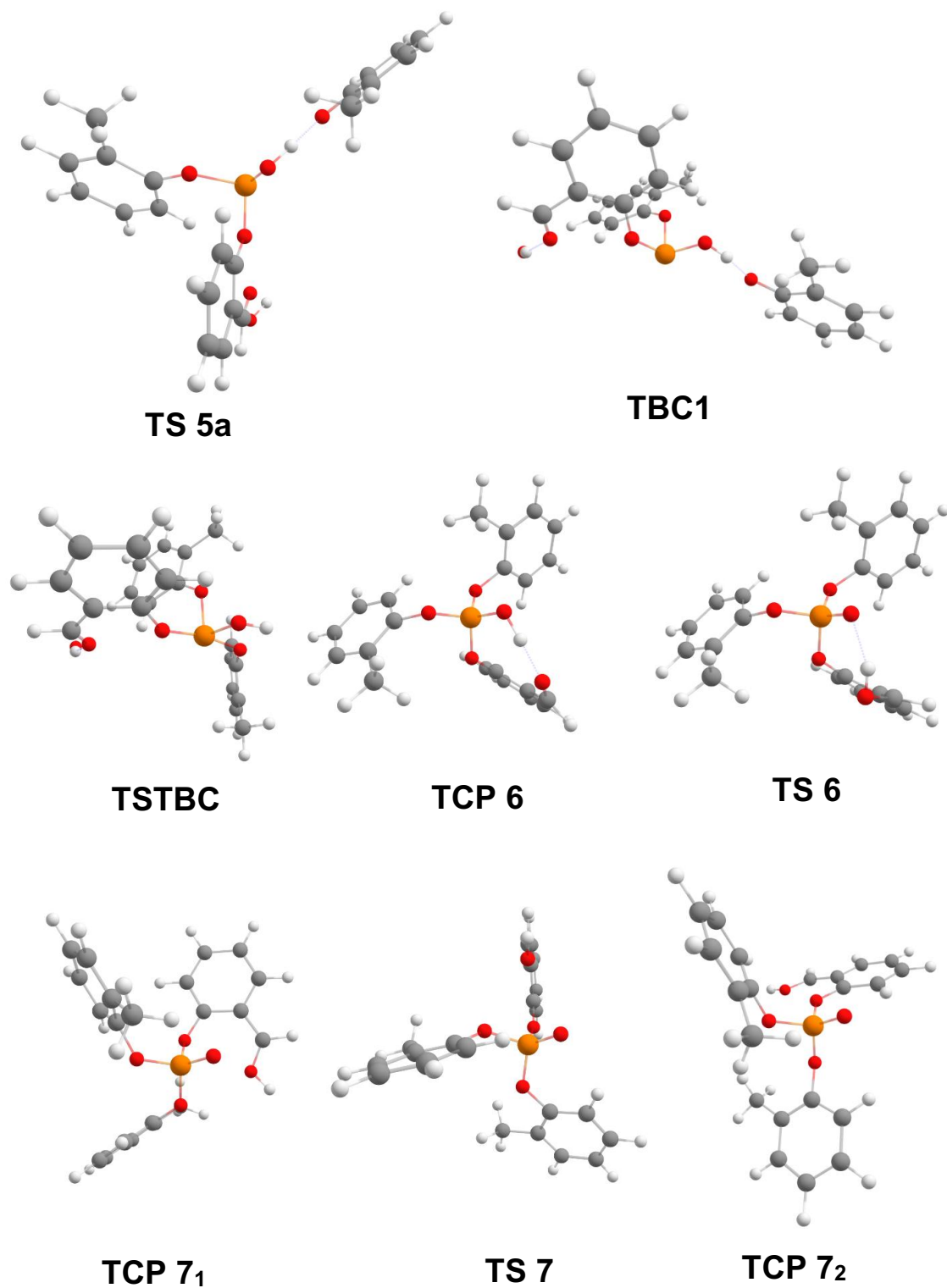


Figure S2.2. The optimized geometries of TS5a-TCP7₂ and their transition structures (in reaction with O_2) obtained from Gaussian g16 calculations (B3LYP/CBSB7)

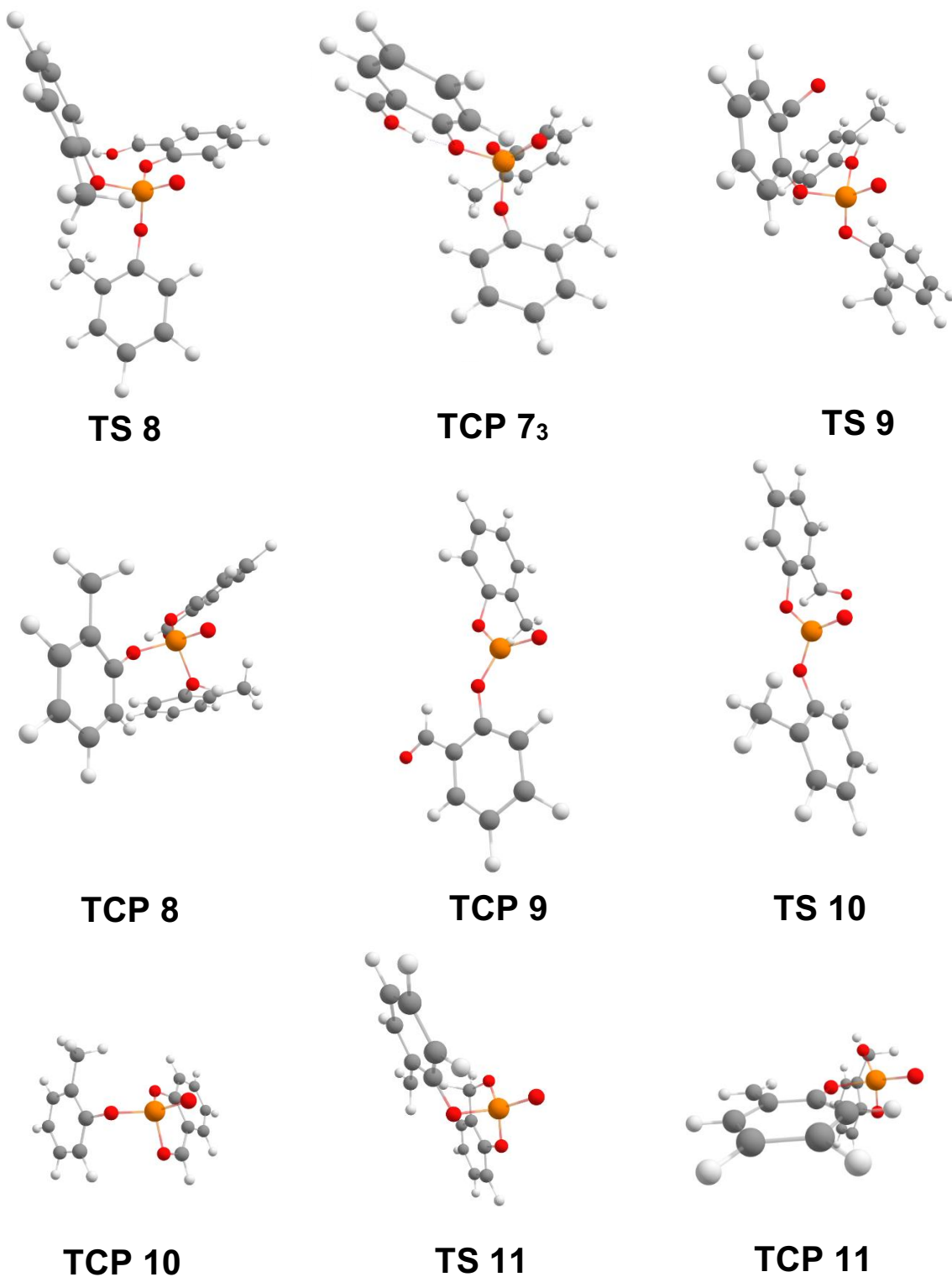
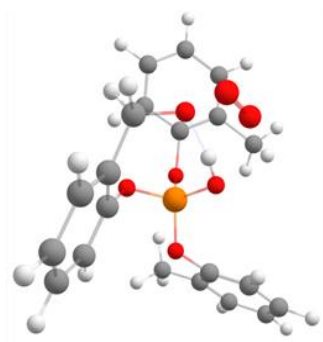
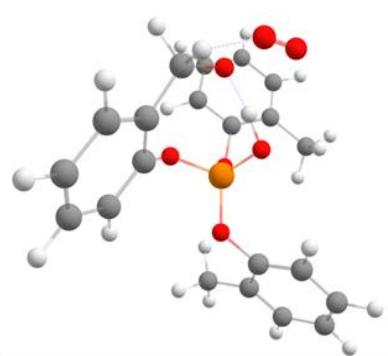


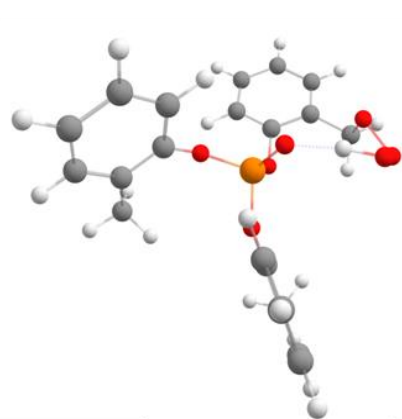
Figure S2.3. The optimized geometries of TS8-TCP11, and their transition structures (in reaction with O₂) obtained from Gaussian g16 calculations (B3LYP/CBSB7)



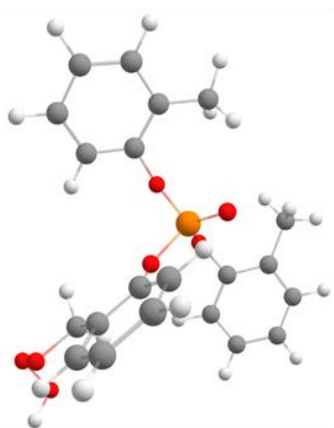
TCP 3b



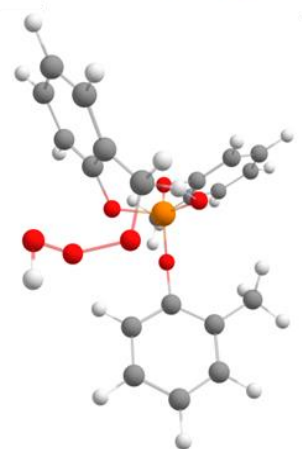
TS 3b (1,4 H)



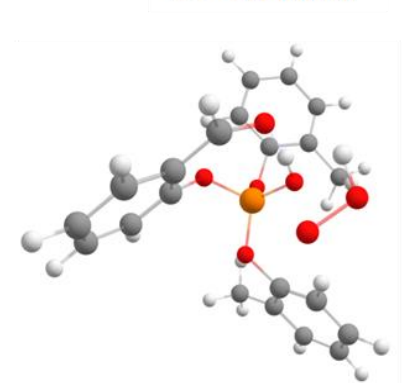
TS 3b (1,9 H)



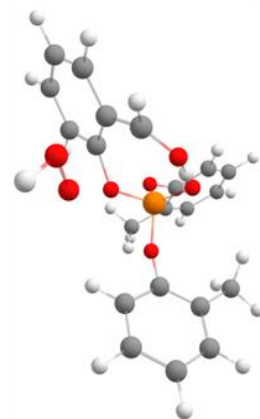
TCP 4b (1,9 H)



TS 4b (1,9 H)



TCP 5b (1,9 H)



TS 5b (1,9 H)

Figure S2.4. The optimized geometries of TCP3b-TCP5b, (1,4 H) and (1,9 H), (in reaction with O₃) obtained from Gaussian g16 calculations (B3LYP/CBSB7)

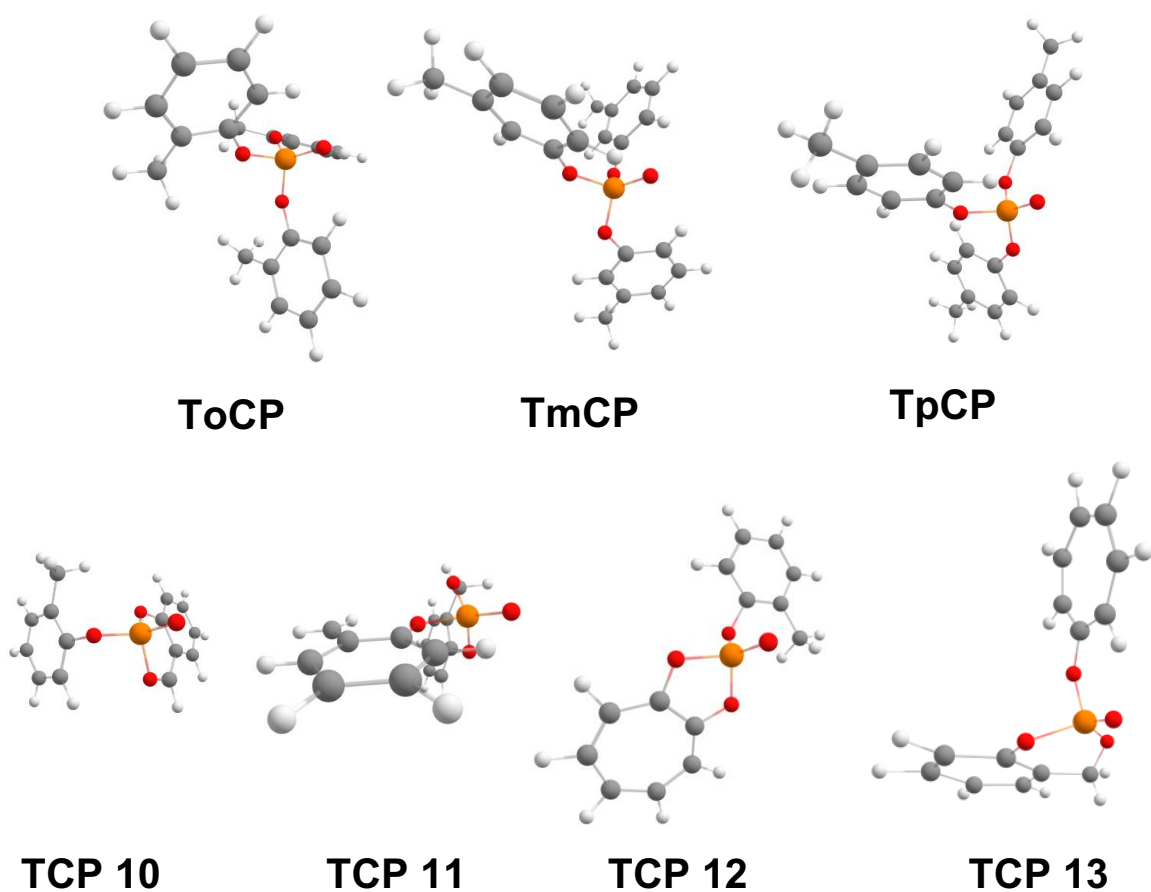
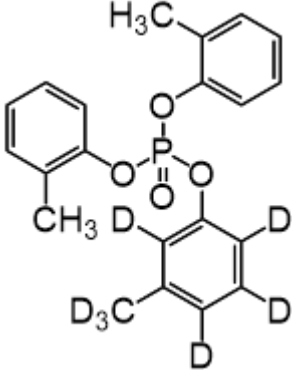
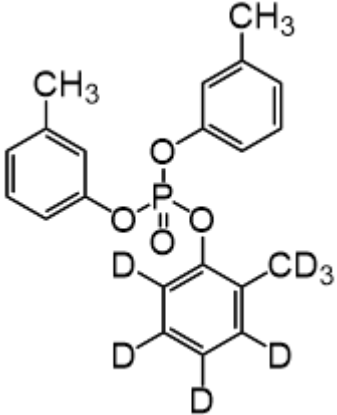
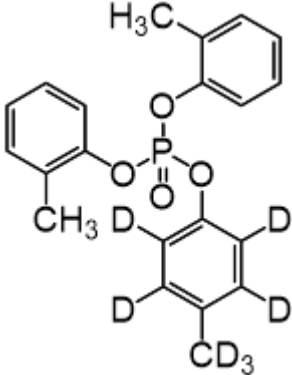
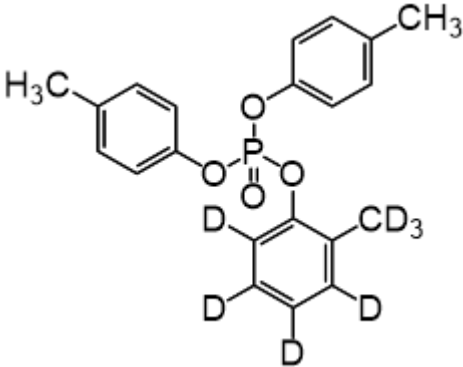
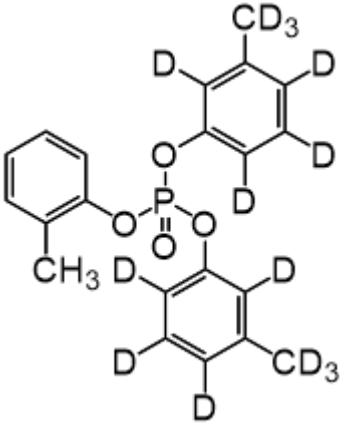
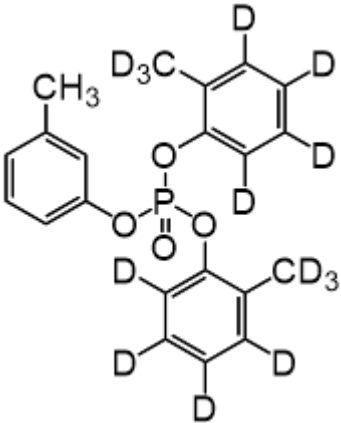
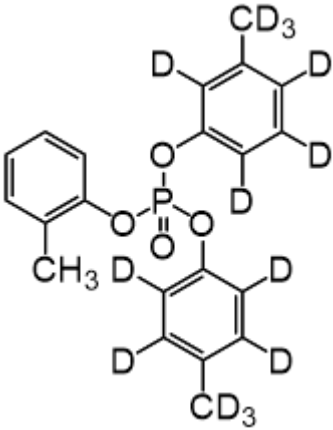
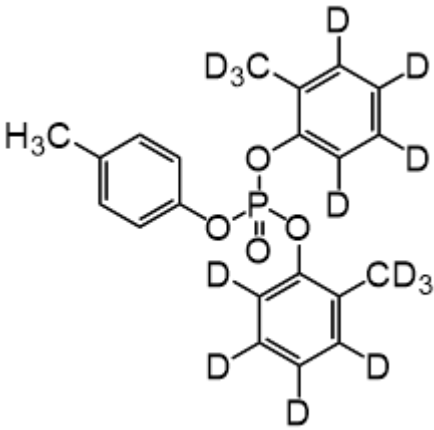
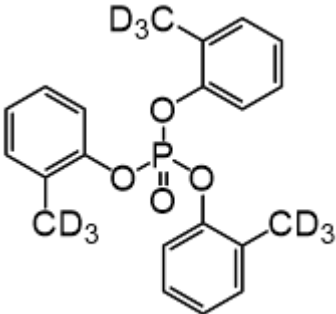


Figure S2.5. The optimized geometries of TCP isomers (ToCP, TmCP, TpCP) molecular ions ($m/z=368$) and all predicted [CBDP-H]⁺ isomers deprotonated ions ($m/z=275$) obtained from gaussian g16 calculations on B3LYP functional in connection with the CBSB7 basis set with the form of 6-311G (2d, d, p).

Table S2.3. List of the synthesized D-labeled TCP isomers and congeners structures.

Name	Structure
<p>mono-D₇-meta-diorthocresyl phosphate (mono-D₇-meta-diortho CP)</p>	
<p>mono-D₇-ortho-dimetacresyl phosphate (mono-D₇-ortho-dimeta CP)</p>	
<p>mono-D₇-paradiorthocresyl phosphate (mono-D₇-para-diortho CP)</p>	

<p>mono-D₇-orthodiparacresyl phosphate (mono-D₇-ortho-dipara CP)</p>	
<p>di-D₇-metamonoorthocresyl phosphate (di-D₇-meta-monoortho CP)</p>	
<p>di-D₇-ortho monometacresyl phosphate (di-D₇-ortho-monometa CP)</p>	

<p>di-D₇-paramonothocresyl phosphate (di-D₇-para-monoortho CP)</p>	
<p>di-D₇-orthomonoparacresyl phosphate (di-D₇-ortho-monopara CP)</p>	
<p>tri-CD₃-orthocresyl phosphate (tri-CD₃-o CP)</p>	

triorthoethyl phenyl phosphate

(ToEP)

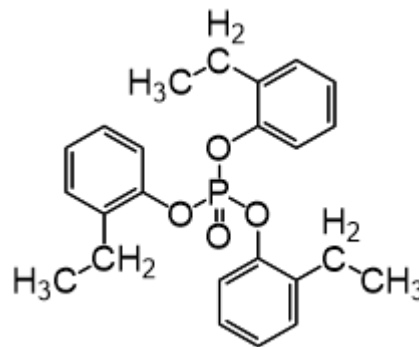


Table S2.4. Labeled and unlabeled tricresyl phosphate isomers and congeners used in the present study. The elemental compositions of their (quasi)molecular ions (2nd and 3rd columns) and the observed product ions (4th and 5th columns) are summarized.

Neutral Structure	M ⁺	[M+H] ⁺	(1) [M-H+O] ⁺ (2) [M-D+O] ⁺	(A) [M-H+O-ROH] ⁺ (B) [M-H+O-R(D ₇)OH] ⁺ (C) [M-D+O-ROD] ⁺ (D) [M-D+O-R(D ₇)OD] ⁺ (E) [M-D+O-R(D ₃)OD] ⁺
ToCP (C ₂₁ H ₂₁ PO ₄); (Figure S2.6)	[C ₂₁ H ₂₁ PO ₄] ⁺ : Not Observed	[C ₂₁ H ₂₂ PO ₄] ⁺ : 369.1248 (2.2 ppm)	(1) [C ₂₁ H ₂₀ PO ₃] ⁺ : 383.1037 (2.9 ppm)	(A) [C ₁₄ H ₁₂ PO ₄] ⁺ : 275.0464 (3.3 ppm)
TmCP (C ₂₁ H ₂₁ PO ₄); (Figure S2.7)	[C ₂₁ H ₂₁ PO ₄] ⁺ : 368.1167 (2.8 ppm)	[C ₂₁ H ₂₂ PO ₄] ⁺ : 369.1245 (3.0 ppm)	-	-
TpCP (C ₂₁ H ₂₁ PO ₄); (Figure S2.8)	[C ₂₁ H ₂₁ PO ₄] ⁺ : 368.1169 (2.2 ppm)	[C ₂₁ H ₂₂ PO ₄] ⁺ : 369.1244 (3.3 ppm)	-	-
mono-D₇-meta-diortho CP (C ₂₁ D ₇ H ₁₄ PO ₄); (Figure S2.9)	[C ₂₁ D ₇ H ₁₄ PO ₄] ⁺ : 375.1614 (0.8 ppm)	[C ₂₁ D ₇ H ₁₅ PO ₄] ⁺ : 376.1690 (1.3 ppm)	(1) [C ₂₁ D ₇ H ₁₃ PO ₃] ⁺ : 390.1482 (1.5 ppm)	(A) [C ₁₄ D ₇ H ₃ PO ₄] ⁺ : 282.0906 (2.1 ppm) (B) [C ₁₄ H ₁₂ PO ₄] ⁺ : Not Observed
mono-D₇-ortho-dimeta CP (C ₂₁ D ₇ H ₁₄ PO ₄); (Figure S2.10)	[C ₂₁ D ₇ H ₁₄ PO ₄] ⁺ : 375.1614 (0.8 ppm)	[C ₂₁ D ₇ H ₁₅ PO ₄] ⁺ : 376.1694 (0.3 ppm)	(2) [C ₂₁ D ₆ H ₁₄ PO ₃] ⁺ : 389.1413 (3.1 ppm)	(C) [C ₁₄ D ₅ H ₇ PO ₄] ⁺ : 280.0783 (1.4 ppm)
mono-D₇-para-diortho CP (C ₂₁ D ₇ H ₁₄ PO ₄); (Figure S2.11)	[C ₂₁ D ₇ H ₁₄ PO ₄] ⁺ : 375.1615 (0.5 ppm)	[C ₂₁ D ₇ H ₁₅ PO ₄] ⁺ : 376.1686 (2.4 ppm)	(1) [C ₂₁ D ₇ H ₁₃ PO ₃] ⁺ : 390.1480 (2.1 ppm)	(A) [C ₁₄ D ₇ H ₃ PO ₄] ⁺ : 282.0899 (4.6 ppm) (B) [C ₁₄ H ₁₂ PO ₄] ⁺ : 275.0468 (1.8 ppm)
mono-D₇-ortho-dipara CP (C ₂₁ D ₇ H ₁₄ PO ₄); (Figure S2.12)	[C ₂₁ D ₇ H ₁₄ PO ₄] ⁺ : 375.1611 (1.6 ppm)	[C ₂₁ D ₇ H ₁₅ PO ₄] ⁺ : 376.1687 (2.1 ppm)	(2) [C ₂₁ D ₆ H ₁₄ PO ₃] ⁺ : 389.1406 (4.9 ppm)	(C) [C ₁₄ D ₅ H ₇ PO ₄] ⁺ : Not Observed
di-D₇-meta-monoortho CP (C ₂₁ D ₁₄ H ₇ PO ₄); (Figure S2.13)	[C ₂₁ D ₁₄ H ₇ PO ₄] ⁺ : 382.2057 (0.3 ppm)	[C ₂₁ D ₁₄ H ₈ PO ₄] ⁺ : 383.2122 (3.1 ppm)	(1) [C ₂₁ D ₁₄ H ₆ PO ₃] ⁺ : 397.1921 (1.5 ppm)	(B) [C ₁₄ D ₇ H ₃ PO ₄] ⁺ : Not Observed
di-D₇-ortho-monometata CP (C ₂₁ D ₁₄ H ₇ PO ₄); (Figure S2.14)	[C ₂₁ D ₁₄ H ₇ PO ₄] ⁺ : 382.2059 (0.8 ppm)	[C ₂₁ D ₁₄ H ₈ PO ₄] ⁺ : 383.2127 (1.8 ppm)	(2) [C ₂₁ D ₁₃ H ₇ PO ₃] ⁺ : 396.1849 (3.8 ppm)	(C) [C ₁₄ D ₁₂ H ₅ PO ₄] ⁺ : 287.1223 (1.4 ppm) (D) [C ₁₄ D ₅ H ₇ PO ₄] ⁺ : 280.0777 (3.6 ppm)
di-D₇-para-monoortho CP (C ₂₁ D ₁₄ H ₇ PO ₄); (Figure S2.15)	[C ₂₁ D ₁₄ H ₇ PO ₄] ⁺ : 382.2056 (0.0 ppm)	[C ₂₁ D ₁₄ H ₈ PO ₄] ⁺ : 383.2126 (2.1 ppm)	(1) [C ₂₁ D ₁₄ H ₆ PO ₃] ⁺ : 397.1918 (2.3 ppm)	(B) [C ₁₄ D ₇ H ₃ PO ₄] ⁺ : Not Observed
di-D₇-ortho-monopara CP (C ₂₁ D ₁₄ H ₇ PO ₄); (Figure S2.16)	[C ₂₁ D ₁₄ H ₇ PO ₄] ⁺ : 382.2055 (0.3 ppm)	[C ₂₁ D ₁₄ H ₈ PO ₄] ⁺ : 383.2125 (2.3 ppm)	(2) [C ₂₁ D ₁₃ H ₇ PO ₃] ⁺ : 396.1838 (6.6 ppm)	(C) [C ₁₄ D ₁₂ H ₅ PO ₄] ⁺ : 287.1218 (3.1 ppm) (D) [C ₁₄ D ₅ H ₇ PO ₄] ⁺ : Not Observed
tri-CD₃-o CP (C ₂₁ D ₉ H ₁₂ PO ₄); (Figure 2.5)	[C ₂₁ D ₉ H ₁₂ PO ₄] ⁺ : 377.1744 (0.5 ppm)	[C ₂₁ D ₉ H ₁₃ PO ₄] ⁺ : 378.1812 (2.4 ppm)	(2) [C ₂₁ D ₈ H ₁₂ PO ₃] ⁺ : 391.1529 (5.6 ppm)	(E) [C ₁₄ D ₄ H ₈ PO ₄] ⁺ : 279.0717 (2.5 ppm)
ToEP (C ₂₄ H ₂₇ PO ₄); (Figure S2.17)	[C ₂₄ H ₂₇ PO ₄] ⁺ : 410.1597 (12.2 ppm)	[C ₂₄ H ₂₈ PO ₄] ⁺ : 411.1725 (0.0 ppm)	(1) [C ₂₄ H ₂₆ PO ₃] ⁺ : 425.1511 (1.6 ppm)	(A) [C ₁₆ H ₁₆ PO ₄] ⁺ : 303.0778 (2.6 ppm)

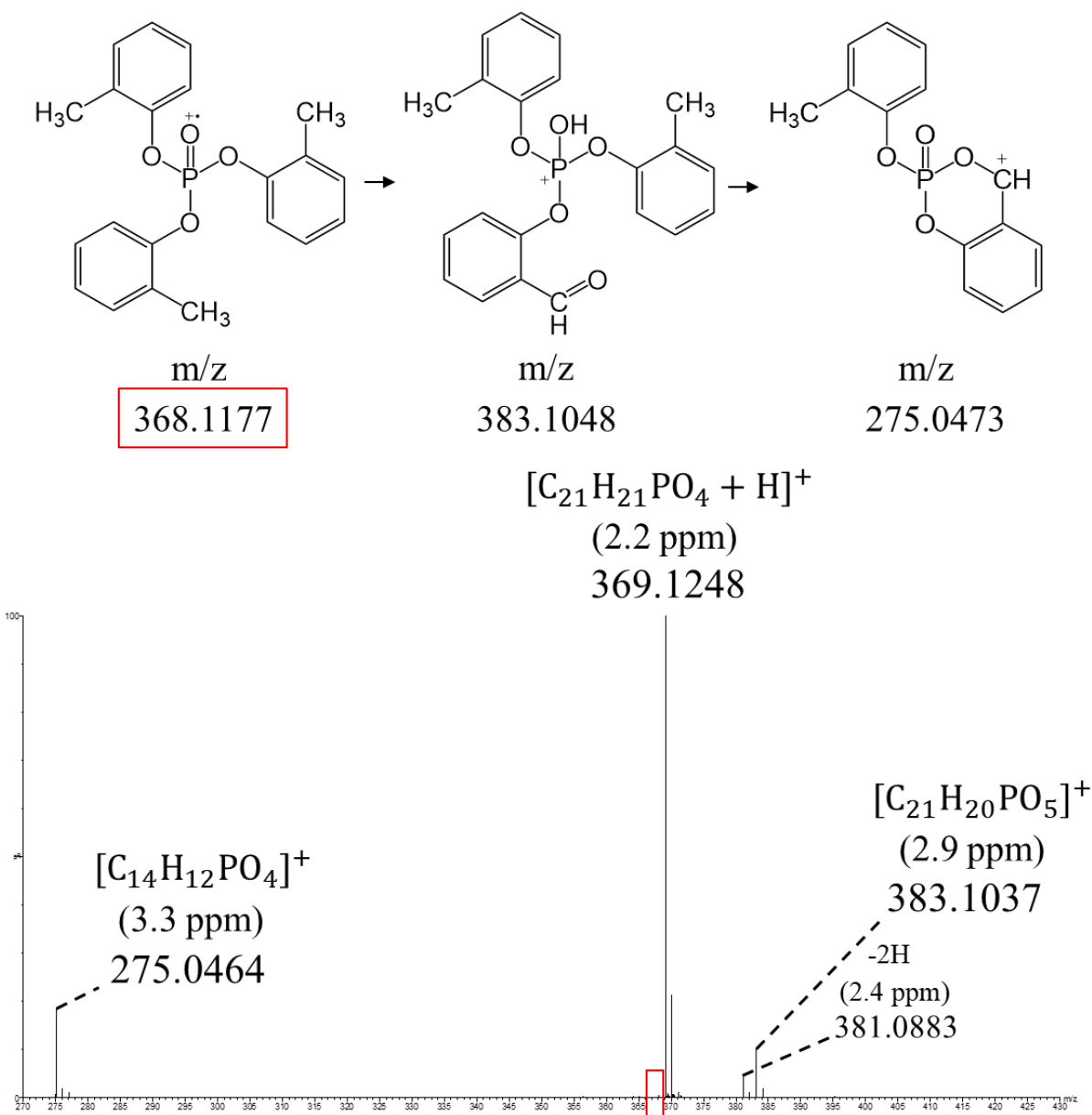
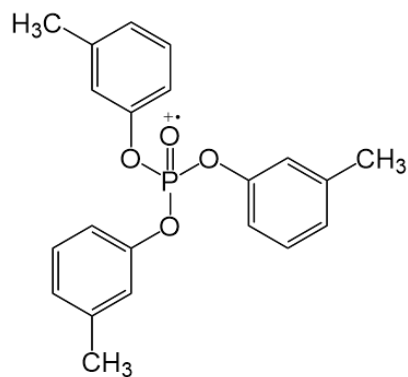


Figure S2.6. The mass spectrum of the standard triorthocresyl phosphate (ToCP) obtained from the APGC-MS(TOF) with compressed air in positive mode. The mass peak of ToCP molecular ion (m/z=368) was not observed. The mass peaks of m/z=383 and m/z=275 represent the [ToCP+O-H]⁺ and [ToCP+O-H-ROH]⁺ (or [CBDP-H]⁺) ion products, respectively. The ion product with m/z=383 produces the m/z=381 by a loss of H₂ molecule.



m/z
368.1177

$[C_{21}H_{21}PO_4 + H]^+$
(3.0 ppm)
369.1245

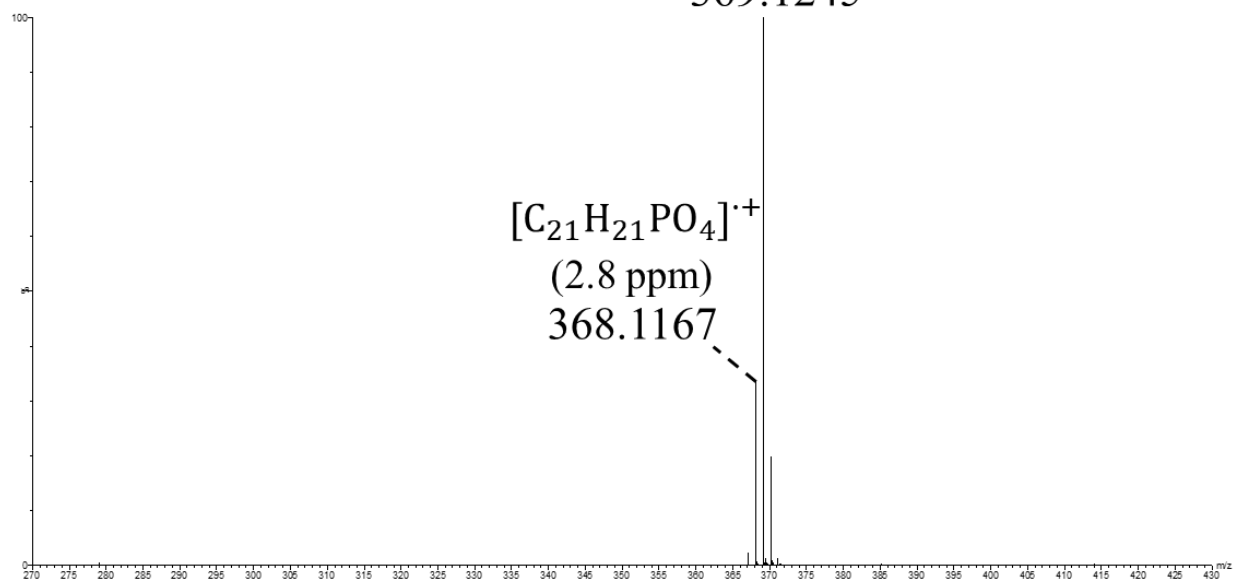
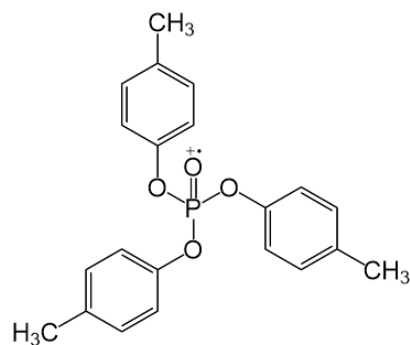


Figure S2.7. The mass spectrum of the standard trimetacresyl phosphate (TmCP) obtained from the APGC-MS(TOF) with compressed air in positive mode. The mass peak of the TmCP molecular ion ($m/z=368$) and the protonated ion ($[TmCP+H]^+$) were observed. No other mass peaks corresponding to any reaction products were observed in the spectrum, showing that $TmCP^+$ does not undergo the same reaction as $ToCP^+$.



m/z
368.1177

$[C_{21}H_{21}PO_4 + H]^+$
(3.3 ppm)
369.1244

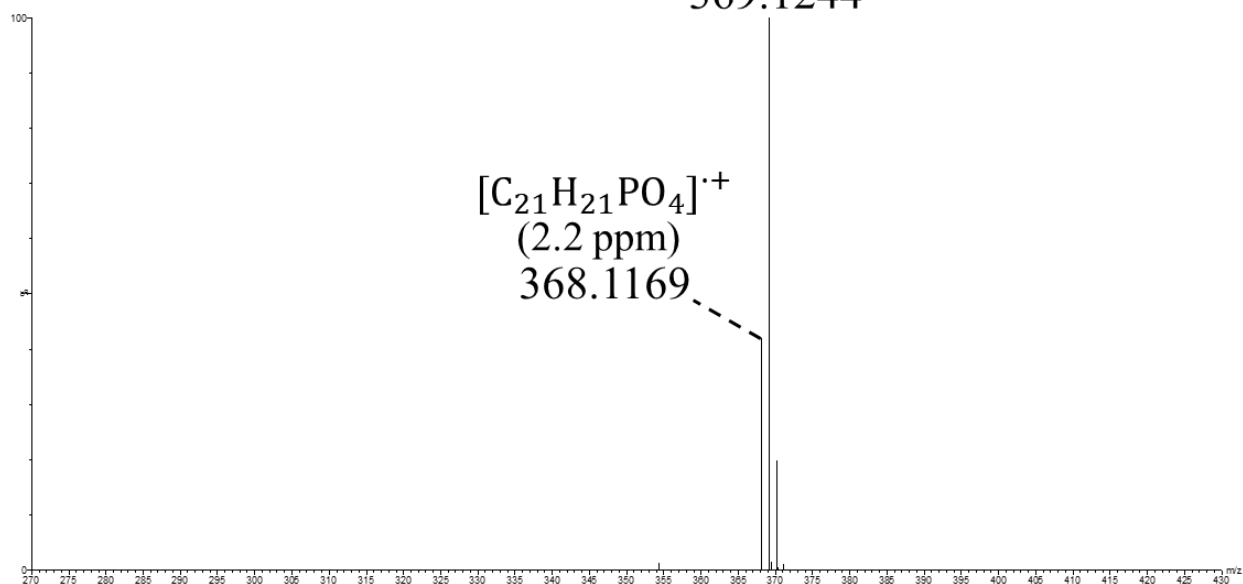


Figure S2.8. The mass spectrum of the standard triparacresyl phosphate (TpCP) obtained from the APGC-MS(TOF) with compressed air in positive mode. Similar to TmCP⁺, The mass peak of TpCP molecular ion (m/z=368) and [TmCP+H]⁺ were observed. No extra mass peaks corresponding to any reaction products were not observed in the spectrum, showing that TpCP⁺, same as TmCP⁺, does not undergo the same reaction as ToCP⁺.

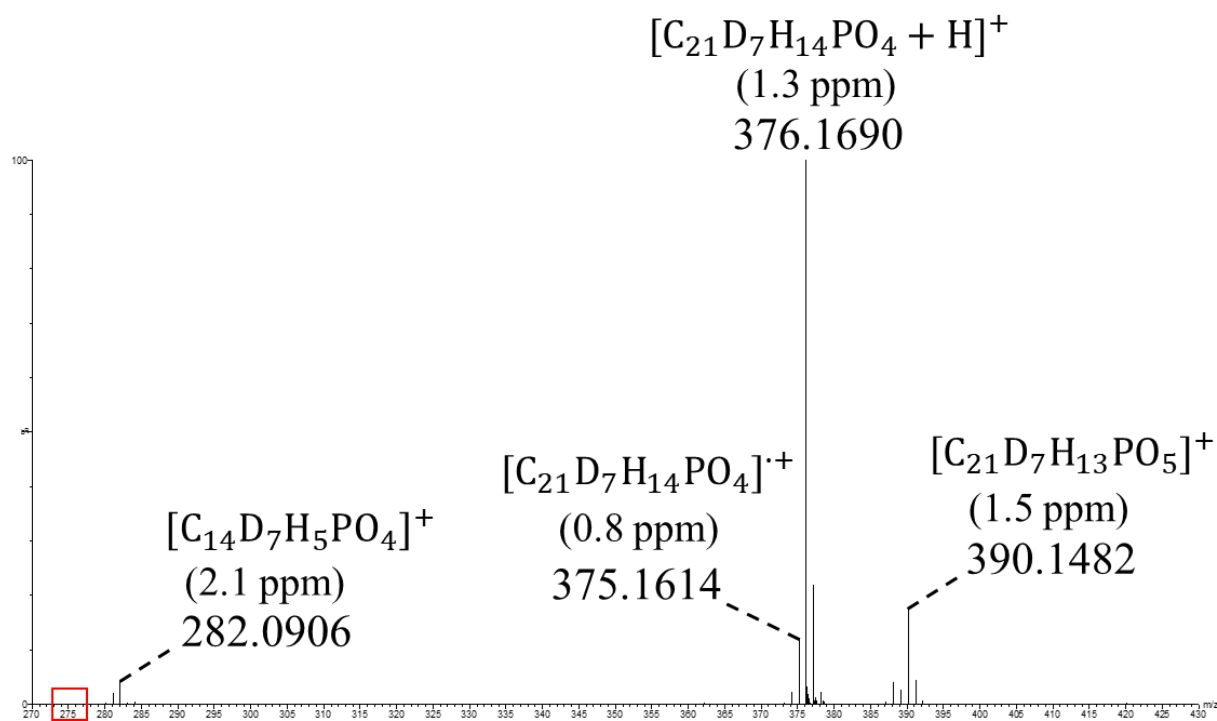
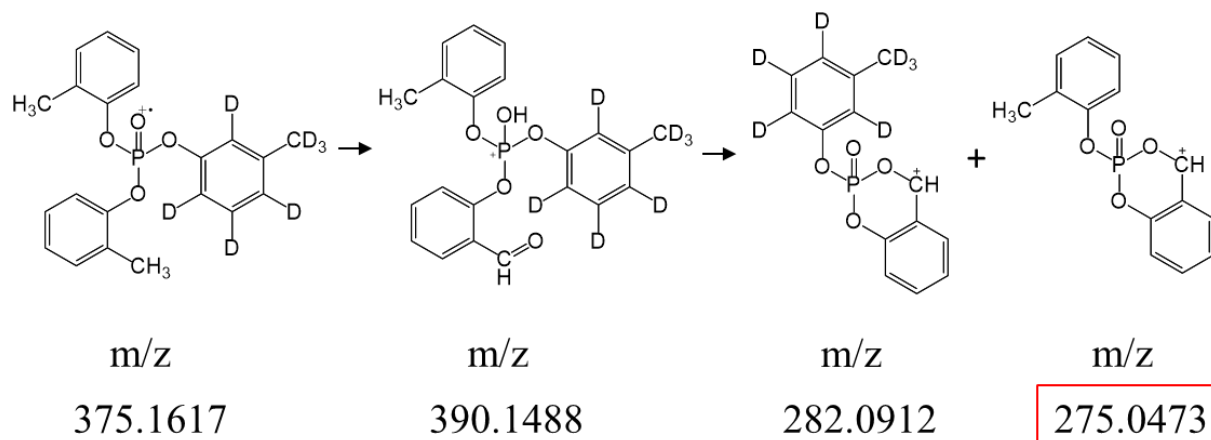


Figure S2.9. The mass spectrum of the synthesized mono-D₇-metadiorthocresyl phosphate (mono-D₇-meta-diortho CP) obtained from the APGC-MS(TOF) with compressed air in positive mode. Unlike ToCP⁺, this molecular ion was observed in the spectrum (m/z=375). It should be noted that between two probable products of this reaction, only one with m/z=282 was observed.

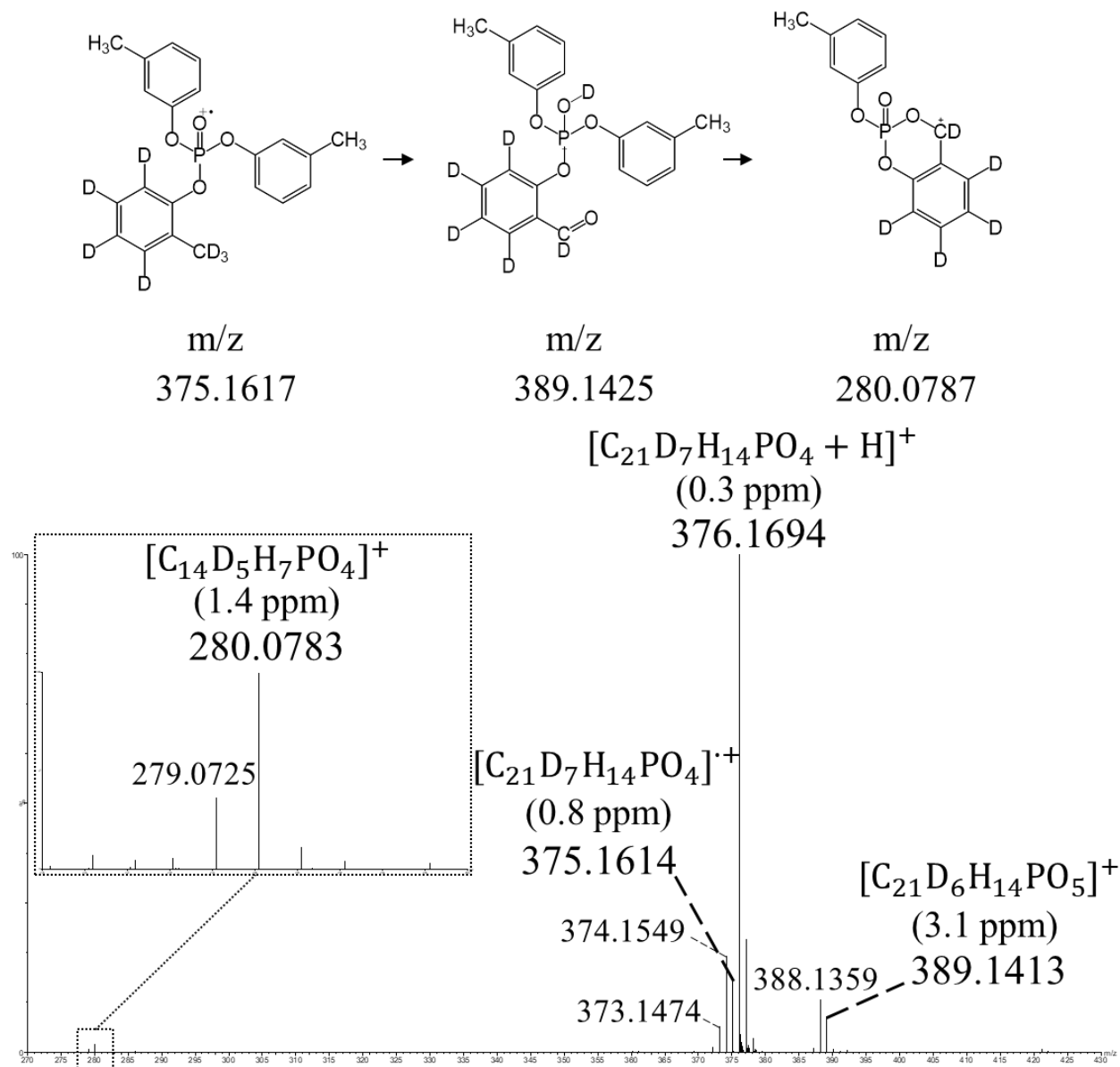


Figure S2.10. The mass spectrum of the synthesized mono-D₇-orthodimetacresyl phosphate (mono-D₇-ortho-dimeta CP) obtained from the APGC-MS(TOF) with compressed air in positive mode. The expected hydrogen-deuterium exchange products of the molecular ion's distonic isomer ($m/z=375$, $m/z=374$ and $m/z=373$) and the first product of the reaction ($m/z=389$ and $m/z=388$) were observed. The final product of the reaction ($m/z=280$) was observed at a low intensity.

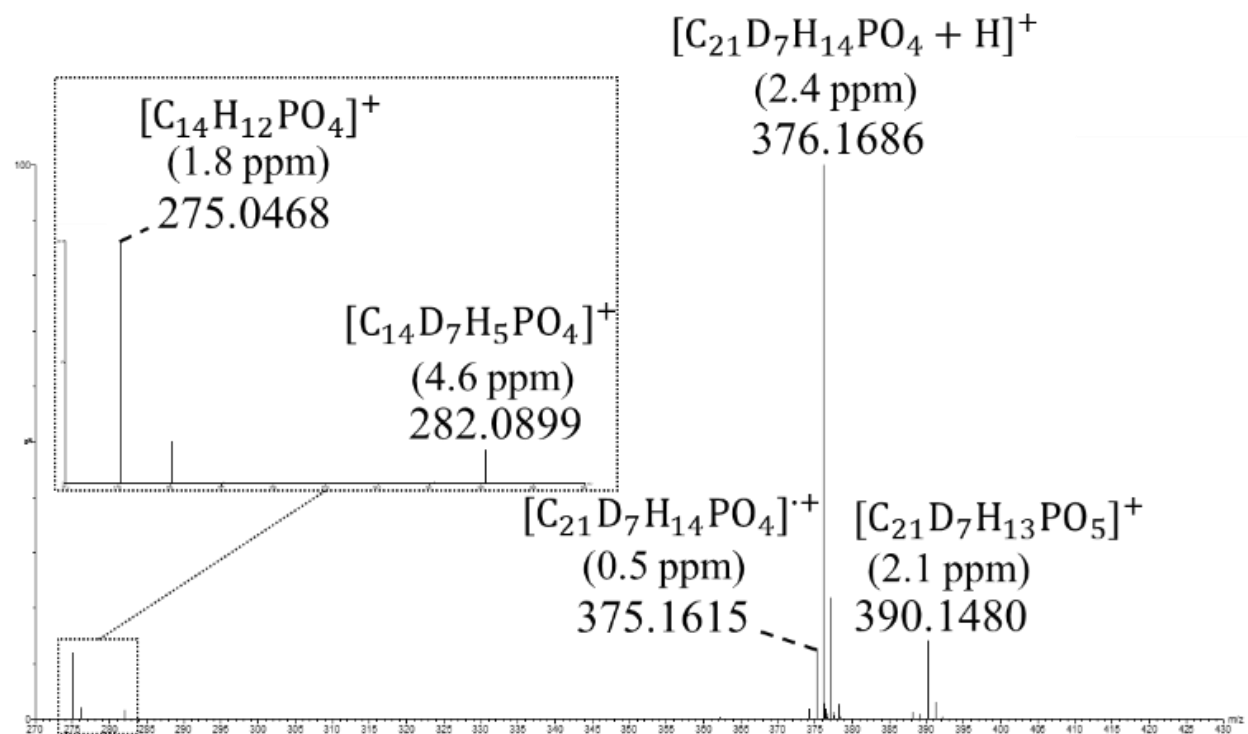
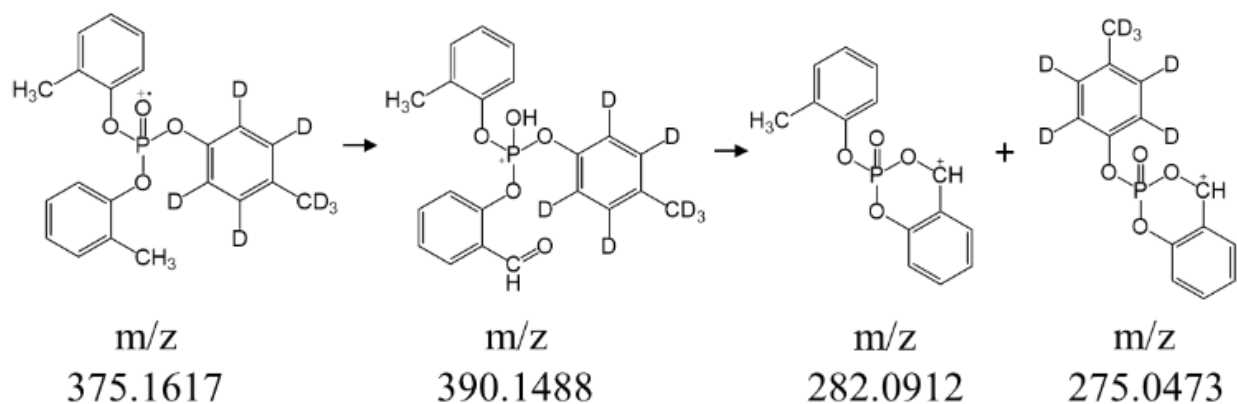


Figure S2.11. The mass spectrum of the synthesized mono- D_7 -paradiorthocresyl phosphate (mono- D_7 -para-diortho CP) obtained from the APGC-MS(TOF) with compressed air in positive mode. The molecular ion ($m/z=375$), protonated ion ($m/z=376$), the first product of the reaction ($m/z=390$) and both final products of the reaction ($m/z=275$ and $m/z=282$) were observed.

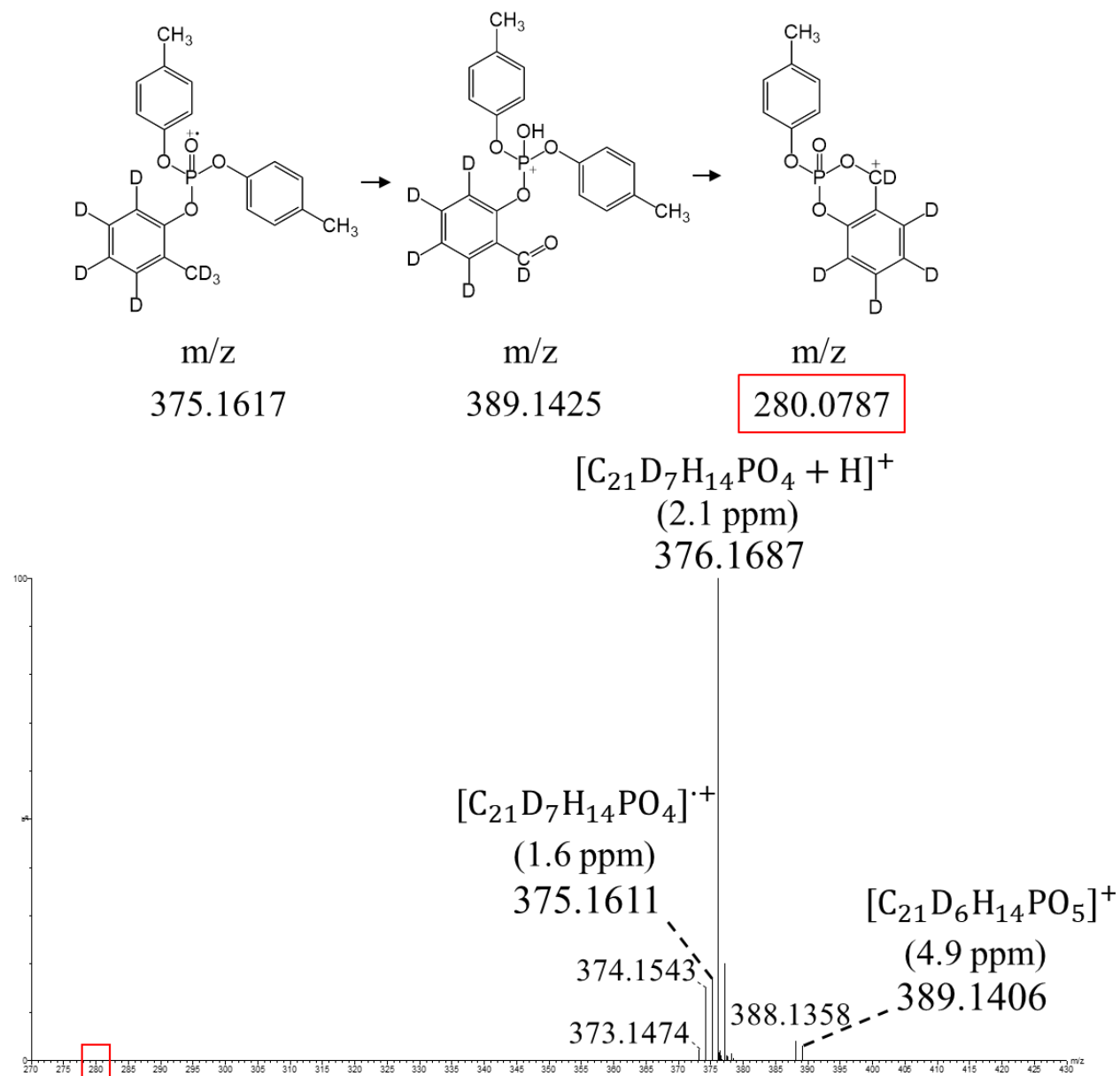


Figure S2.12. The mass spectrum of the synthesized mono-D₇-orthodiparacresyl phosphate (mono-D₇-ortho-dipara CP) obtained from the APGC-MS(TOF) with compressed air in positive mode. The expected hydrogen-deuterium exchange products of the molecular ion's distonic isomer (m/z=375, m/z=374 and m/z=373), the first product of the reaction (m/z=389 and m/z=388) were observed, but no mass peak was observed for the final product of the reaction (m/z=280).

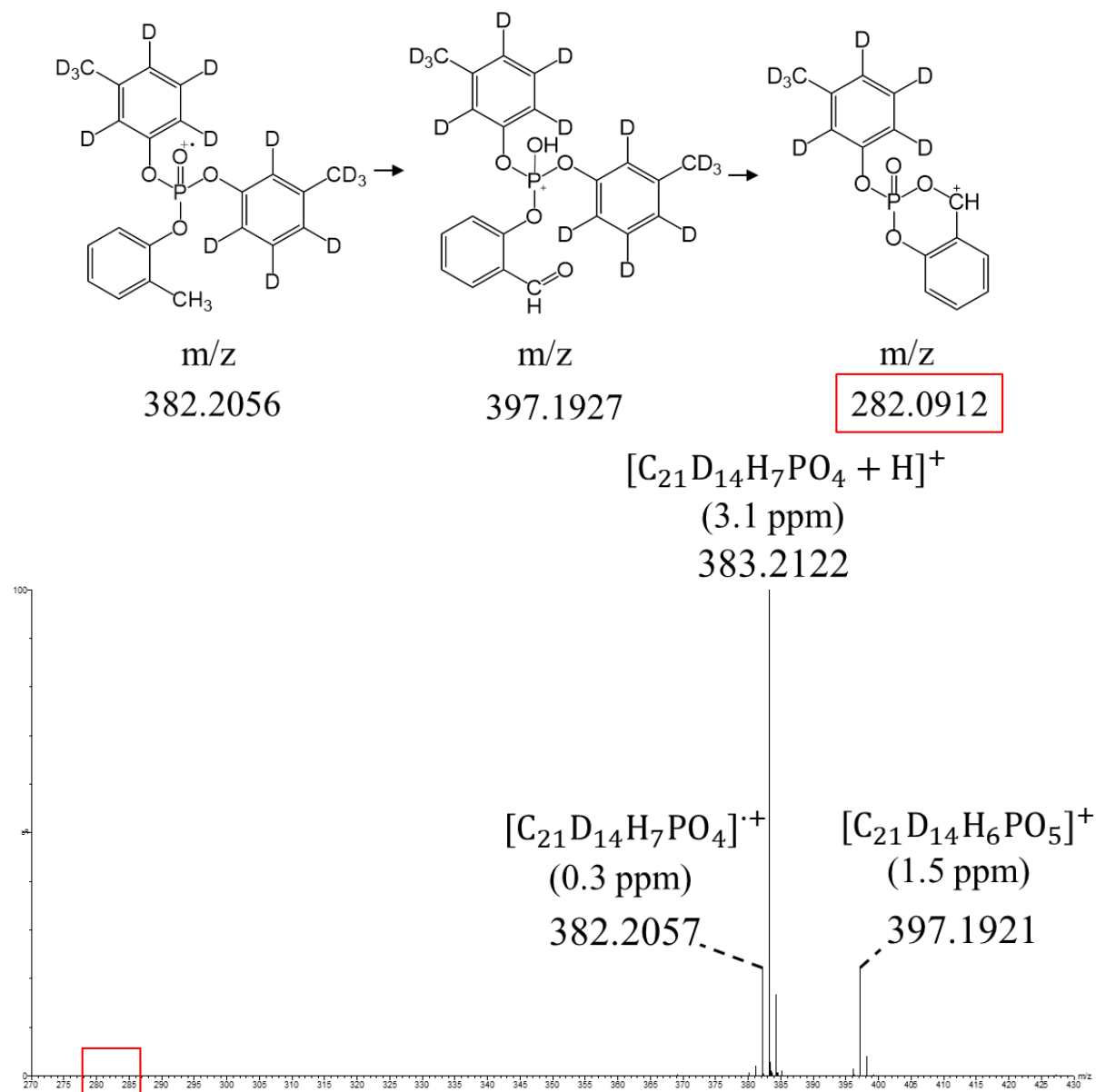


Figure S2.13. The mass spectrum of the synthesized di-D₇-metamonooortho CP (di-D₇-meta-monoortho CP) obtained from the APGC-MS(TOF) with compressed air in positive mode. The molecular ion (m/z=382) and the first product of the reaction (m/z=397) were observed, but the final product of the reaction (m/z=282) did not generate an observable peak in the spectrum.

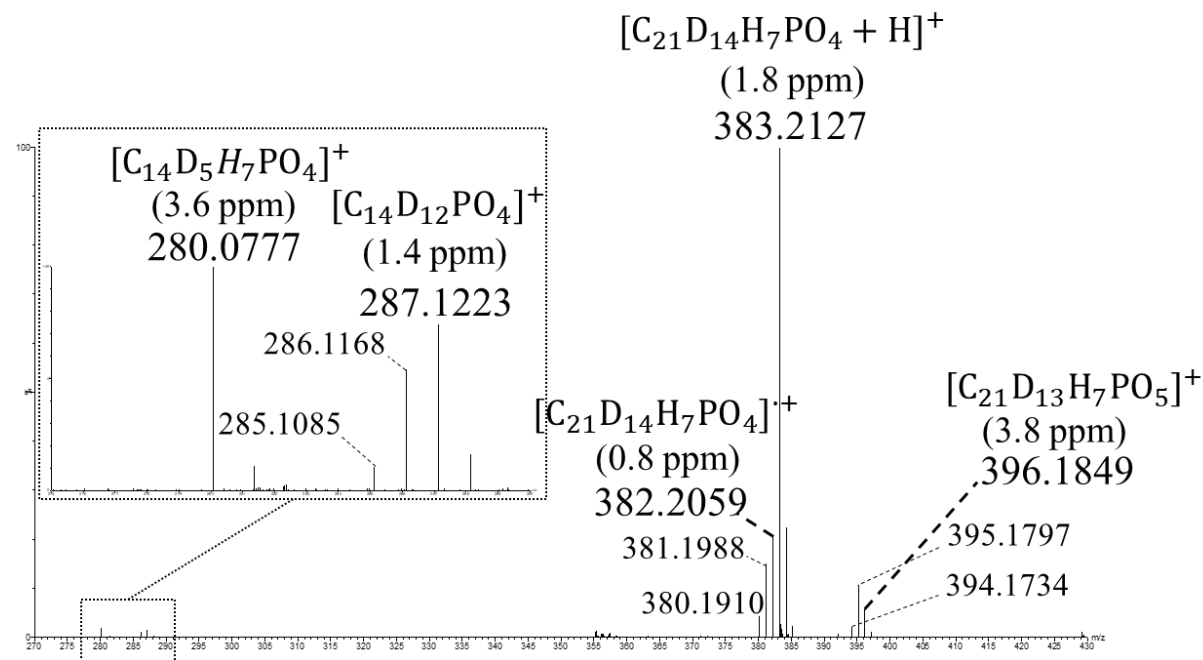
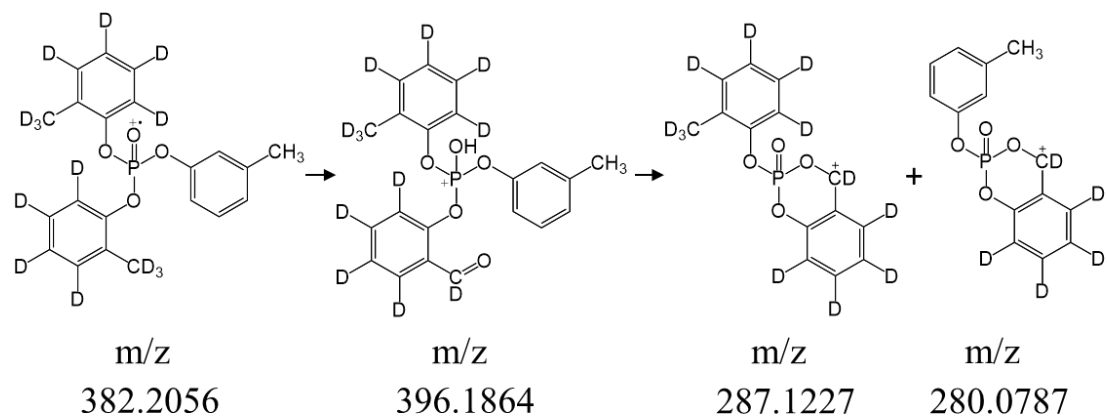


Figure S2.14. The mass spectrum of the synthesized di-D₇-orthomonometacresyl phosphate (di-D₇-orthomonometacresyl CP) obtained from the APGC-MS(TOF) with compressed air in positive mode. The molecular ion (m/z=382), the first product of the reaction (m/z=396), and both final products of the reaction (m/z=280 and m/z=287) were observed. Also, the expected hydrogen-deuterium exchange products of the molecular ion (m/z=381 and m/z=380), the first product (m/z=395 and m/z=396), and the final product with m/z=287 (m/z=286, m/z=285) were observed.

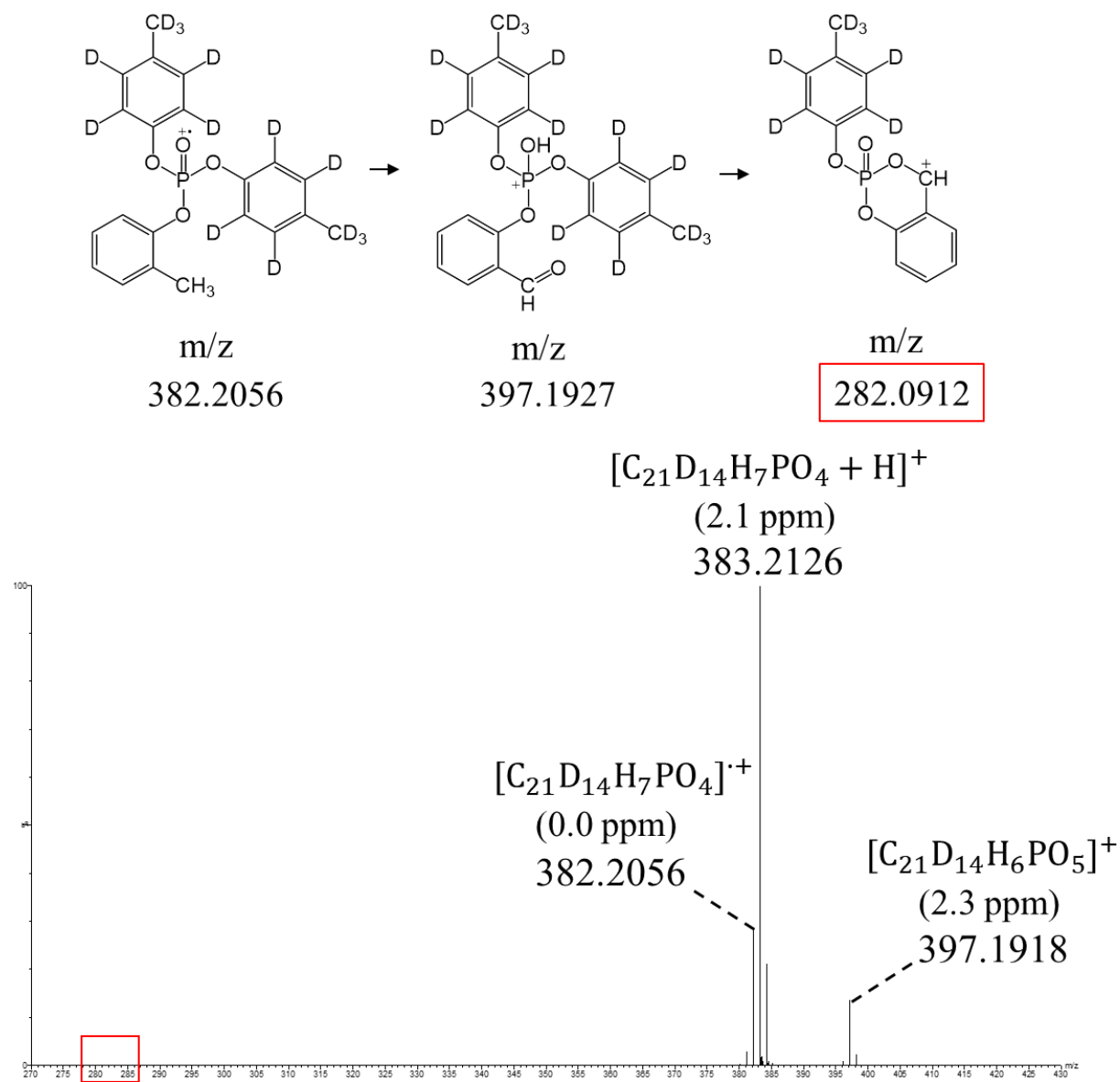


Figure S2.15. The mass spectrum of the synthesized di-D₇-paramonoorthocresyl phosphate (di-D₇-paramonoortho CP) obtained from the APGC-MS(TOF) with compressed air in positive mode. The molecular ion ($m/z=382$) and the first product of the reaction ($m/z=397$) were observed in the spectrum, but the final product of the reaction ($m/z=282$) did not generate observable mass peaks.

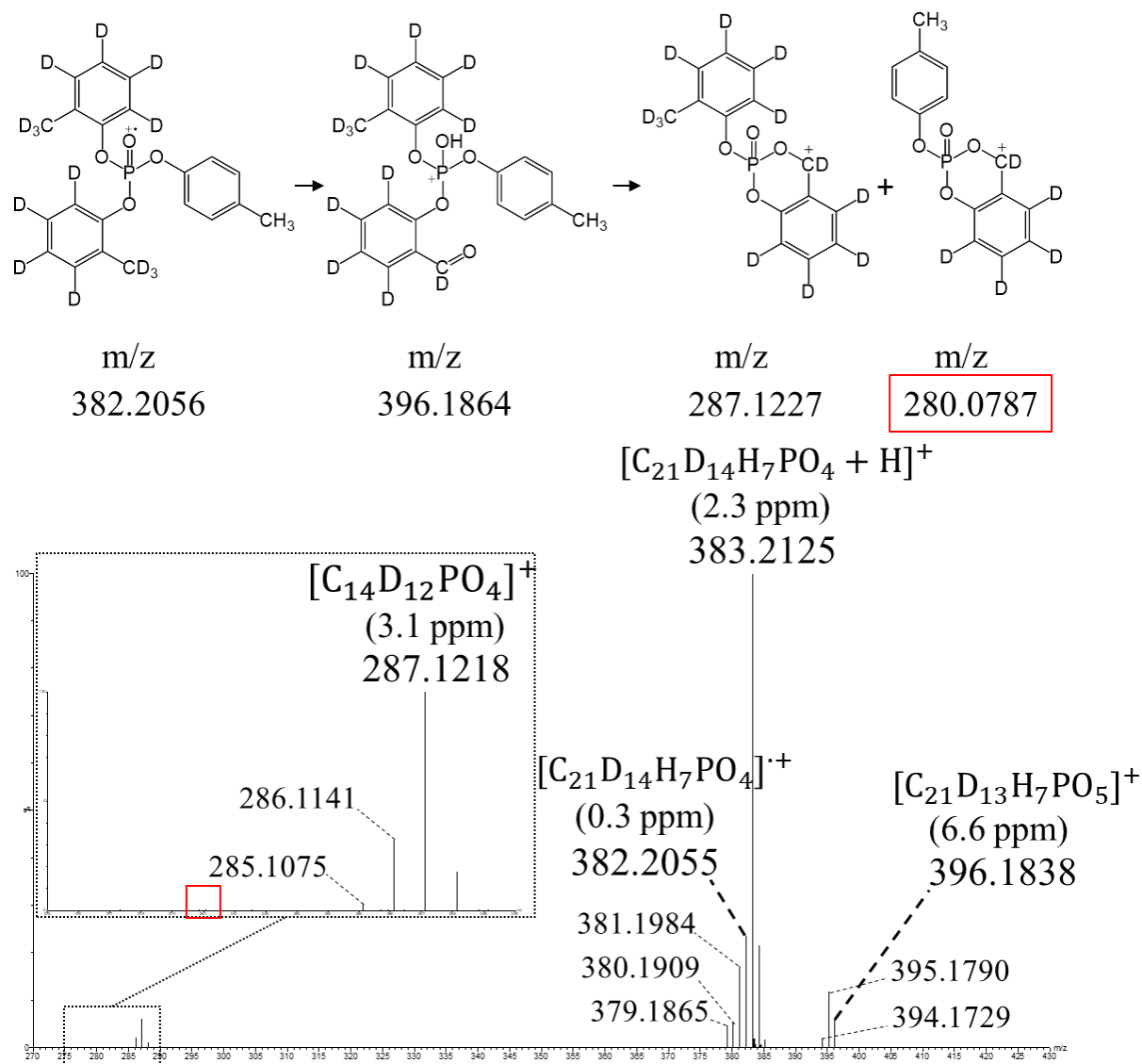


Figure S2.16. The mass spectrum of the synthesized di- D_7 -orthomonoparacresyl phosphate (di- D_7 -orthomonopara CP) obtained from the APGC-MS(TOF) with compressed air in positive mode. The mass peaks of the molecular ion ($m/z=382$), protonated ion ($m/z=383$), the first product of the reaction ($m/z=396$), and one of the final products ($m/z=287$) were observed in the spectrum, but the other final product did not provide observable mass peaks. Hydrogen-deuterium exchange was observed as expected for the first product of the reaction ($m/z=396$, $m/z=395$, and $m/z=394$), the distonic isomers of the molecular ion ($m/z=381$, $m/z=380$, and $m/z=379$), and the final products of the reaction ($m/z=286$, and $m/z=285$).

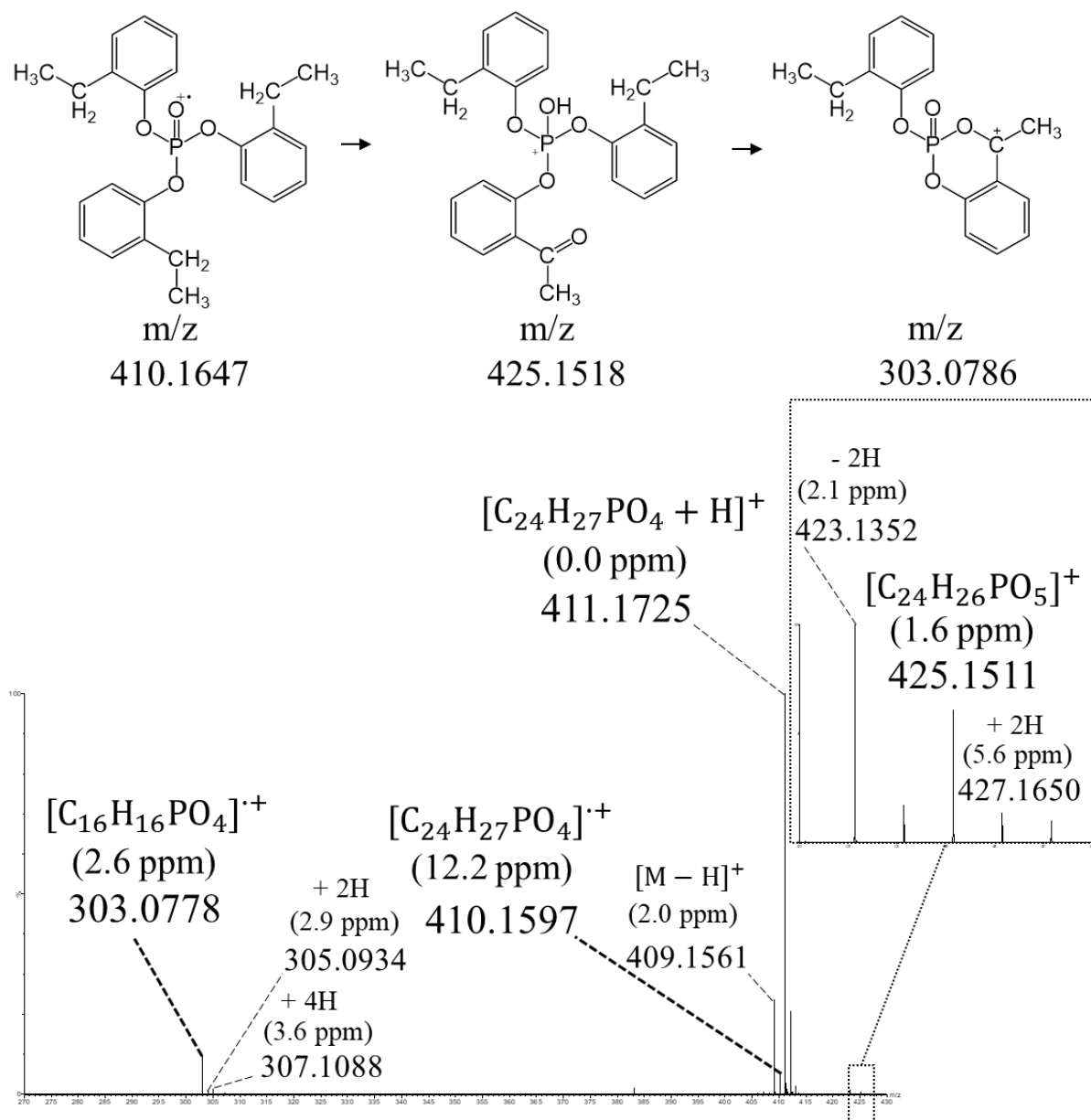


Figure S2.17. The mass spectrum of the synthesized tris 2-ethyl phenyl phosphate (ToEP) obtained from the APGC-MS(TOF) with compressed air in positive mode. The molecular ion ($m/z=410$), the first product ($m/z=425$), and the final product ($m/z=303$) of its reaction with O₂ were observed in the mass spectrum. In addition to the main reaction (shown by horizontal arrows), side reactions, including the loss of hydrogens or addition of hydrogens (shown in vertical arrows), took place due to steric effects.

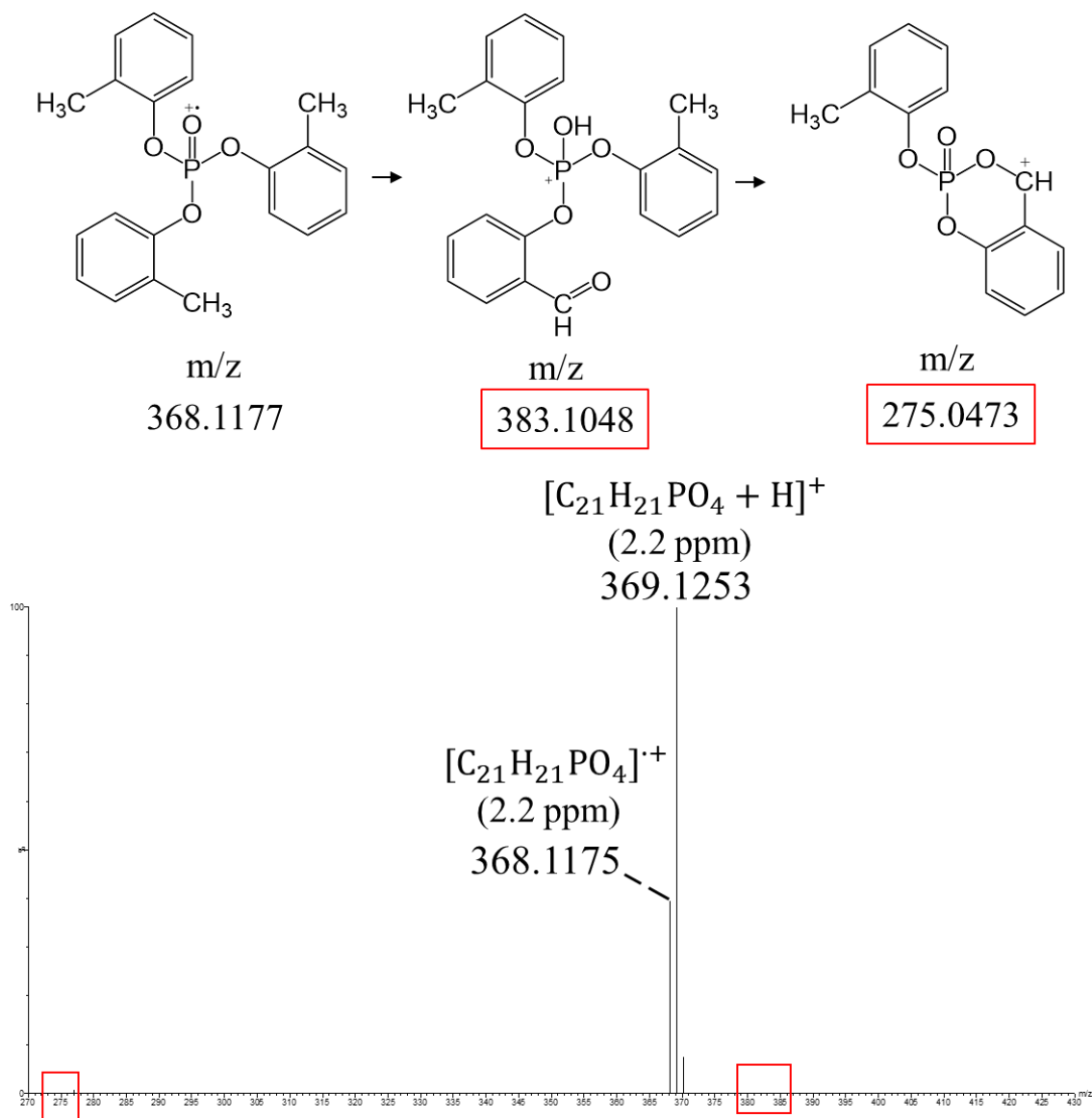


Figure S2.18. The mass spectrum of the standard triorthocresyl phosphate (ToCP) obtained from the APGC-MS(TOF) with N_2 in positive mode.

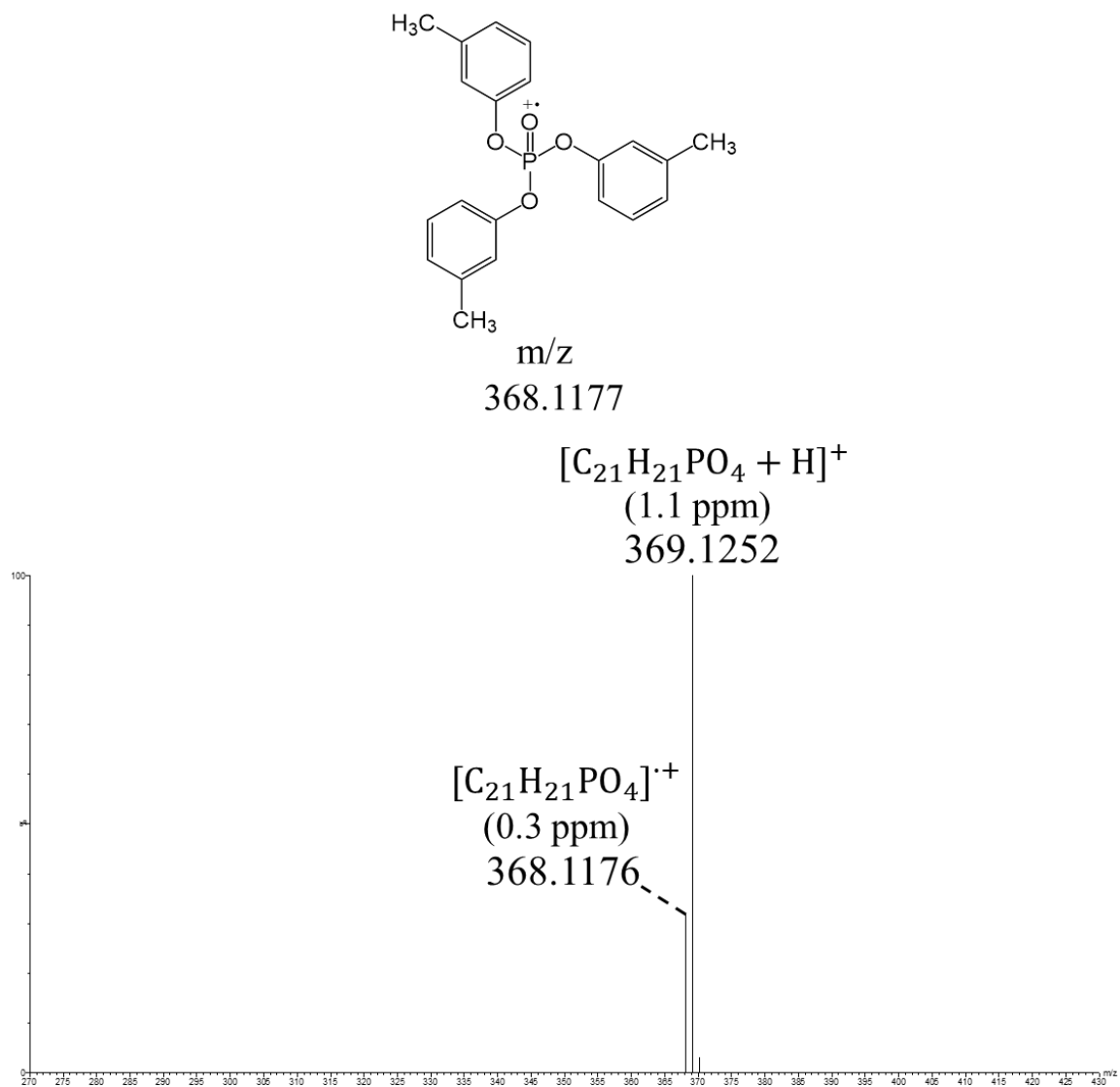
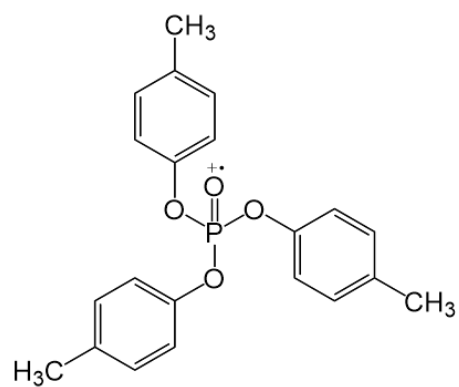


Figure S2.19. The mass spectrum of the standard trimetacresyl phosphate (TmCP) obtained from the APGC-MS(TOF) with N₂ in positive mode.



m/z
368.1177

$[C_{21}H_{21}PO_4 + H]^+$
(2.4 ppm)
369.1247

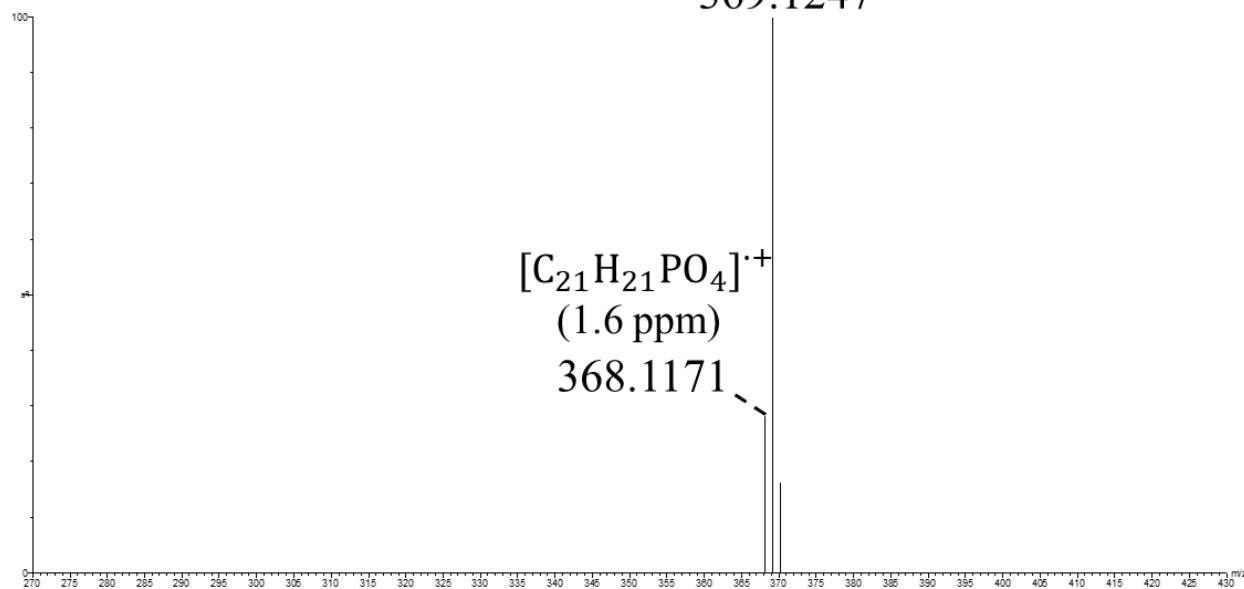


Figure S2.20. The mass spectrum of the standard triparacresyl phosphate (TpCP) obtained from the APGC-MS(TOF) with N₂ in positive mode.

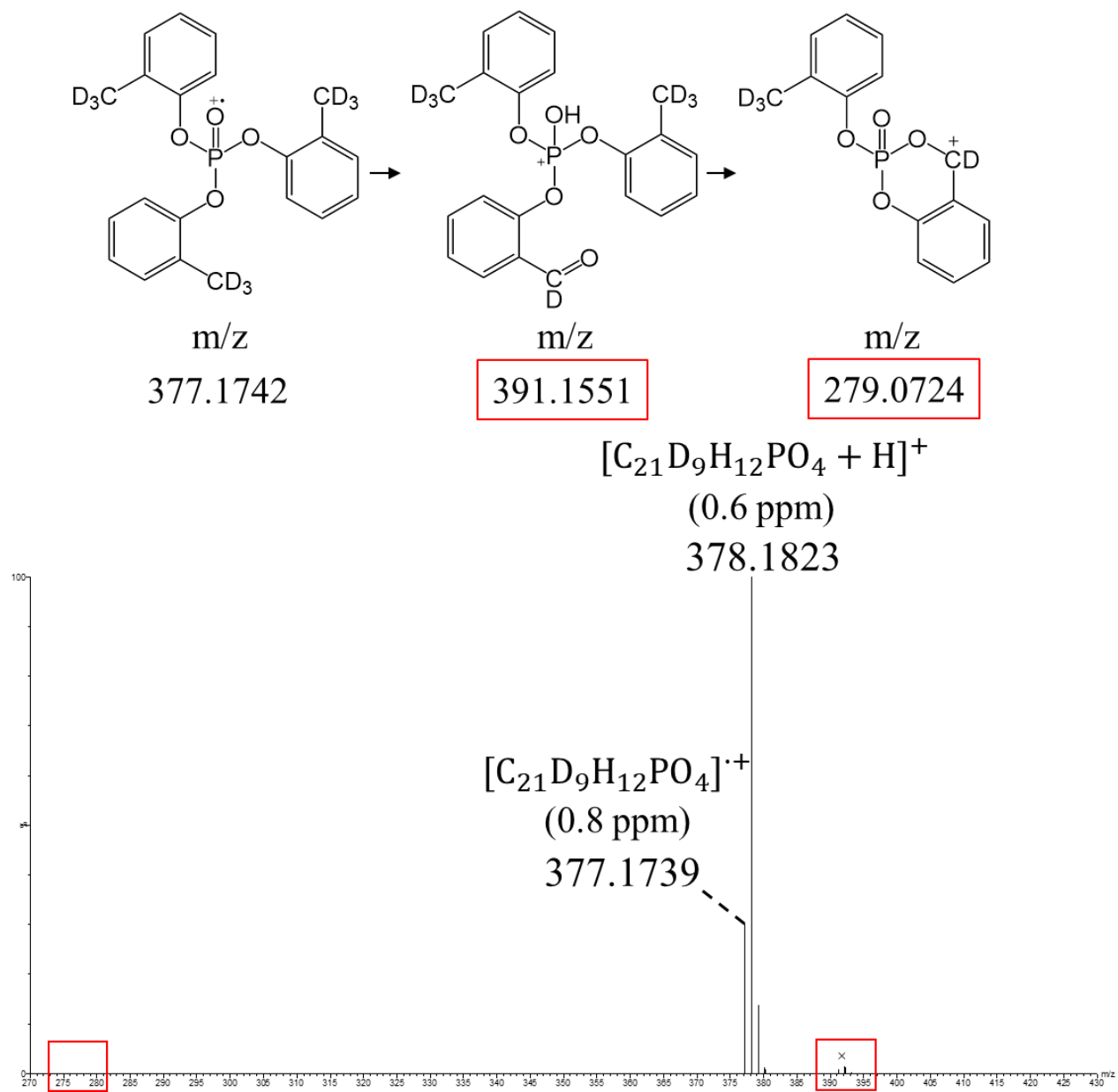


Figure S2.21. The mass spectrum of the synthesized D₉-labeled tri-CD₃-ortho cresyl phosphate (tri-CD₃-*o*CP) obtained from the APGC-MS(TOF) with N₂ in positive mode.

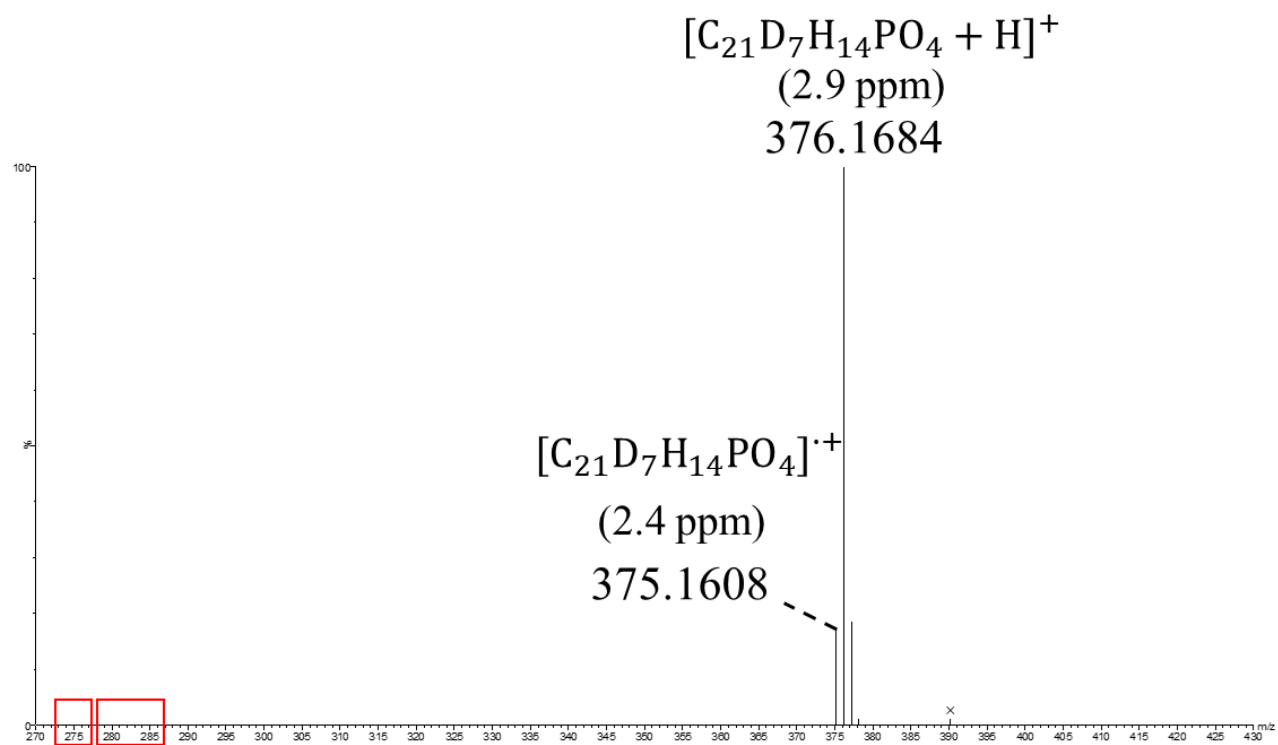
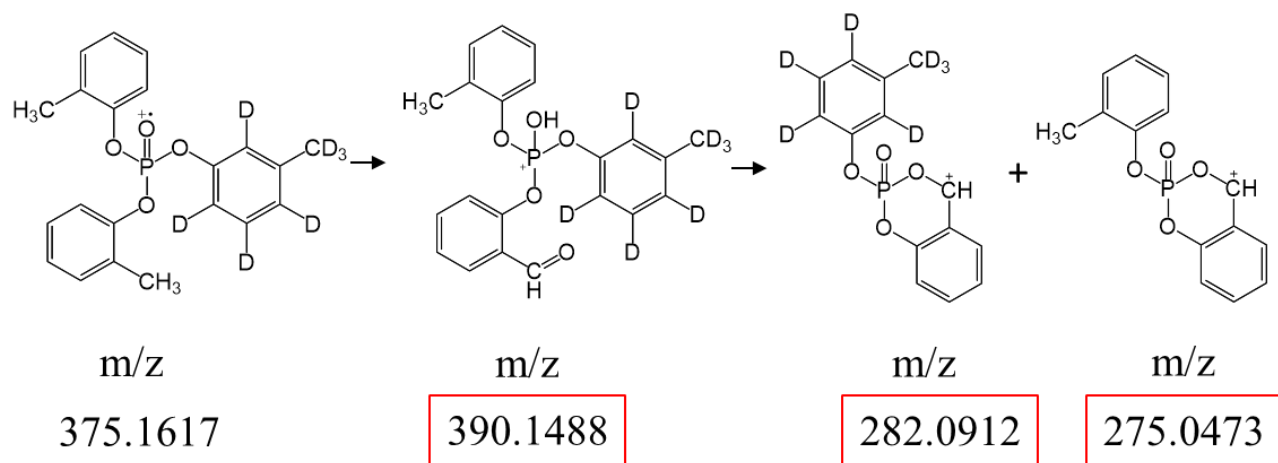


Figure S2.22. The mass spectrum of the synthesized mono-D₇-metadiorthocresyl phosphate (mono-D₇-meta-diortho CP) obtained from the APGC-MS(TOF) with N₂ in positive mode.

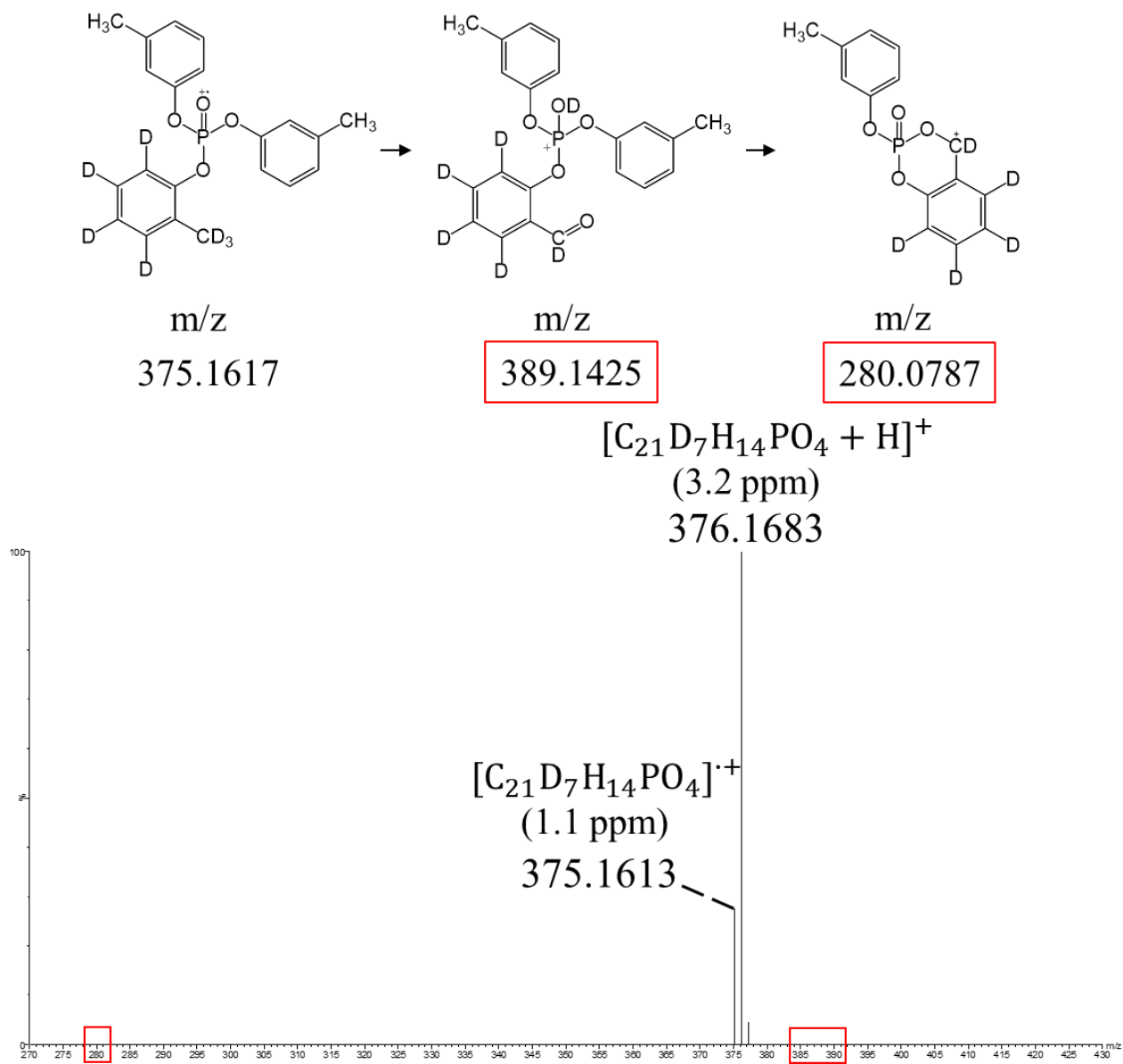
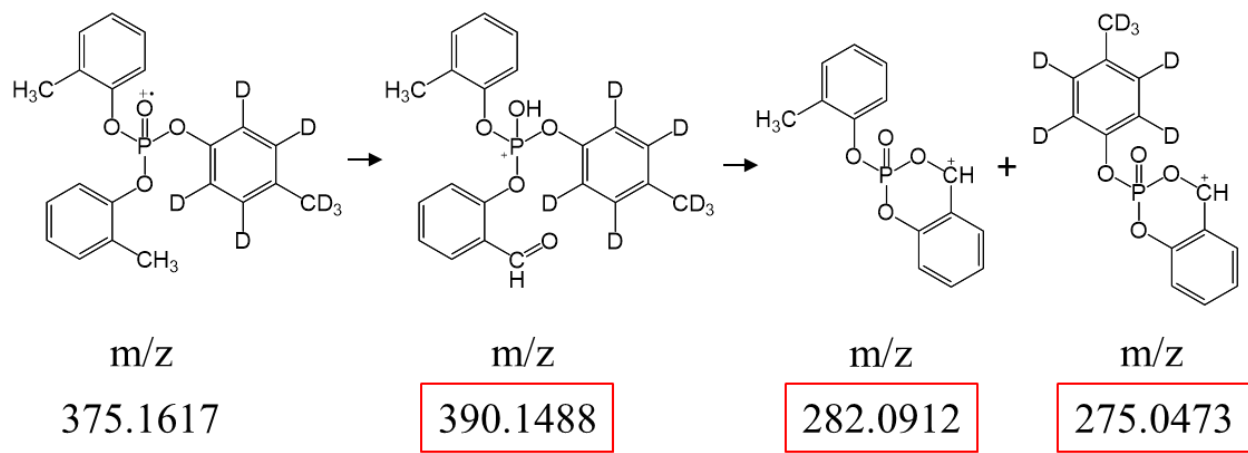


Figure S2.23. The mass spectrum of the synthesized mono-D₇-orthodimetacresyl phosphate (mono-D₇-ortho-dimeta CP) obtained from the APGC-MS(TOF) with N₂ in positive mode.



$[C_{21}D_7H_{14}PO_4 + H]^+$
 (4.6 ppm)
 376.1678

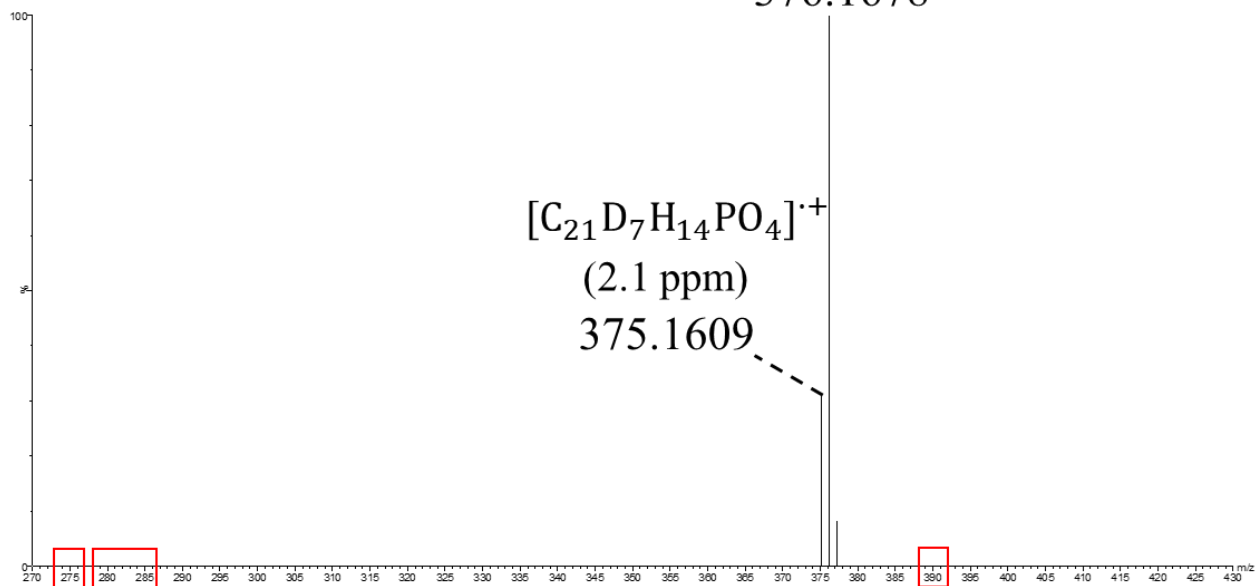


Figure S2.24. The mass spectrum of the synthesized mono-D₇-para-diortho cresyl phosphate (mono-D₇-para-diortho CP) obtained from the APGC-MS(TOF) with N₂ in positive mode.

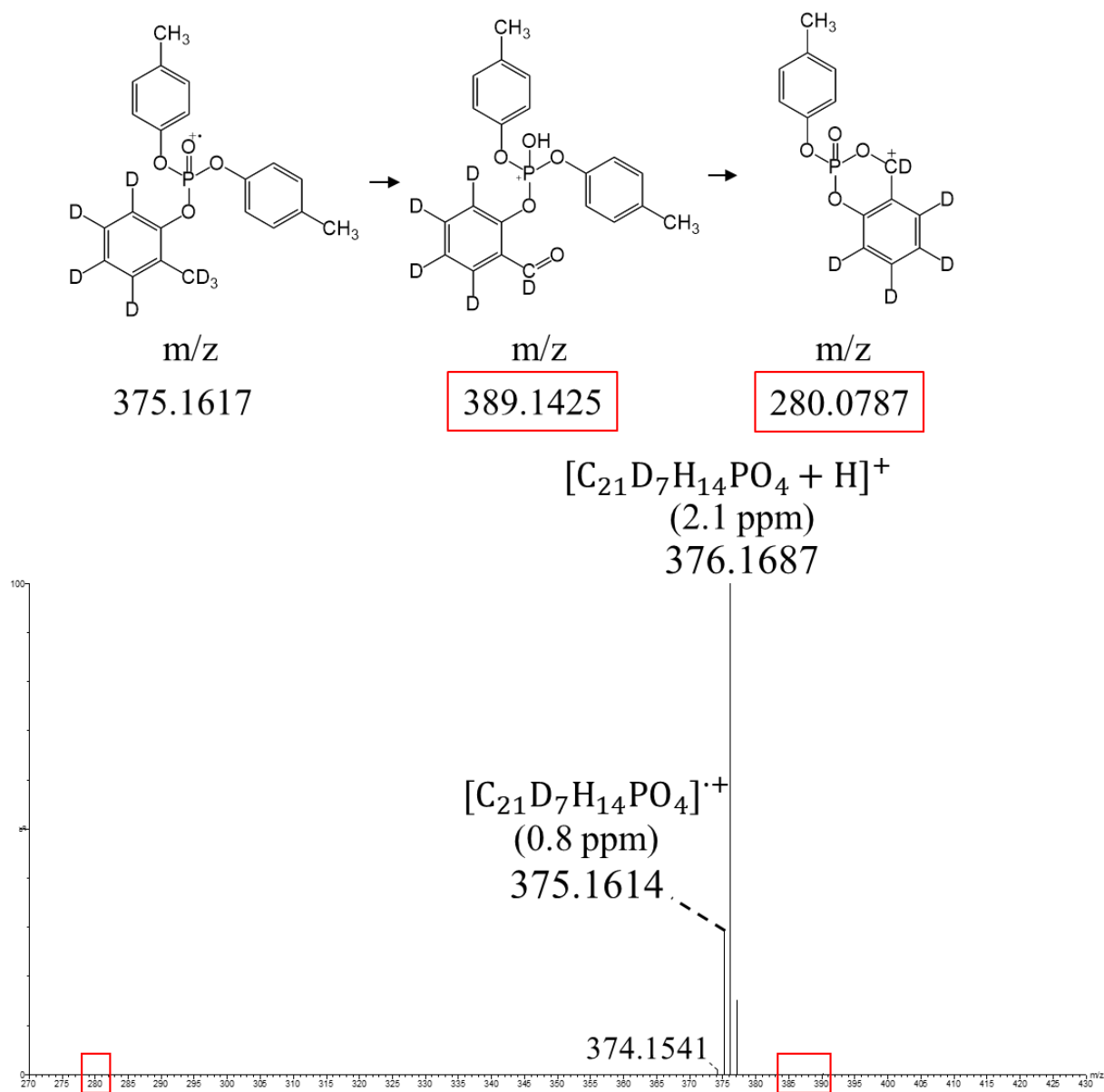


Figure S2.25. The mass spectrum of the synthesized mono-D₇-orthodiparacresyl phosphate (mono-D₇-ortho-dipara CP) obtained from the APGC-MS(TOF) with N₂ in positive mode.

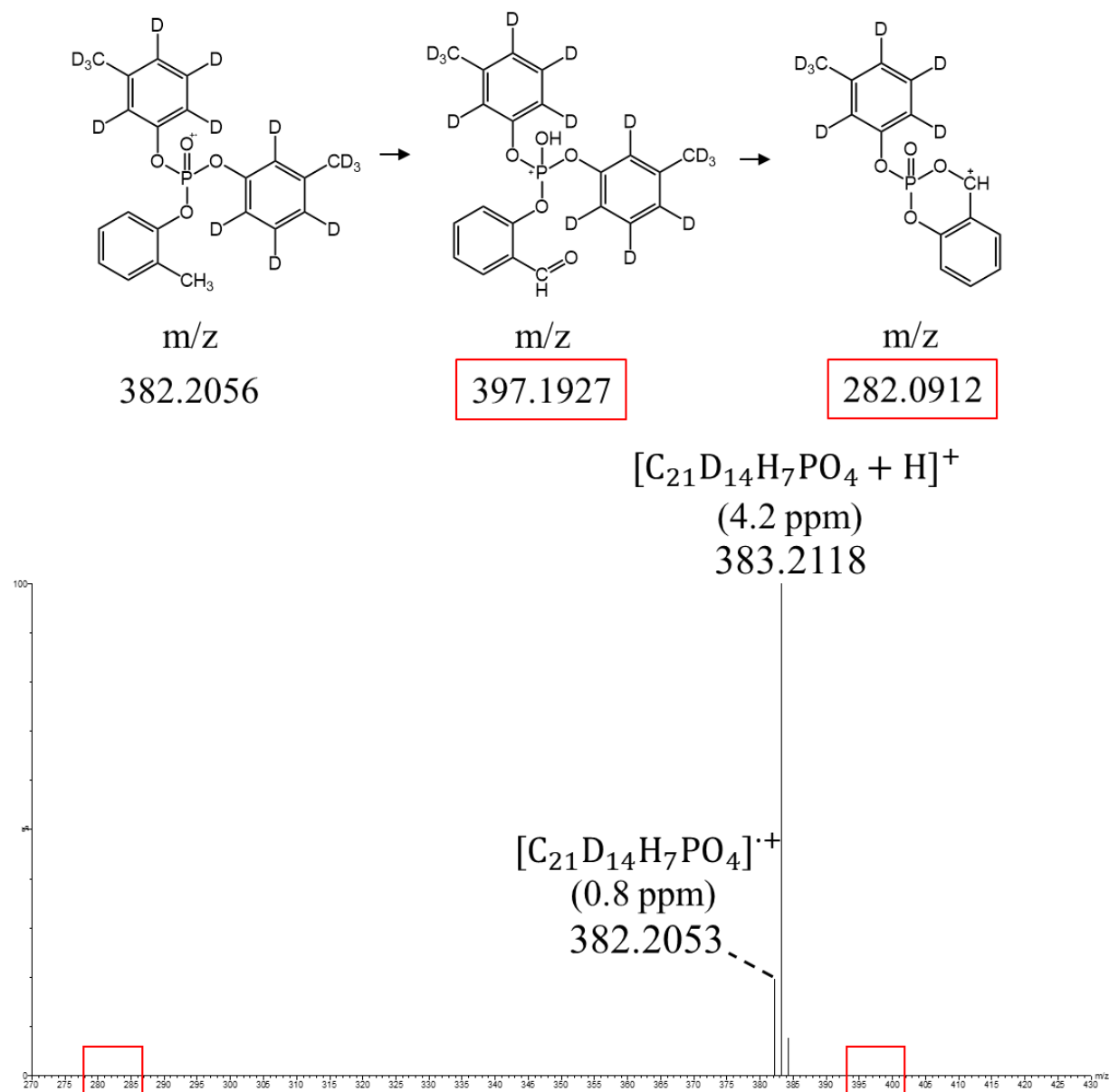


Figure S2.26. The mass spectrum of the synthesized di- D_7 -metamonoothocresyl phosphate (di- D_7 -metamonootho CP) obtained from the APGC-MS (TOF) with N_2 in positive mode.

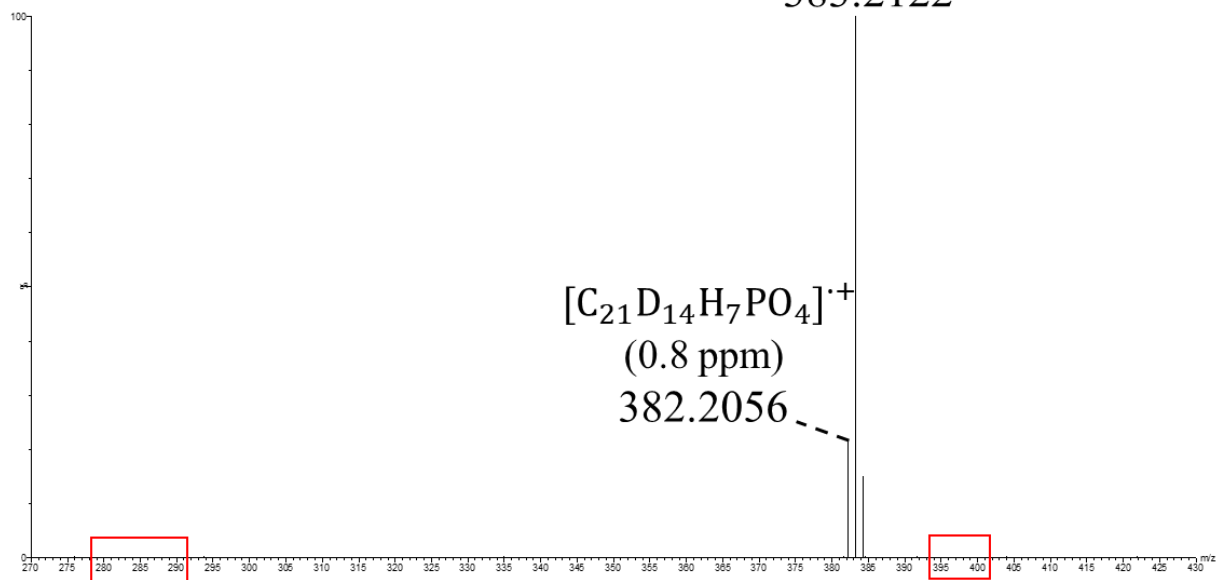
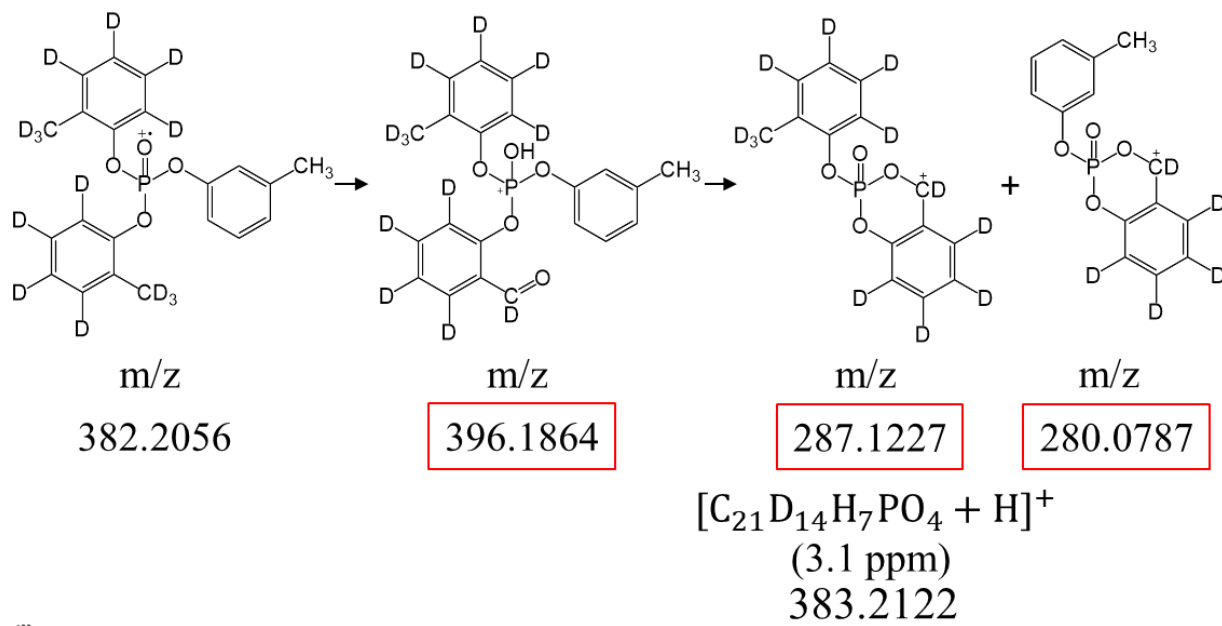


Figure S2.27. The mass spectrum of the synthesized di-D₇-orthomonometacresyl phosphate (di-D₇-orthomonometacresyl CP) obtained from the APGC-MS (TOF) with N₂ in positive mode.

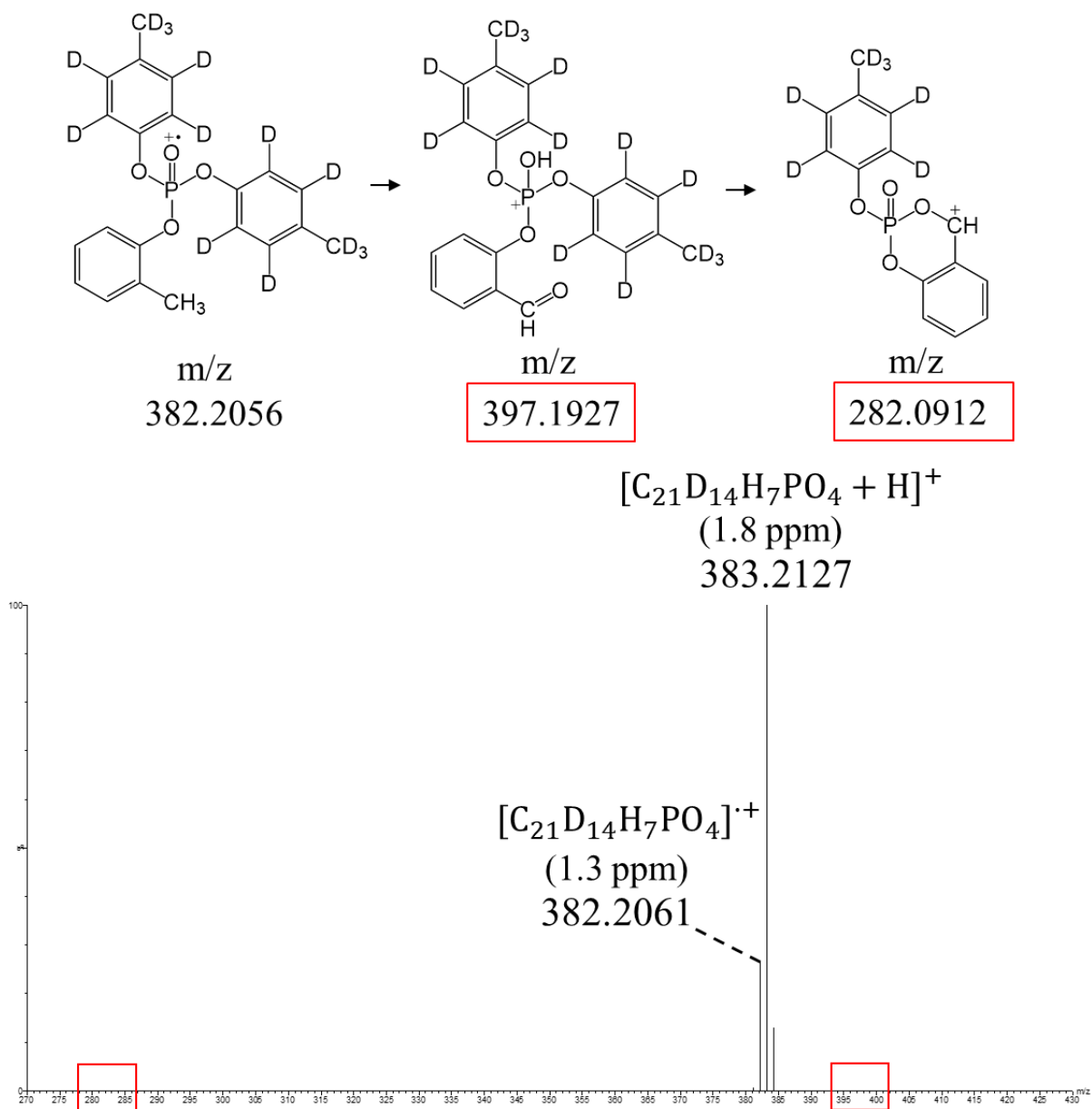


Figure S2.28. The mass spectrum of the synthesized di-D₇-paramonortho cresyl phosphate (di-D₇-paramonortho CP) obtained from the APGC-MS(TOF) with N₂ in positive mode.

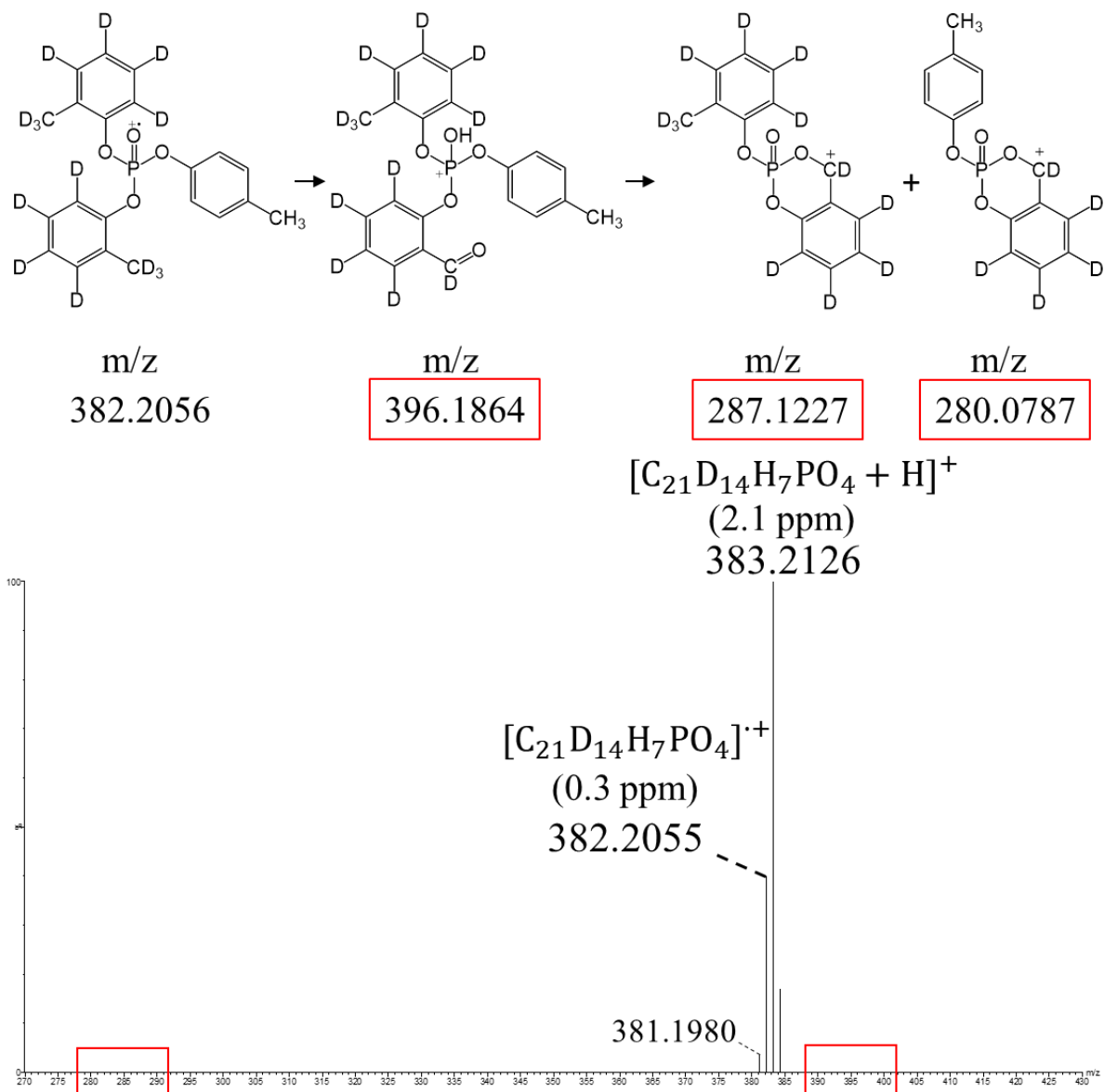


Figure S2.29. The mass spectrum of the synthesized di- D_7 -orthomonoparacresyl phosphate (di- D_7 -orthomonopara CP) obtained from the APGC-MS(TOF) with N_2 in positive mode.

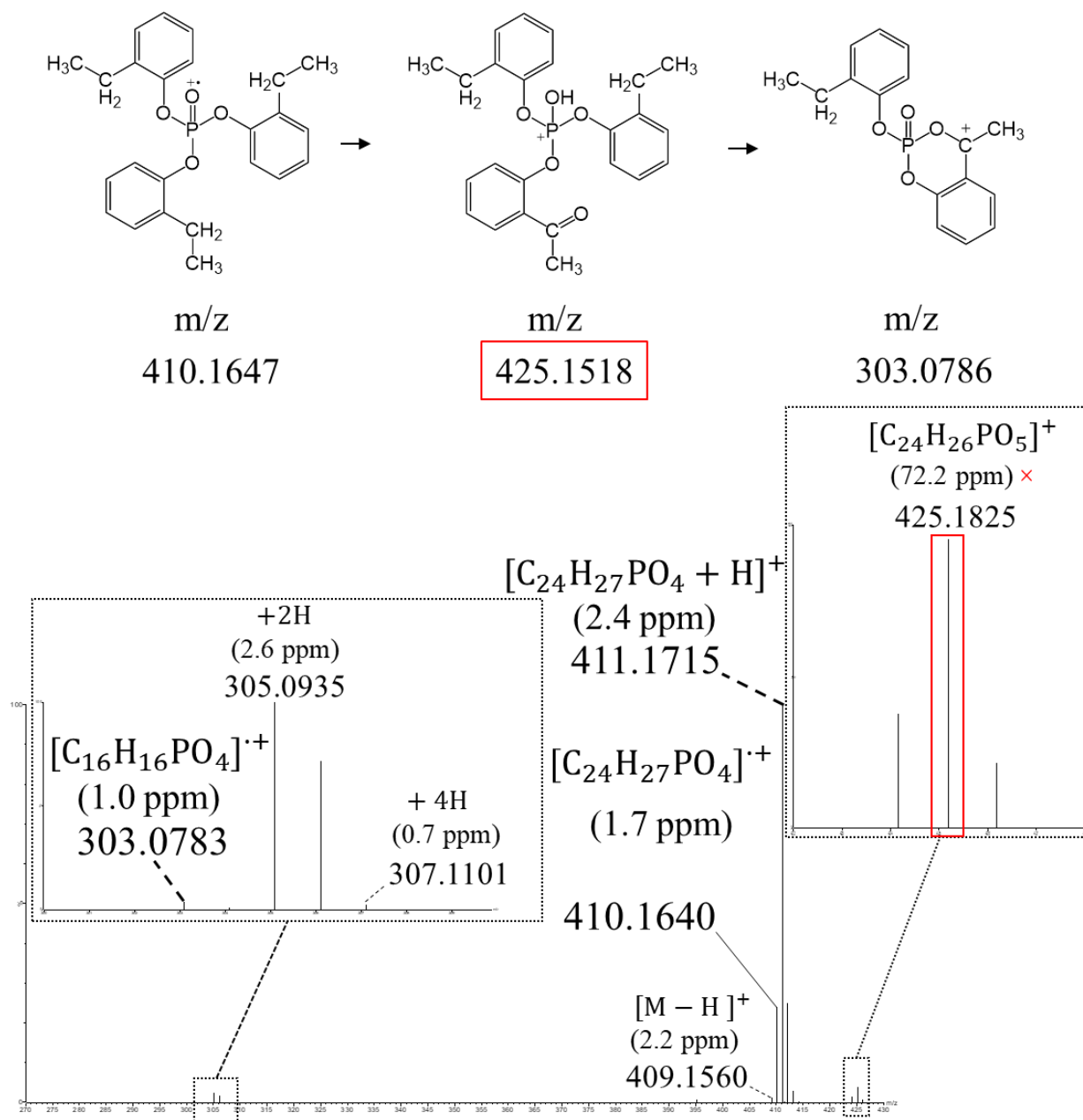


Figure S2.30. The mass spectrum of the synthesized tris 2-ethyl phenyl phosphate (ToEP) obtained from the APGC-MS(TOF) with N_2 in positive mode.

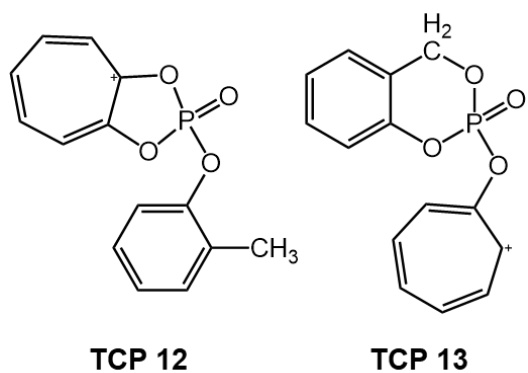


Figure S2.31. The structures of TCP12 and TCP13; the benzyllium-tropylium ion rearrangement products of TCP10 and TCP11.

Table S2.5 The list of all TCP⁺⁺ and [CBDP-H]⁺ isomers are provided with the corresponding MOBCAL-MPI predicted and cIM measured CCS values. The CCS resolution is calculated for the isomers with the same m/z ratios. (For m/z=275 and m/z=368, respectively, [CBDP-H]⁺ and ToCP⁺⁺ were chosen as reference in calculating the CCS resolution).

Structure	Predicted CCS	SD (%)	CCS Resolution
ToCP (m/z=368)	179.66	1.58	
[ToCP+O-H] ⁺	183.71	1.11	
[CBDP-H] ⁺ (TCP 9) (m/z=275)	159.54	1.08	
TCP 10 (m/z=275)	156.02	1.25	45
TCP 11 (m/z=275)	159.53	1.04	1600
TCP 12 (m/z=275)	158.01	1.15	103
TmCP (m/z=368)	197.35	0.90	11
TpCP (m/z=368)	182.57	1.00	63

Chapter 3. A Mechanistic Analysis of the Ion-Molecule Reactions between Oxygen and Tetrahalogenated Dibenzo-*p*-Dioxins

Abstract: Tetrachlorodibenzo-*p*-dioxins (TCDDs) are infamous for their toxicity and persistence in the environment after being generated from the combustion of polychlorinated compounds and polymers. Analysis of mixtures of dioxins is difficult due to their complexity and limited availability of authentic standards. Hard ionization techniques, including electron ionization (EI), cannot distinguish between toxic and non-toxic isomers due to the lack of isomer selective fragmentations. However, when atmospheric pressure chemical ionization (APCI) is used in negative mode, TCDD isomers undergo structure-diagnostic bond cleavages. Previous studies have provided us with ionic dissociation products of two groups of ion-molecule reactions between TCDDs and O₂; first, the oxidation reaction resulting in [M-Cl+O]⁻, and second, the ether cleavage reaction resulting in a radical anion and a neutral product. However, the mechanism of these reactions remains unknown. In this study, we proposed mechanisms for both oxidation and ether cleavage reactions and investigated them by DFT calculations. We also calculated theoretical collision cross section (CCS) values for the ether cleavage products using MobCal-MPI to support further studies on separating their isomeric structures using cyclic-ion mobility. These mechanisms will guide the eventual development of experimental methods that can differentiate between (potentially) toxic and non-toxic mixed halogenated dibenzo-*p*-dioxins.

3.1. Introduction

Polychlorinated dibenzo-*p*-dioxins and furans (PCDD/Fs) consist of two chlorinated benzene rings (4-8 Cl atoms) connected by one or two oxygen bridges. This class of compounds contains 75 PCDD and 135 PCDF congeners [1]. They have been monitored in air, soil, sediment, sewage sludge, milk and biological tissue for a half century due to their toxicity and persistence in the environment [2]. PCDD/Fs are also formed as byproducts in the synthesis of chlorinated aromatic compounds (i.e. agent orange [3] and chlorophenols [4]) and by thermal conversion processes during the combustion [4,5] of polychlorinated biphenyls (PCBs), polychlorophenols [5], polyvinylchloride (PVC) [6], and other chlorinated chemicals and polymers [5,6]. The Plastimet Inc. fire in Hamilton, Ontario, Canada (July, 1997) [7–9], one the largest industrial fires in North America, was an example of the generation and release of PCDD/Fs together with polybrominated dibenzo-*p*-dioxins (PBDD/Fs) and mixed halogenated dioxins and furans (PXDD/Fs) [8,10]. At least 400 tonnes of polyvinyl chloride (PVC) and polyurethanes were consumed in the fire [7–9]. It is suspected that the decomposition of brominated flame retardants was also an additional source of PXDD/Fs formation [7–9,11]. Furthermore, PCDD/Fs, PBDD/Fs and PXDD/Fs are emitted to the environment under milder conditions from other sources, including municipal incineration [12] and electronics waste recycling [13,14].

PCDD/Fs are carcinogenic and can cause reproductive and developmental issues, immune system damage, and endocrine system interference [15–18]. The number of lateral-positioned chlorines directly affects the level of PCDD/Fs toxicity which is mediated by the aryl-hydrocarbon receptor (AhR) [1,19]. AhR binds to PCDD/Fs and transfers them to the nucleus affecting the genes involved in xenobiotic metabolism [1]. The ligand–receptor binding affinities between each PCDD/Fs congener and AhR determines the level of toxicity which is higher for congeners with

lateral-positioned chlorines than non-lateral positioned counterparts [20,21]. Among all 210 congeners of PCDD/Fs, the 2,3,7,8-tetrachlorinated dibenzo-*p*-dioxin (TCDD) with all Cl atoms on the lateral positions is the most toxic since it possesses the highest affinity toward the AhR. [1] Since PBDD/Fs and PXDD/Fs show similar chemical properties as PCDD/Fs, they can also bind to AhR exhibiting toxic properties [22] with 2,3,7,8 substituted tetrabrominated (TBDD) and mixed tetrahalogenated (TXDD) dibenzo-*p*-dioxins being more dangerous [23,24].

The most common technique for the analysis of PCDDs [25], PBDDs [26], and PXDDs [27] is gas chromatography coupled to mass spectrometry (GC-MS). Instrumental analysis of these dioxins is complicated because of the large number of isomers which require complex separation techniques and limited availability of authentic standards [28]. Hard ionization techniques, such as electron ionization (EI), cannot provide enough information on the structures of TCDDs, TBDDs and TXDDs due to lack of isomer selective fragmentations [29]. Fernando et al. studied tetrahalogenated dibenzo-*p*-dioxins using atmospheric pressure chemical ionization (APCI) mass spectrometry [10]. They concluded that APCI⁻ is the only ionization technique that can provide sufficient structural information in the resulting mass spectra to distinguish between lateral and non-lateral substituted TCDD, TBDD and TXDD isomers. The reason for this is the ion-molecule reactions that occur between tetrahalogenated dibenzo-*p*-dioxins and oxygen in the ionization source. One of these reactions is the oxidation of dioxins to their pseudomolecular ions ($[M-Cl+O]^-$). The second is an ether cleavage reaction that is selective towards the dioxins which contain lateral-positioned halogens [10]. However, the mechanisms of these reactions have not yet been established. In the present study, we apply density functional theory (DFT) to investigate the proposed mechanisms of these ion-molecule reactions. We also calculate the collision cross section (CCS) values of the ether cleavage products for further structural studies using cyclic-ion mobility.

The selectivity of these mechanisms provides a novel strategy for identifying toxic PXDD/Fs congeners present in environmental samples.

3.2. Experimental Section

3.2.1. Computational methods

The Gaussian 16 suite of programs available on the Atlantic Computational Excellence network (ACEnet) cluster was employed to perform all DFT calculations using the B3LYP functional in combination with the 6-311G (2d,p) basis set [30]. The local minima and connecting transition structures (TS) were optimized and then validated by frequency analysis at the same level of theory. The total energies (in Hartree) and relative energies (in kcal/mol) for the reactants, intermediates, transition structures, product ions and neutrals of both reactions are reported in Table S3.1. MobCal-MPI v1.2 available on the SHARCNET platform was used to calculate the theoretical collision cross section (CCS) values.

Geometries were optimized prior to MobCal analysis using DFT at the B3LYP/6-31++G(d,p) level of theory. A python module provided by Hopkins et al. [31], in addition to Open Babel 2.4.1 [32] and sdf2xyz2sdf [33] packages, was applied to convert the output files from the geometry optimization into the input files for MobCal-MPI. The trajectory method (TM) was applied to calculate the CCS values for simulated collisions between the ions and N₂ as the buffer gas. [31]

3.3. Results and Discussion

3.3.1. Computational analysis of the oxidation mechanism

Figure 3.1 displays the energy diagram of the proposed mechanism for the oxidation reaction (OX). The ionized nitrogen molecules can transfer electrons to either TCDD or O₂ during the collisions in the APCI source resulting in the formation of TCDD^{•-} and O₂^{•-}. Although calculations show that TCDD^{•-}+O₂ is 21 kcal/mol more stable than TCDD+O₂^{•-}, the larger population of O₂ molecules (~ 0.01% of the N₂ gas) than TCDD molecules allows both ions to be generated in the source. Thus, two reaction paths are possible; a) when the reactants are **TCDD**+O₂^{•-} and b) when they are TCDD^{•-} (ion **TCDD1**) +O₂.

The first step of the oxidation reaction involves simultaneous cleavage of a C-Cl bond and formation of a C-O bond on the same C atom. This process transforms ion **TCDD1** into the remarkably stable ion **TCDD2**, which has an extra internal energy of 39 kcal/mol. The terminal oxygen atom and the isolated chlorine atom in ion **TCDD2** are close enough to have interatomic interactions for a Cl-O bond formation coinciding with the O-O bond cleavage. By loss of a ClO[•] (radical), the final oxidation product is produced in the form of [M-Cl+O]⁻ shown as ion **TCDD3** which is 25 kcal/mol lower in energy than the reactants. All reactants, intermediates and products are connected by low-lying energy barriers.

Geometry optimizations provided us with additional information on the structure of ion **TCDD1** (Figure S3.1,3.2). In Figure S3.1 it is clear that the C-Cl bonds have different lengths in ion **TCDD1**, and one of the carbon atoms shows a semi-bond cleavage with its adjacent chlorine atom. The distance between the mentioned C and Cl (~2.51 Å) is less than the sum of the Van der Waals radii (~3.45 Å) of the individual and Cl neutral atoms and C-Cl bonding interactions might

exist. However, the ionized species commonly show different chemical and physical behaviors compared to their neutral counterparts due to their higher levels of kinetic and internal energy. Thus, a complete C-Cl bond cleavage prior to further interactions with O₂ cannot be excluded by the existing data because the mass spectrometer cannot detect *m/z* 35 and 37 (Cl⁻) ions.

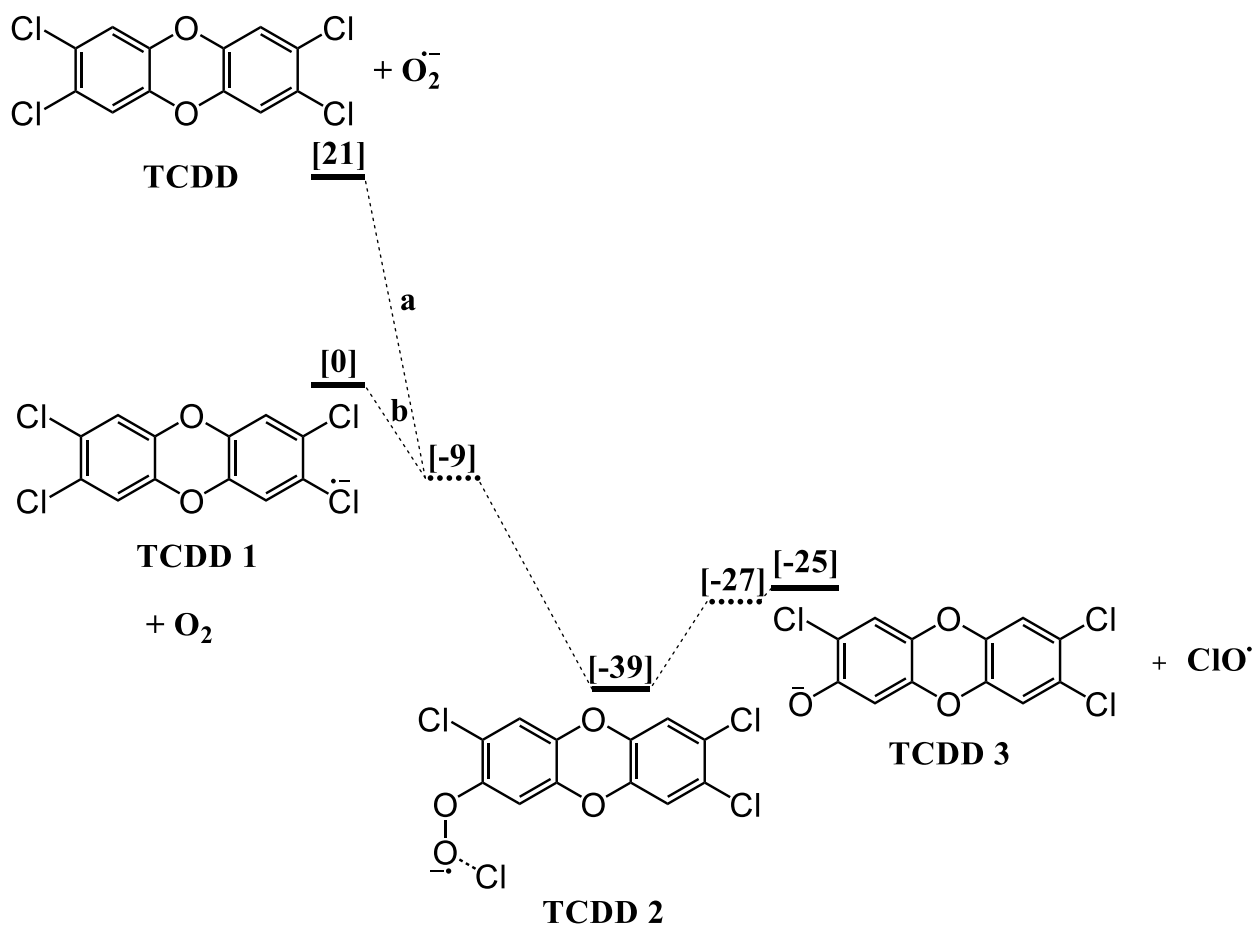


Figure 3.1. The energy diagram of the oxidation reaction ($M^+ + O_2 \rightarrow [M-Cl+O]^- + ClO^\bullet$) between 2,3,7,8 TCDD and O₂ obtained from B3LYP/6-311G (2d,p) energy calculations.

3.3.2. Computational analysis of the ether cleavage reaction mechanism

Figure 3.2 depicts the energy diagram of the proposed mechanism for the second ion-molecule reaction (ether cleavage; EC). The reaction starts with the addition of O₂ into the ion **TCDD1** that concur with a C-O bond cleavage in the dioxin ring. This bond cleavage allows for the formation

of a new bond between the carbon atom and O₂. This step stabilizes the ion **TCDD1** into ion **TCDD EC2** which gains an excess amount of internal energy equal to 26 kcal/mol.

Ion **TCDD EC2** undergoes two dihedral rotations around the C-C-O-O axis and produces ion **TCDD EC3** and a hexagonal ring structure that connects the two aromatic rings in ion **TCDD EC4**. The energy barriers of these rotations are 20 and 26 kcal/mol, respectively, below the total energy of the reactants.

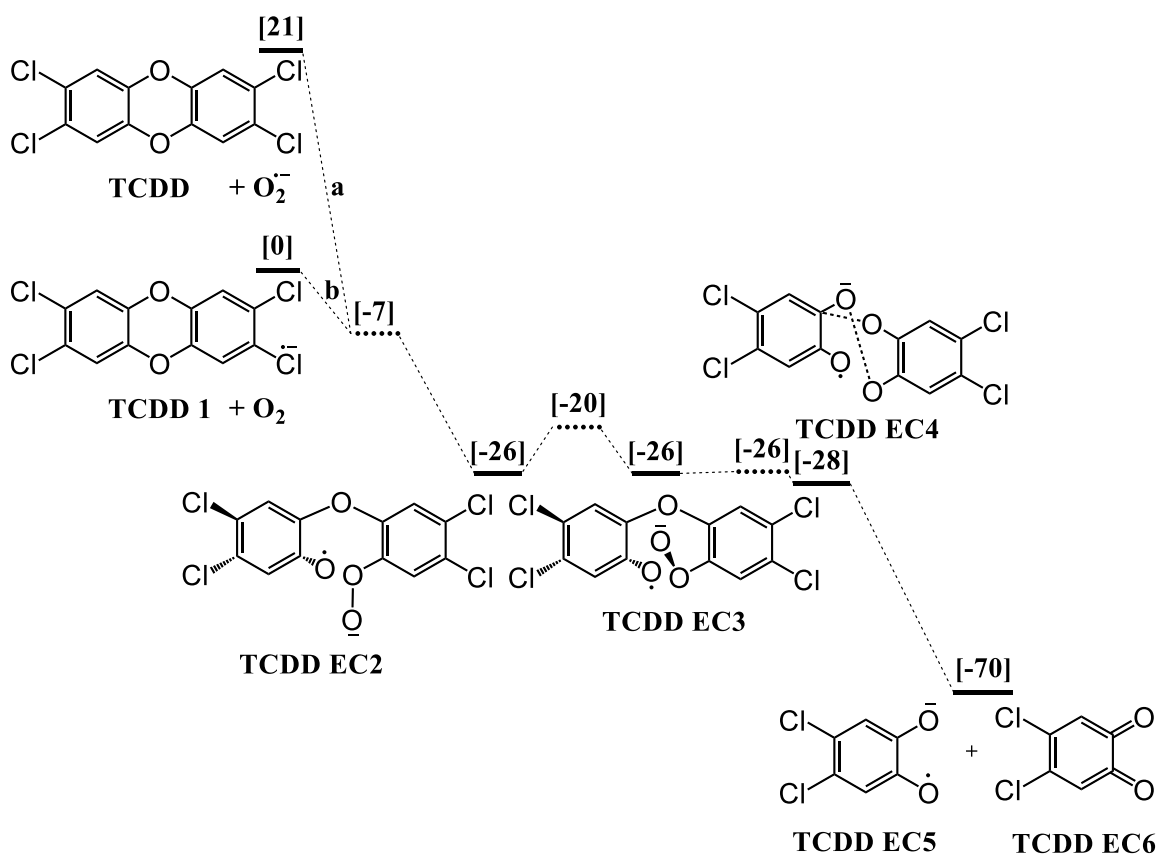


Figure 3.2. The energy diagram of the ether cleavage reaction ($M^+ + O_2 \rightarrow ECPI + ECPN$) between 2,3,7,8 TCDD and O₂ obtained from B3LYP/6-311G (2d, d, p) energy calculations.

Potential energy surface scan calculations revealed the involvement of ion **TCDD EC4** in the proposed mechanism which consists of a C₃O₃ ring that connects the two aromatic rings. The geometry optimization expanded this structure into two aromatic rings that were too distant for

showing the C_3O_3 as a completely closed ring structure. However, the C_3O_3 semi-open ring structure kept the aromatic rings partially connected (Figure S3.4).

Ion **TCDD EC4** breaks into two ether cleavage products (one anion radical, **TCDD EC5**; and the other neutral, **TCDD EC6**) immediately after its formation. The overall ether cleavage reaction stabilizes the ion **TCDD1** by producing **TCDD EC5** and **TCDD EC6** structures with a combined energy of 70 kcal/mol lower than **TCDD1**+ O_2 .

3.3.3. Is the ether cleavage reaction regioselective for asymmetric TCDDs (e.g., 1,3,7,8 TCDD)?

TCDD isomers that contain lateral-positioned chlorines can have asymmetric structures which enable them to produce two distinct ether cleavage product ions (ECPIs). For instance, the asymmetric structure of 1,3,7,8 (Figure 3.3,3.4) can produce two ether cleavage product ions (ECPIs); 1,3 ECPI and 2,3 (7,8) ECPI. For this group of congeners, the relative regioselectivity of the ether cleavage reaction toward producing each ECPI structure is not clear to us. In this study, we performed energy calculations for the reactants and ether cleavage products of 1,3,7,8 TCDD to investigate the regioselectivity of this reaction from a thermodynamic perspective. Figure 3.3 displays the resulting energy diagrams for the formation of both ECPIs and provides information to compare their levels of exothermicity. It clearly shows that in both reactions, the levels of exothermicity are nearly equal. Hence, one reaction does not have a significant thermodynamic preference over the other, and both ECPIs are expected to be produced in equal quantities.

3.3.4. The exothermicity of ether cleavage reactions on other TCDDs

Computational studies on the exothermicity of ether cleavage reactions (refer to section 3.2) were expanded to six selected toxic TCDD isomers. All six TCDDs and their ether cleavage products are shown in Figure 3.4.

Table 3.1 contains the summary of energy calculations for all selected TCDDs. The enthalpy of the ether cleavage reaction for the formation of each ECPI from the corresponding TCDD isomer provides us with enough information on the exothermicity levels. The data indicates that most TCDD isomers release similar amounts of energy (~ 70 - 76 kcal/mol) through the ether cleavage reaction. However, two isomers (1,3,6,8 and 1,3,7,9 TCDDs) show slightly higher levels

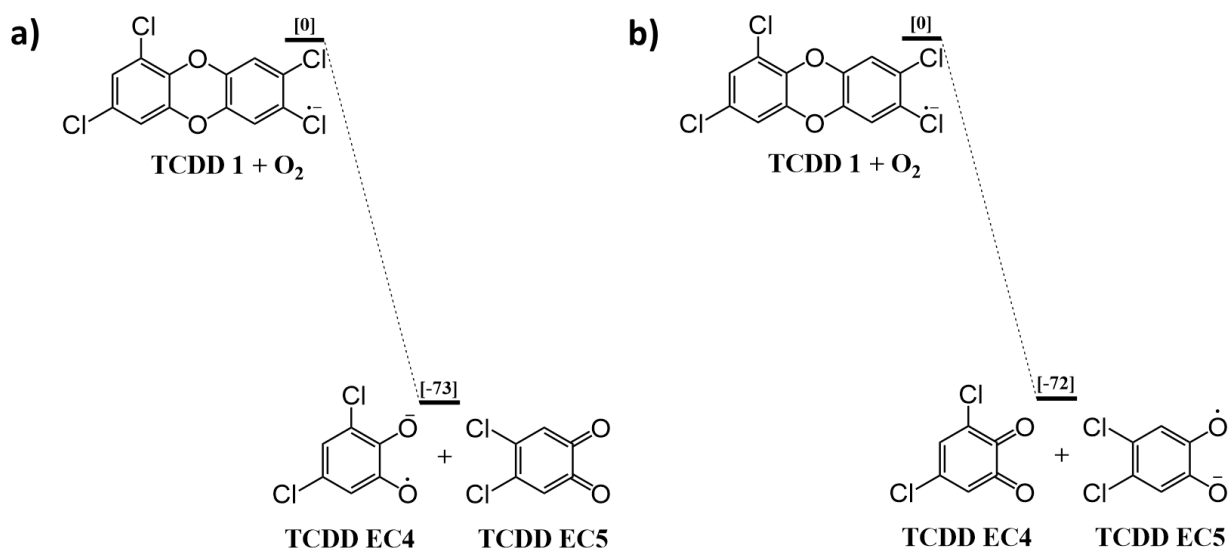


Figure 3.3. The energy diagrams of the ether cleavage reactions ($M^* \rightarrow ECPI+ECPI$) between 1,3,7,8 TCDD and O₂ for the formation of **a.** 1,3 ECPI and **b.** 2,3 ECPI obtained from B3LYP/6-311G (2d, d, p) energy calculations.

of exothermicity ($\Delta H = -81, -82$ kcal/mol). These ether cleavage reactions possess the same range of exothermicity which may further serve as thermodynamic evidence for the occurrence of ether cleavage reactions on a wide variety of lateral-substituted TCDDs, TBDDs, and TXDDs.

The optimized geometries of six TCDD^{•-} structures showed that the C-Cl bond lengths are remarkably different in four of them (1,2,3,4, 1,2,8,9, 1,3,7,8, and 2,3,7,8 TCDD) (Figure S3.5). The distances between chlorines and their adjacent carbons are shown for these four structures in Figure S3.6. For more explanation, see Section 3.1.

In the remaining two structures (1,3,6,8 and 1,3,7,9 TCDDs), all C-Cl bond lengths are in the same range. These isomers are the ones that possess the most exothermic ether cleavage reactions (Table 3.1). One long C-Cl bond may stabilize the structure of TCDD^{•-} and decrease the exothermicity of its ether cleavage reaction. However, the existing data cannot provide enough information on the complete correlation between the C-Cl bond lengths in each TCDD^{•-} structure and the exothermicity of its ether cleavage reaction.

3.3.5. Application of collision cross section in structural studies on ether cleavage products

Collision cross section (CCS), a physical property that differentiates between the ions of equal masses by their different size and shapes, can be useful to study ECPIs. Figure 3.5 displays the four ECPIs of the six TCDD isomers with their predicted CCS values obtained from MobCal-MPI. The results of the CCS calculations, including CCS values and the required resolutions (CCS/ Δ CCS), are summarized in Table 3.2. This set of results supports the experimental observations prior to structural analysis using a cyclic-ion mobility mass spectrometer. (See Chapter 2, Section 2.3.4)

From Table 3.2 it is clear that 1,2,3,4 ECPI can be easily isolated from the other ECPIs due to the fact that it has a higher mass and more extended structure. Based on the maximum CCS resolution that cyclic ion mobility can provide ($R=400$), there is a possibility that 2,3 can be

separated from 1,3/1,2 ECPIs (R=157/148) by multi-pass experiments using cIM-MS. Although this was not attempted in the current work, it remains an area for future studies. Lastly, 1,2 and 1,3 ECPIs cannot be separated from each other (R=2589!) by any of the existing ion mobility instruments.

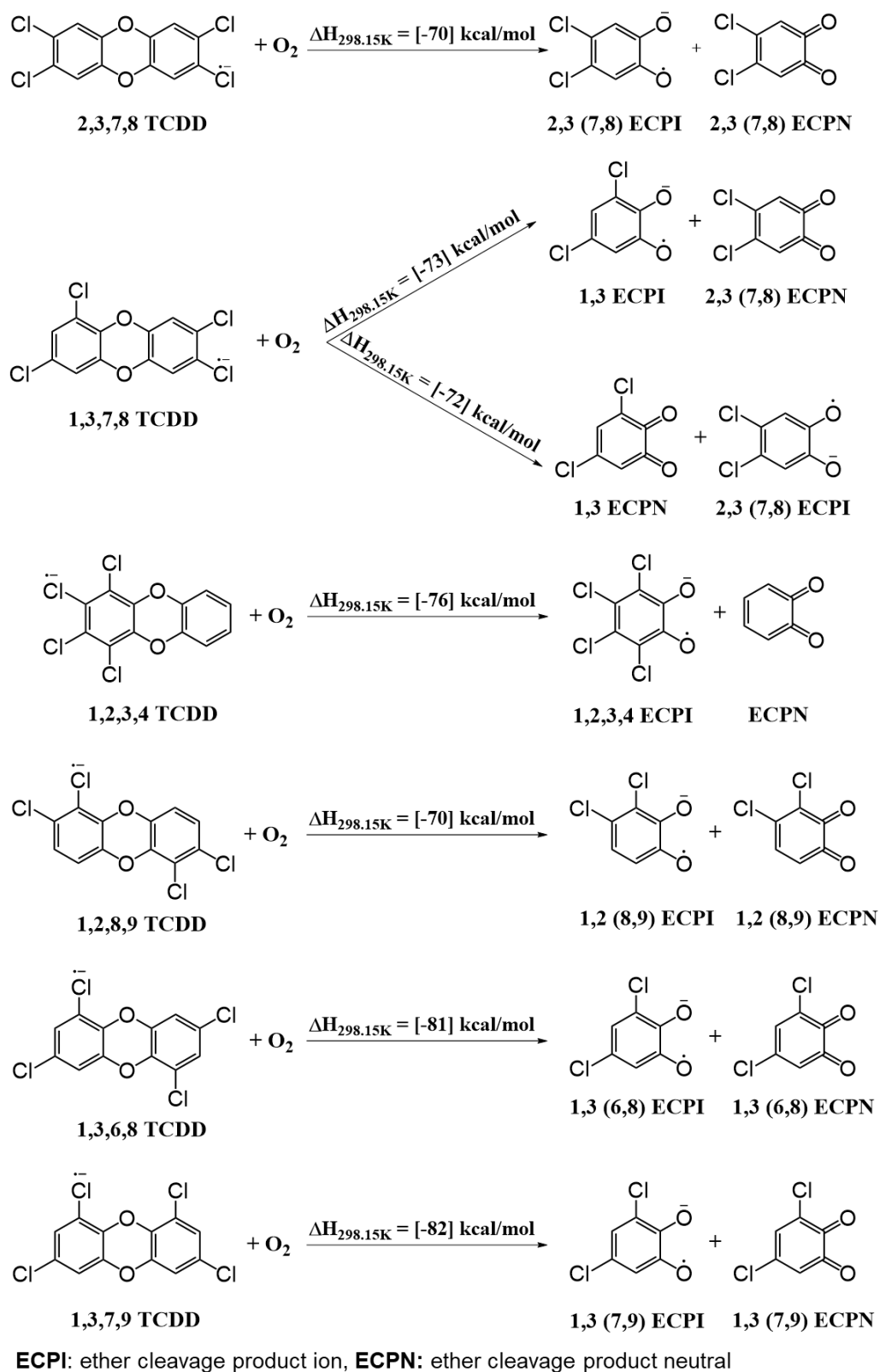
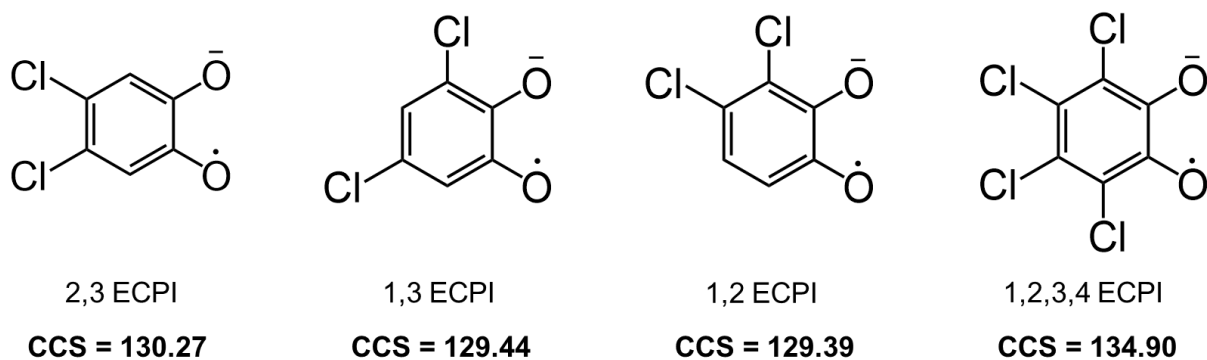


Figure 3.4. The structures of six selected TCDD⁻ structures and their ether cleavage products.

Table 3.1. The enthalpies of ether cleavage reactions of selected TCDD isomers

Structures	ΔH [298.15 K] (kcal.mol ⁻¹)
1,2,3,4 TCDD → 1,2,3,4 ECPI	-76
1,2,8,9 TCDD → 1,2 (8,9) ECPI	-70
1,3,6,8 TCDD → 1,3 (6,8) ECPI	-81
1,3,7,8 TCDD → 1,3 ECPI	-73
1,3,7,8 TCDD → 2,3 (7,8) ECPI	-72
1,3,7,9 TCDD → 1,3 (7,9) ECPI	-82
2,3,7,8 TCDD → 2,3 (7,8) ECPI	-70

**Figure 3.5.** The structures of ECPIs produced from the six selected TCDD isomers and the corresponding theoretical CCS values obtained from MobCal-MPI calculations.**Table 3.2.** Theoretical CCS values of ether cleavage products of the selected TCDD isomers and the required CCS resolutions obtained from MobCal-MPI calculations.

Structures	$CCS_{N_2}^{TM}$ (MobCal-MPI) (Å ²)	Required Resolution
1,2,3,4 ECPI	134.90	29 ^a
1,2 ECPI	129.39	2589 ^b
1,3 ECPI	129.44	157 ^c
2,3 ECPI	130.27	148 ^d

CCS resolutions are reported between **a.** 1,2,3,4 ECPI and 2,3 ECPI, **b.** 1,2 ECPI and 1,3 ECPI, **c.** between 1,3 ECPI and 2,3 ECPI, and **d.** 2,3 ECPI and 1,2 ECPI.

3.4. Conclusions

The computational study on oxidation and ether cleavage reactions between TCDDs and oxygen under APCI (-) conditions indicated that both ion-molecule reactions are highly exothermic. Although the computations covered only six selected TCCD isomers, the exothermicity levels may represent the occurrence of these reactions on a wide range of tetrahalogenated dibenzo-*p*-dioxins.

All halogenated dioxins can potentially undergo the oxidation reactions. However, the selectivity of the ether cleavage reaction towards lateral-positioned halogens limits its occurrence on the toxic dioxins. This selectivity can allow for further applications of the ether cleavage reaction as a structure-based identification tool that differentiates between toxic and non-toxic TBDDs and TXDDs. The application of this reaction might be expanded to above a thousand of potentially toxic PCDD/Fs, PBDD/Fs, and PXDD/Fs that are not easily identified in complex environmental samples.

The main focus of this study was on the theoretical explanation of the reactions and computational predictions to open the experimental path for further structural analysis on ether cleavage products using GC-APCI (-) coupled with cIM-MS. Future experiments can provide us with a diagnostic tool for toxic tetrahalogenated and polyhalogenated dibenzo-*p*-dioxins and furans that may also separate them based on their structures and the corresponding levels of toxicity.

References

- [1] B. Patrizi, M.S. de Cumis, TCDD toxicity mediated by epigenetic mechanisms, *Int. J. Mol. Sci.* 19 (2018) 1–15. <https://doi.org/10.3390/ijms19124101>.
- [2] R.E. Alcock, K.C. Jones, Dioxins in the environment: A review of trend data, *Environ. Sci. Technol.* 30 (1996) 3133–3143. <https://doi.org/10.1021/es960306z>.
- [3] A.L. Young, *The History, Use, Disposition and Environmental Fate of Agent Orange*, Springer US, 2009. https://link.springer.com/chapter/10.1007/978-0-387-87486-9_5.
- [4] J.A. van Zorge, J.H. van Wijnen, R.M.C. Theelen, K. Olie, M. van den Berg, Assessment of the toxicity of mixtures of halogenated dibenzo-p-dioxins and dibenzofurans by use of toxicity equivalency factors (TEF), *Chemosphere.* 19 (1989) 1881–1890. <https://www.unhcr.org/publications/manuals/4d9352319/unhcr-protection-training-manual-european-border-entry-officials-2-legal.html?query=excom> 1989.
- [5] R. Ishaq, C. Näf, Y. Zebühr, D. Broman, U. Järnberg, PCBs, PCNs, PCDD/Fs, PAHs and Cl-PAHs in air and water particulate samples - Patterns and variations, *Chemosphere.* 50 (2003) 1131–1150. [https://doi.org/10.1016/S0045-6535\(02\)00701-4](https://doi.org/10.1016/S0045-6535(02)00701-4).
- [6] M. Zhang, A. Buekens, X. Jiang, X. Li, Dioxins and polyvinylchloride in combustion and fires, *Waste Manag. Res.* 33 (2015) 630–643. <https://doi.org/10.1177/0734242X15590651>.
- [7] S. Fernando, K.J. Jobst, V.Y. Taguchi, P.A. Helm, E.J. Reiner, B.E. McCarry, Identification of the halogenated compounds resulting from the 1997 Plastimet Inc. fire in Hamilton, Ontario, using comprehensive two-dimensional gas chromatography and (ultra)high resolution mass spectrometry, *Environ. Sci. Technol.* 48 (2014) 10656–10663.

<https://doi.org/10.1021/es503428j>.

- [8] Plastimet Inc. fire in Hamilton, Ontario, July 9-12, 1997, I (1997) 1997.
- [9] V.Y. Taguchi, R.J. Nieckarz, R.E. Clement, S. Krolik, R. Williams, Dioxin Analysis by Gas Chromatography-Fourier Transform Ion Cyclotron Resonance Mass Spectrometry (GC-FTICRMS), *J. Am. Soc. Mass Spectrom.* 21 (2010) 0–3. <http://link.springer.com/10.1016/j.jasms.2010.07.010> <http://link.springer.com/10.1016/j.jasms.2010.07.010>
- [10] S. Fernando, M.K. Green, K. Organtini, F. Dorman, R. Jones, E.J. Reiner, K.J. Jobst, Differentiation of (Mixed) Halogenated Dibenzop-Dioxins by Negative Ion Atmospheric Pressure Chemical Ionization, *Anal. Chem.* 88 (2016) 5205–5211. <https://doi.org/10.1021/acs.analchem.6b00255>.
- [11] A.L. Myers, S.A. Mabury, E.J. Reiner, Analysis of mixed halogenated dibenzo-p-dioxins and dibenzofurans (PXDD/PXDFs) in soil by gas chromatography tandem mass spectrometry (GC-MS/MS), *Chemosphere.* 87 (2012) 1063–1069. <https://doi.org/10.1016/j.chemosphere.2012.02.013>.
- [12] G.W. Sovocool, R.K. Mitchum, Y. Tondeur, W.D. Munslow, T.L. Vonnahme, J.R. Donnelly, Bromo- and bromochloro-polynuclear aromatic hydrocarbons, dioxins and dibenzofurans in municipal incinerator fly ash, *Biomed. Environ. Mass Spectrom.* 15 (1988) 669–676. <https://doi.org/10.1002/bms.1200151205>.
- [13] X. Yu, M. Zennegg, M. Engwall, A. Rotander, M. Larsson, M. Hung Wong, R. Weber, E-waste recycling heavily contaminates a Chinese city with chlorinated, brominated and mixed halogenated dioxins, *Organohalogen Compd.* 70 (2008) 813–816.

- [14] J.F. Viel, P. Arveux, J. Baverel, J.Y. Cahn, Soft-tissue sarcoma and non-Hodgkin's lymphoma clusters around a municipal solid waste incinerator with high dioxin emission levels, *Am. J. Epidemiol.* 152 (2000) 13–19. <https://doi.org/10.1093/aje/152.1.13>.
- [15] E.J. Mrema, F.M. Rubino, G. Brambilla, A. Moretto, A.M. Tsatsakis, C. Colosio, Persistent organochlorinated pesticides and mechanisms of their toxicity, *Toxicology.* 307 (2013) 74–88. <https://doi.org/10.1016/j.tox.2012.11.015>.
- [16] F. Maqbool, S. Mostafalou, H. Bahadar, M. Abdollahi, Review of endocrine disorders associated with environmental toxicants and possible involved mechanisms, *Life Sci.* 145 (2016) 265–273. <https://doi.org/10.1016/j.lfs.2015.10.022>.
- [17] T.T. Schug, A.F. Johnson, L.S. Birnbaum, T. Colborn, L.J. Guillette, D.P. Crews, T. Collins, A.M. Soto, F.S. Vom Saal, J.A. McLachlan, C. Sonnenschein, J.J. Heindel, Minireview: Endocrine disruptors: Past lessons and future directions, *Mol. Endocrinol.* 30 (2016) 833–847. <https://doi.org/10.1210/me.2016-1096>.
- [18] Y.S. Lin, J.L. Caffrey, P.C. Hsu, M.H. Chang, M.F. Faramawi, J.W. Lin, Environmental exposure to dioxin-like compounds and the mortality risk in the U.S. population, *Int. J. Hyg. Environ. Health.* 215 (2012) 541–546. <https://doi.org/10.1016/j.ijheh.2012.02.006>.
- [19] Y.Y. Zhao, F.M. Tao, E.Y. Zeng, Theoretical study of the quantitative structure-activity relationships for the toxicity of dibenzo-p-dioxins, *Chemosphere.* 73 (2008) 86–91. <https://doi.org/10.1016/j.chemosphere.2008.05.018>.
- [20] S. Hirokawa, T. Imasaka, T. Imasaka, Chlorine substitution pattern, molecular electronic properties, and the nature of the ligand-receptor interaction: Quantitative property-activity relationships of polychlorinated dibenzofurans, *Chem. Res. Toxicol.* 18 (2005) 232–238.

<https://doi.org/10.1021/tx049874f>.

- [21] M. Larsson, M. Van Den Berg, P. Brenerová, M.B.M. Van Duursen, K.I. Van Ede, C. Lohr, S. Luecke-Johansson, M. Machala, S. Naser, K. Pěňčíková, L. Poellinger, D. Schrenk, S. Strapáčová, J. Vondráček, P.L. Andersson, Consensus toxicity factors for polychlorinated dibenzo-P-Dioxins, dibenzofurans, and biphenyls combining in silico models and extensive in vitro screening of AhR-mediated effects in human and rodent cells, *Chem. Res. Toxicol.* 28 (2015) 641–650. <https://doi.org/10.1021/tx500434j>.
- [22] M. van den Berg, M.S. Denison, L.S. Birnbaum, M.J. DeVito, H. Fiedler, J. Falandysz, M. Rose, D. Schrenk, S. Safe, C. Tohyama, A. Tritscher, M. Tysklind, R.E. Peterson, Polybrominated dibenzo-p-dioxins, dibenzofurans, and biphenyls: Inclusion in the toxicity equivalency factor concept for dioxin-like compounds, *Toxicol. Sci.* 133 (2013) 197–208. <https://doi.org/10.1093/toxsci/kft070>.
- [23] M. Van den Berg, L.S. Birnbaum, M. Denison, M. De Vito, W. Farland, M. Feeley, H. Fiedler, H. Hakansson, A. Hanberg, L. Haws, M. Rose, S. Safe, D. Schrenk, C. Tohyama, A. Tritscher, J. Tuomisto, M. Tysklind, N. Walker, R.E. Peterson, The 2005 World Health Organization reevaluation of human and mammalian toxic equivalency factors for dioxins and dioxin-like compounds, *Toxicol. Sci.* 93 (2006) 223–241. <https://doi.org/10.1093/toxsci/kfl055>.
- [24] S. Bandiera, T. Sawyer, M. Romkes, B. Zmudzka, L. Safe, G. Mason, Polychlorinated dibenzofurans (PCDFs): effects of structure on binding to the 2,3,7,8-TCDD cytosolic receptor protein, AHH induction and toxicity, *Elsevier.* 32 (1984). [https://doi.org/10.1016/0300-483X\(84\)90132-X](https://doi.org/10.1016/0300-483X(84)90132-X).

- [25] E.J. Reiner, R.E. Clement, A.B. Okey, C.H. Marvin, Advances in analytical techniques for polychlorinated dibenzo-p-dioxins, polychlorinated dibenzofurans and dioxin-like PCBs, *Anal. Bioanal. Chem.* 386 (2006) 791–806. <https://doi.org/10.1007/s00216-006-0479-1>.
- [26] J. Hagberg, Analysis of brominated dioxins and furans by high resolution gas chromatography/high resolution mass spectrometry, *J. Chromatogr. A.* 1216 (2009) 376–384. <https://doi.org/10.1016/j.chroma.2008.10.022>.
- [27] D. Zacs, J. Rjabova, A. Viksna, V. Bartkevics, Method development for the simultaneous determination of polybrominated, polychlorinated, mixed polybrominated/chlorinated dibenzo-p-dioxins and dibenzofurans, polychlorinated biphenyls and polybrominated diphenyl ethers in fish, *Chemosphere.* 118 (2015) 72–80. <https://doi.org/10.1016/j.chemosphere.2014.06.032>.
- [28] E.J. Reiner, The analysis of dioxins and related compounds, Wiley Period. Inc., *Mass Spec Rev.* (2009). <https://doi.org/10.1002/mas>.
- [29] K.L. Organtini, L. Haimovici, K.J. Jobst, E.J. Reiner, A. Ladak, D. Stevens, J.W. Cochran, F.L. Dorman, Comparison of Atmospheric Pressure Ionization Gas Chromatography-Triple Quadrupole Mass Spectrometry to Traditional High-Resolution Mass Spectrometry for the Identification and Quantification of Halogenated Dioxins and Furans, *Anal. Chem.* 87 (2015) 7902–7908. <https://doi.org/10.1021/acs.analchem.5b01705>.
- [30] W.C. Gaussian 16, Revision C.01, Frisch, M. J.; Trucks, G. W.; Schlegel, H. B.; Scuseria, G. E.; Robb, M. A.; Cheeseman, J. R.; Scalmani, G.; Barone, V.; Petersson, G. A.; Nakatsuji, H.; Li, X.; Caricato, M.; Marenich, A. V.; Bloino, J.; Janesko, B. G.; Gomper, Gaussian 16, Revision C.01, (2016). <https://gaussian.com/citation/>.

- [31] C. Ieritano, J. Crouse, J.L. Campbell, W.S. Hopkins, A parallelized molecular collision cross section package with optimized accuracy and efficiency, *Analyst*. 144 (2019) 1660–1670. <https://doi.org/10.1039/c8an02150c>.
- [32] N.M. O’Boyle, M. Banck, C.A. James, C. Morley, T. Vandermeersch, G.R. Hutchison, Open Babel, *J. Cheminform.* 3 (2011) 1–14. <https://jcheminf.biomedcentral.com/track/pdf/10.1186/1758-2946-3-33>.
- [33] P. Tosco, T. Balle, F. Shiri, SDF2XYZ2SDF: How to exploit TINKER power in cheminformatics projects, *J. Mol. Model.* 17 (2011) 3021–3023. <https://doi.org/10.1007/s00894-011-1111-7>.

Supporting Information

Contents

Table S3.1. Energy levels of the reactants, intermediates, products and transition structures of the ion-molecule reactions between 2,3,7,8 TCDD and O ₂ obtained from B3LYP/6-311G (2d, d, p) energy calculations. (E_{total} is the total calculated energy in Hartree at 298.15 K) The energy levels of the structures corresponding to the oxidation reaction (OX) are located at the top part and the ones for the ether cleavage reaction (EC) are reported at the bottom part of the table	133
Figure S3.1. The optimized geometry of 2,3,7,8 TCDD radical anion and C-Cl bonds length obtained from gaussian g.16 calculations (B3LYP/6-311G (2d, d, p))	134
Figure S3.2. The optimized geometries of the reactants, intermediates, products, and the transition structures (PCDD1-PCDD3) of the oxidation reaction ($M^{\cdot-} \rightarrow [M-Cl+O]^{\cdot-}$) between 2,3,7,8 TCDD and O ₂ obtained from gaussian g.16 calculations (B3LYP/6-311G (2d, d, p))	134
Figure S3.3. The optimized geometries of the reactants, intermediates, products, and the transition structures (PCDD1-PCDD EC5) of the ether cleavage reaction ($M^{\cdot-} \rightarrow ECPI+ECPN$) between 2,3,7,8 TCDD and O ₂ obtained from gaussian g.16 calculations (B3LYP/6-311G (2d, d, p))	135
Figure S3.4. The optimization of PCDD EC4 geometry from the minimum between TS 3b and PCDD EC5+ PCDD EC6.....	136
Figure S3.5. The optimized geometries of the selected TCDD isomers obtained from gaussian g.16 calculations (B3LYP/6-311G (2d, d, p))	137
Figure S3.6. The optimized geometries of the selected TCDD isomers and C-Cl bonds length obtained from gaussian g.16 calculations (B3LYP/6-311G (2d, d, p))	138

Figure S3.7. The optimized geometries of ether cleavage products of the selected TCDD isomers obtained from gaussian g.16 calculations (B3LYP/6-311G (2d, d, p)) 139

Table S3.1. Energy levels of the reactants, intermediates, products and transition structures of the ion-molecule reactions between 2,3,7,8 TCDD and O₂ obtained from B3LYP/6-311G (2d, d, p) calculations. (E_{total} is the total calculated energy in Hartree and the relative energy (Rel. E) is reported in kcal/mol at 298.15 K) The energy levels of the structures corresponding to the oxidation reaction (OX) are located at the top part and the ones for the ether cleavage reaction (EC) are reported at the bottom part of the table.

Structure	E_{total} [298.15 K]	Rel. E [298.15 K]	Transition State	E_{total} [298.15 K]	Rel. E [298.15 K]
TCDD (2,3,7,8 TCDD)	-2451.1530834	-	-	-	-
O ₂ ⁻	-150.3540919	-	-	-	-
TCDD + O₂⁻	-2601.5071753	21	-	-	-
TCDD 1	-2451.175403	-	-	-	-
O ₂	-150.3647876	-	-	-	-
TCDD 1 + O₂	-2601.540191	0	TS1_{OX} (TCDD1+ O₂→ TCDD2)	-2601.554347	-9
TCDD 2	-2601.602406	-39	TS2_{OX} (TCDD2→ TCDD 3 + ClO')	-2601.58373	-27
TCDD 3	-2066.235901	-	-	-	-
ClO'	-535.3442814	-	-	-	-
TCDD 3 + ClO'	-2601.580182	-25	-	-	-
TCDD 1 + O₂	-2601.540191	0	TS1_{EC} (TCDD 1 + O₂→ TCDD EC2)	-2601.55103	-7
TCDD EC2	-2601.581805	-26	TS2_{EC} (TCDD EC2→ TCDD EC3)	-2601.572436	-20
TCDD EC3	-2601.5822267	-26	TS3_{EC} (TCDD EC3→ TCDD EC4 + EC5)	-2601.581446	-26
TCDD EC4	-2601.585604	-28	-	-	-
TCDD EC5 (2,3 ECPI)	-1300.871963	-	-	-	-
TCDD EC6 (2,3 ECPN)	-1300.77969	-	-	-	-
TCDD EC5 + TCDD EC6	-2601.651653	-70	-	-	-

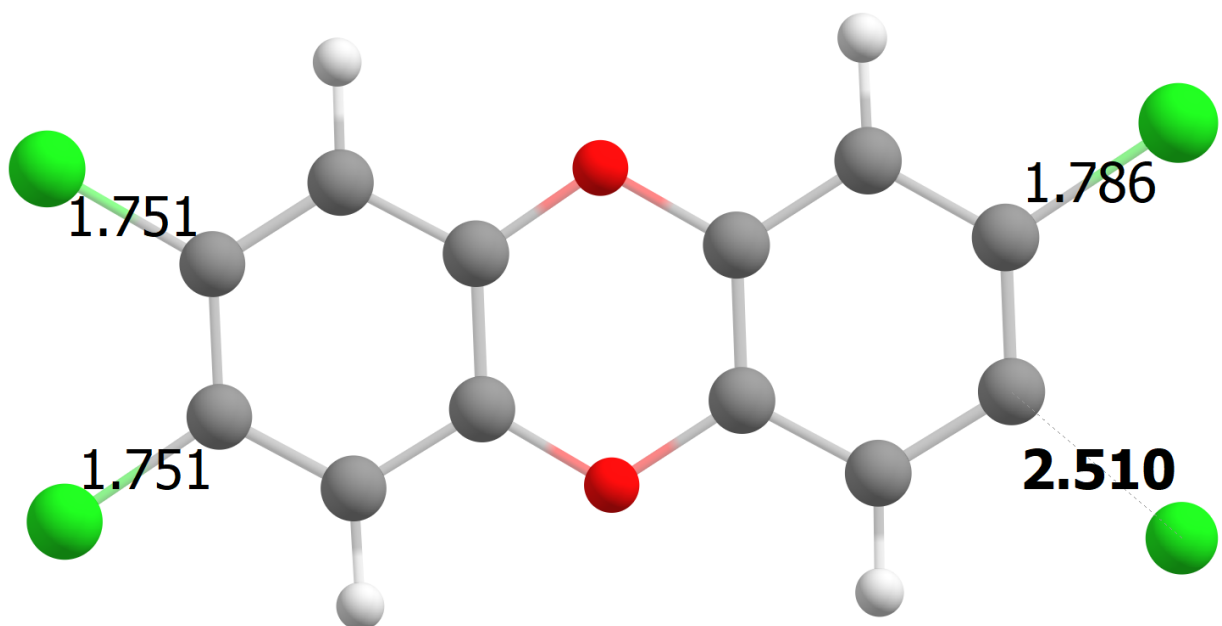


Figure S3.1. The optimized geometry of 2,3,7,8 TCDD radical anion ($\text{TCDD}^{\bullet-}$) and C-Cl bonds length obtained from gaussian g.16 calculations (B3LYP/CBSB7).

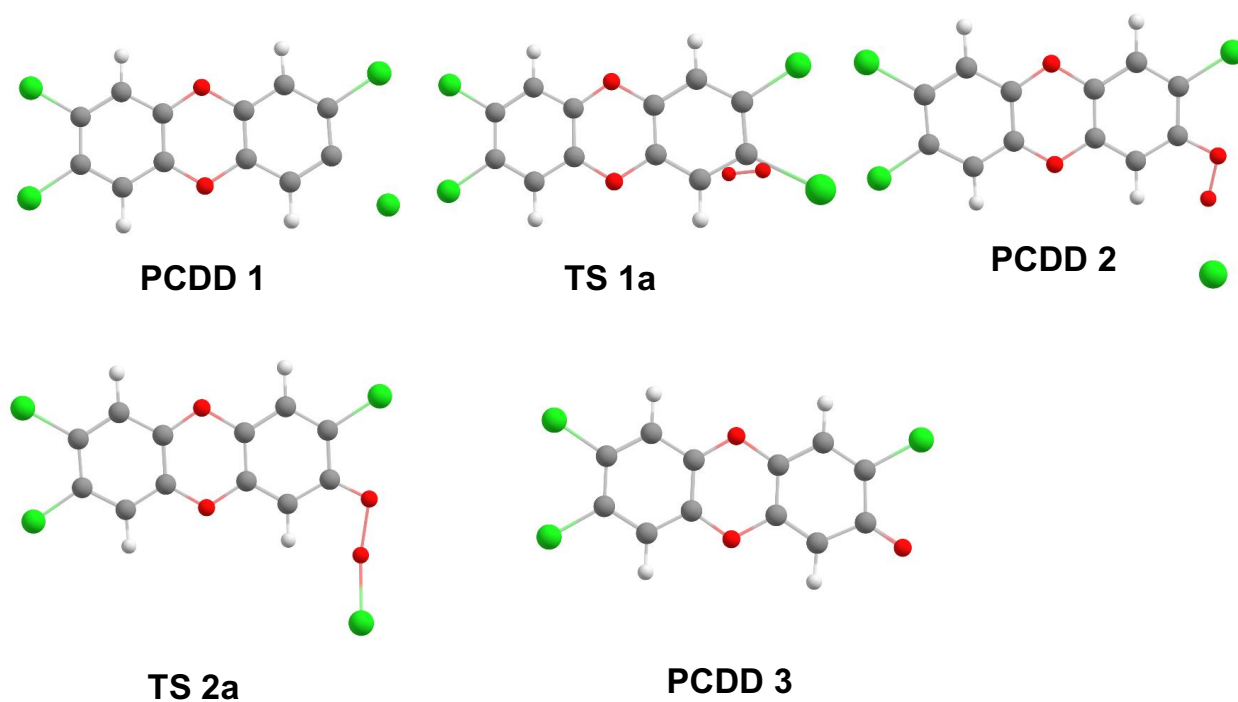


Figure S3.2. The optimized geometries of the reactants, intermediates, products, and the transition structures (PCDD1-PCDD3; also named as TCDD1-TCDD3) of the oxidation reaction ($\text{M}^{\bullet-} \rightarrow [\text{M}-\text{Cl}+\text{O}]^-$) between 2,3,7,8 TCDD and O_2 obtained from gaussian g.16 calculations (B3LYP/CBSB7).

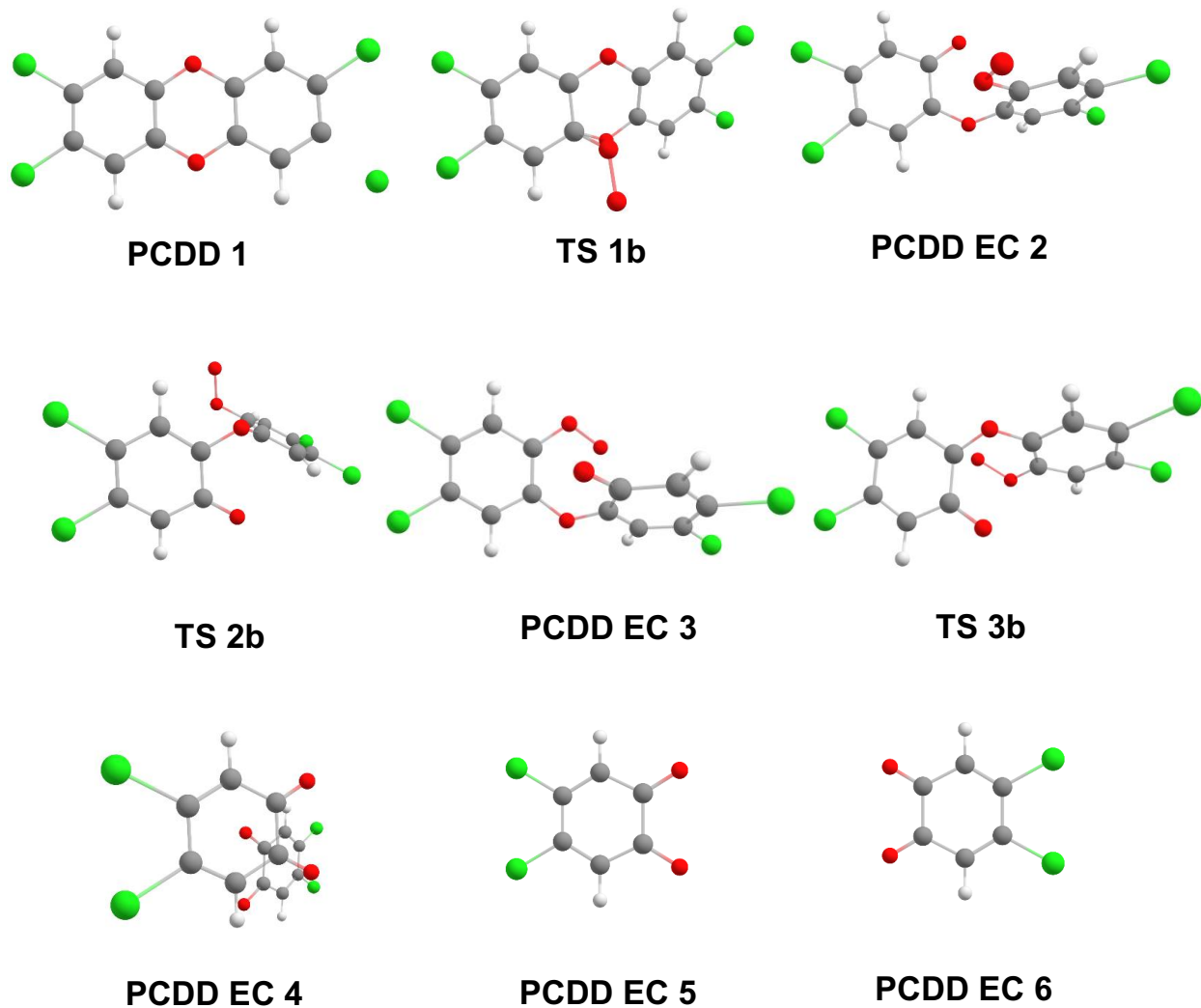


Figure S3.3. The optimized geometries of the reactants, intermediates, products, and the transition structures (PCDD1-PCDD EC5; also named as TCDD1-TCDD EC5) of the ether cleavage reaction ($M^+ \rightarrow ECPI+ECPN$) between 2,3,7,8 TCDD and O_2 obtained from gaussian g.16 calculations (B3LYP/CBSB7).

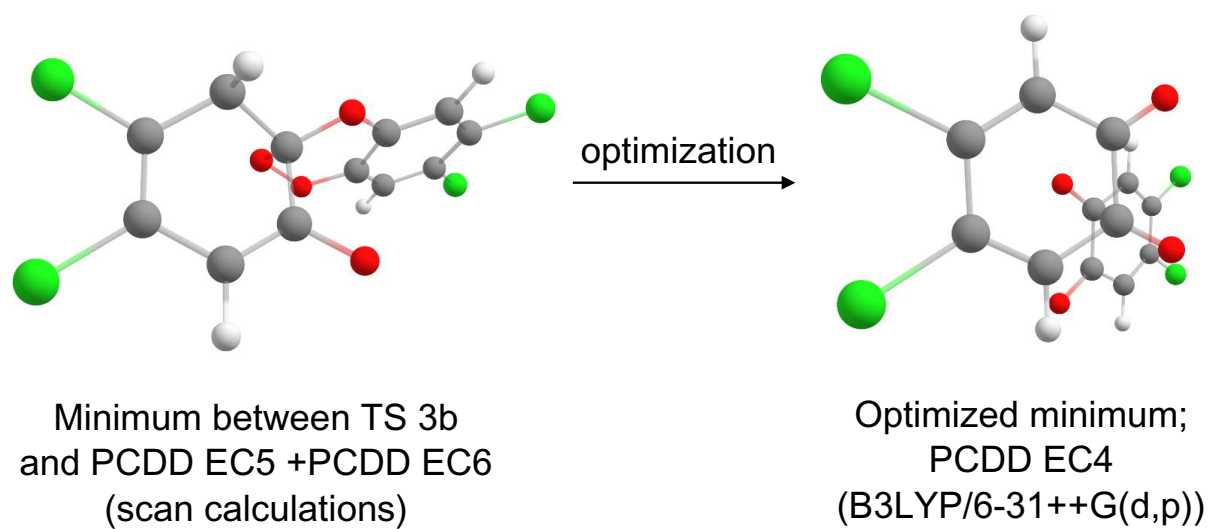


Figure S3.4. The optimization of PCDD EC4 (also named as TCDD EC4) geometry from the minimum between TS 3b and PCDD EC5+ PCDD EC6 (also named as TCDD EC5+ TCDD EC6).

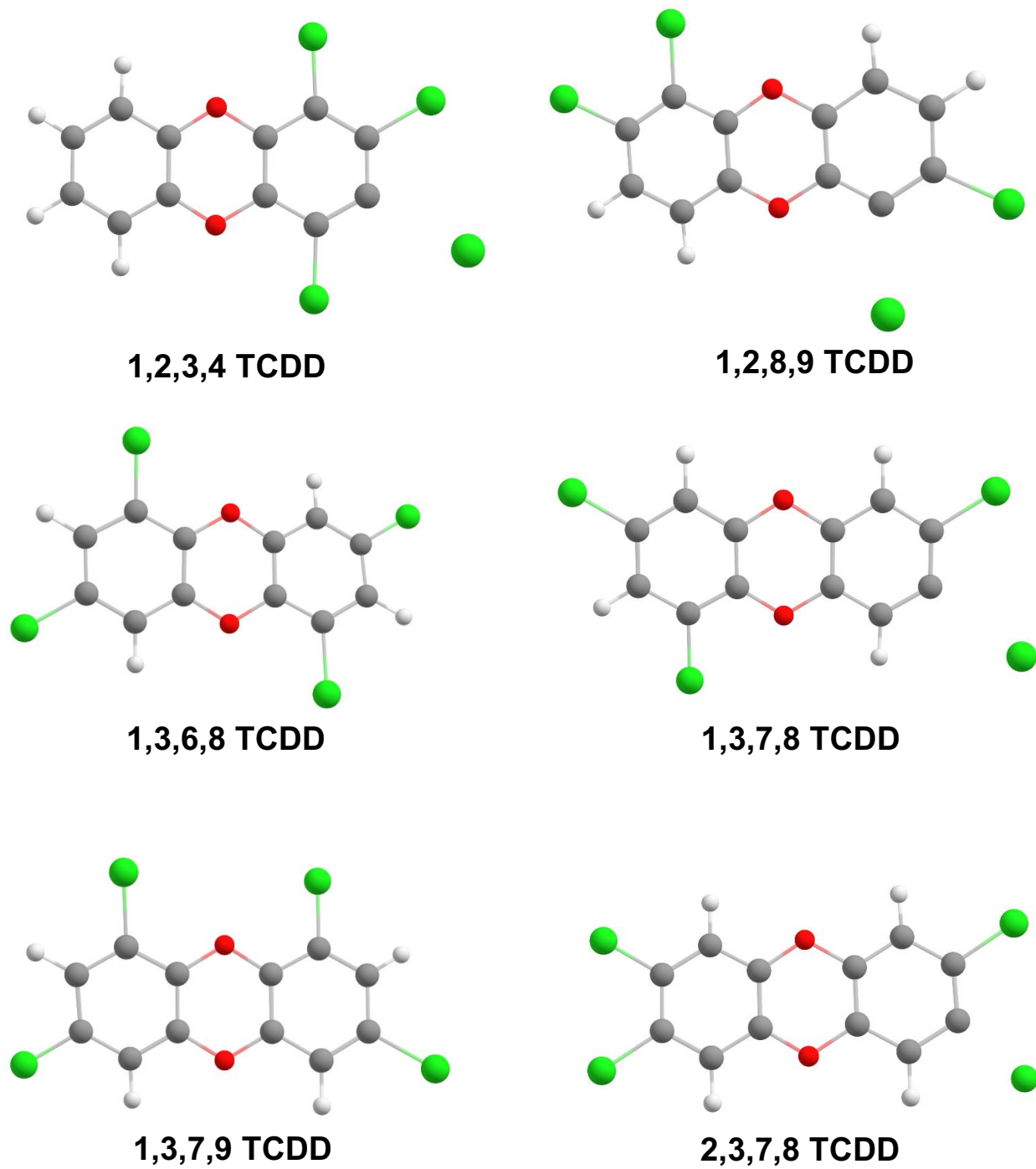


Figure S3.5. The optimized geometries of the selected TCDD isomers radical anions (TCDD⁻) obtained from gaussian g.16 calculations (B3LYP/CBSB7)

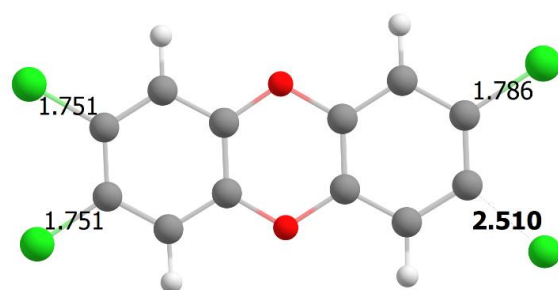
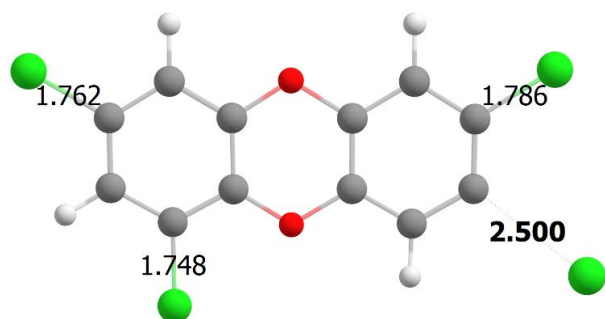
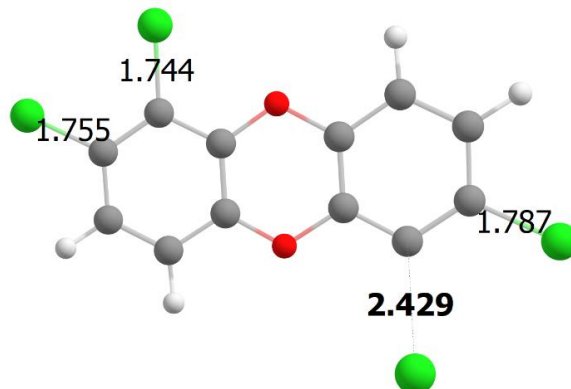
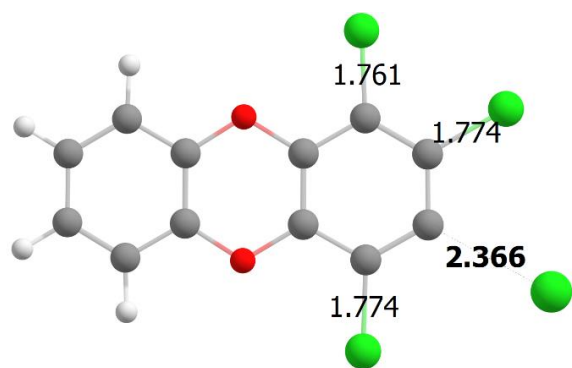


Figure S3.6. The optimized geometries of the selected TCDD isomers and C-Cl bonds length obtained from gaussian g.16 calculations (B3LYP/CBSB7)

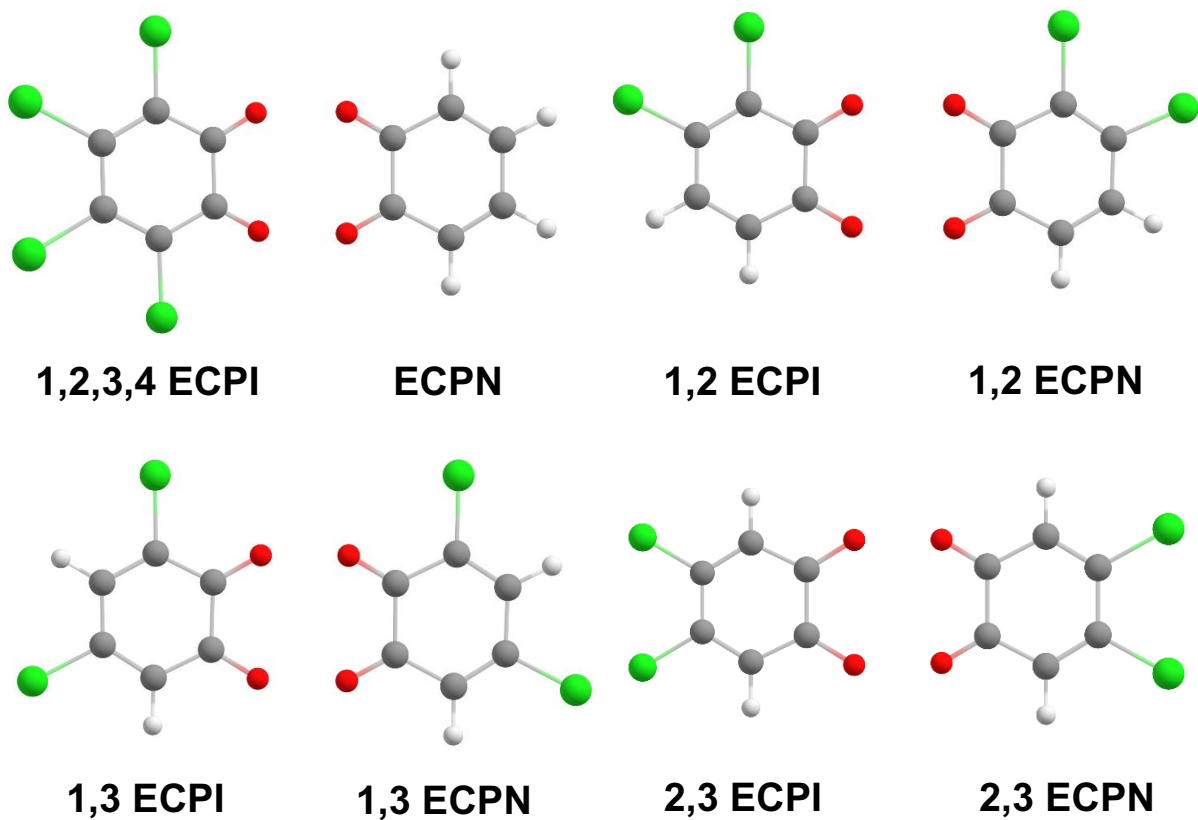


Figure S3.7. The optimized geometries of ether cleavage products of the selected TCDD isomers obtained from gaussian g.16 calculations (B3LYP/CBSB7)

Chapter 4. Conclusions and future work

Computational and experimental results indicate that the application of selective ion-molecule reactions of TCPs and TCDDs may be expanded to a wide range of unknown triaryl phosphates and tetrahalogenated (and potentially polyhalogenated) dibenzo-p-dioxins. The scope of this thesis was mostly focused on the mechanistic analysis of the ion molecule reactions, and this knowledge may eventually result in an efficient diagnostic tool for toxic compounds present in complex environmental mixtures.

Based on DFT calculations, theory suggests that the ion-molecule reaction between tricresyl phosphate and ozone is more likely to happen under the APCI conditions relative to dioxygen. Instrumental analysis on deuterium labelled tricresyl phosphates supported both proposals for the mechanism. The ion-molecule reaction is selective towards the ortho-substituted methyl groups and all tricresyl phosphates containing at least one ortho-cresyl group can undergo the reaction. Ion mobility experiments on [CBDP-H]⁺ product ions revealed the formation of at least two structures (m/z 275) during the ion-molecule reaction. Mass spectrometry experiments on the ethyl-substituted homologue of ToCP showed that the ion-molecule reaction occurs not only on toxic tricresyl phosphates, but also on other potentially toxic triaryl phosphate homologues.

One limitation for the occurrence of the ion-molecule reaction in this study was the low concentration ratio of the molecular ions to protonated ions (ToCP⁺/[ToCP+H]⁺). While ToCP⁺ is the starting structure for the ion-molecule reaction, the higher ToCP⁺/[ToCP+H]⁺ ratios result in higher yields of reaction and the higher concentration of [CBDP-H]⁺ product ion. One main reason for the generation of [ToCP+H]⁺ ions in high concentrations is the presence of volume of

H₂O inside the APCI source. A solution to overcome this limitation is replacing the APCI by an APPI technique, because the photoionization technique will not provide excess ionization energy to ionize H₂O. Further instrumental analysis should also be performed on environmental and industrial samples containing complex mixtures of triaryl phosphates, including jet engine oil, indoor dust and air. This can potentially expand the application of the studied ion-molecule reaction as a fast and efficient identification tool for a large variety of unknown toxic triaryl phosphates. Future studies may also expand our knowledge on the structures of triaryl phosphates by linking the ion mobility experiments on precursor and decomposition product ions to the toxicity level of the triaryl phosphates.

Computational analysis on the ion-molecule reactions between tetrachlorinated dibenzo-p-dioxins and dioxygen showed that both reactions are highly exothermic. The oxidation reaction is a common reaction for halogenated organic chemicals with a Cl atom displaced by the addition of an oxygen atom ($[M+O-Cl]^-$). However, the ether cleavage reaction is of a more analytical interest due to its selectivity towards the toxic isomers of tetrachlorinated dibenzo-p-dioxins. This ether cleavage reaction does not show a thermodynamic preference on producing one ether cleavage product ion over another from an asymmetric TCDD structure. Thus, one TCDD/TBDD/TXDD structure can potentially produce more than one ether cleavage product ion. The ether cleavage product ions can be separated by ion mobility, but the resolving power of this technique is currently a limitation. Future studies on the ether cleavage reactions of dibenzo-p-dioxins must include instrumental analysis of tetrachlorinated, brominated and mixed halogenated dioxin standards. The complementary experiments with polyhalogenated congeners containing more than four halogens are recommended to investigate the highest potentials of the ether cleavage reaction as a diagnostic tool for a wide range of toxic dioxins.

Eventually, this identification approach could be applied on real samples. Complex samples contain mixtures of thousands of (mixed) polyhalogenated dibenzo-p-dioxins, most of which are not available as authentic standards. The selectivity of the ether cleavage reaction provides a reliable separation technique that differentiates between toxic and non-toxic PHDDs.

Finally, ion chemistry is important! While a wide range of toxic triaryl phosphate and polyhalogenated dibenzo-p-dioxin pollutants are unknown to us, ion chemistry can help identify them when other separations techniques fail.

a)



b)



Last Photographs as a member of Jobst Team. a) At the end of my Master's seminar session with my supervisor, Dr. Jobst, and colleagues, Ethan, Amber, Meera and Mahin. **b)** As a Jobst lab tradition, scientists/engineers who did something AMAZING with the cyclic ion mobility mass spectrometer, sign the instrument with a silver permanent marker (more colors may be available in the future). I am so happy and excited for having my signature on our cIM-MS forever! (R. A.)